Engineering nanoparticles using chemical and biological approaches for tumor targeted delivery

by

Tuyen Duong Thanh Nguyen

B.Sc., Cantho University, Vietnam, 2014

AN ABSTRACT OF A DISSERTATION

submitted in partial fulfillment of the requirements for the degree

DOCTOR OF PHILOSOPHY

Department of Chemistry
College of Arts and Sciences

KANSAS STATE UNIVERSITY
Manhattan, Kansas

2019

Abstract

Nanotechnology offers exciting options for the site-selective delivery of chemotherapeutics and diagnostic agents using nanoparticles. Varieties of organic and inorganic nanomaterials have been explored extensively as a delivery system either in the form of drug carriers or imaging agents. Successful stories include the clinical translation of anticancer nanomedicines such as PEGylated liposomal doxorubicin (DOXIL®), albumin-bound paclitaxel (Abraxane®), and polymeric micelle loaded paclitaxel (Genexol®), which are currently used in the clinic as one of the first lines for cancer chemotherapies. These conventional nanomedicines rely on passive-drug targeting taking advantage of leaky tumor vasculature, called the Enhanced Permeability and Retention (EPR) effect. However, delivering biologically active components selectively to the diseased cell, for example, cancer, is highly challenging due to the biological barriers in the body including blood pool cells/proteins, heterogeneous microenvironment, and intracellular degradation. Therefore, the **goal of this dissertation** is to develop nanoplatforms that can deliver the agents of interest in targeted fashion to cancer while bypassing or collaborating with the biological barriers. The **design consideration** of these nanoplatforms centralizes on using simple chemical reactions and cell biology to engineer nanoparticles. The presented nanoparticles were extensively studied and evaluated for their biological functions using *in vitro* and *in vivo* models. These nanoconstructs described herein address current limitations of conventional nanomedicine such as (1) the lack of understanding of the interaction of nanoparticle and biological system, and (2) the lack of an effective targeting strategy to deliver drugs to the cancer cell in the tumors. The significant findings of each system will be highlighted and discussed throughout this dissertation. Results obtained highlight key findings such as nanoparticle intracellular fate, maximized tumor accumulation, and unique pharmacokinetics could open the avenues for systemic investigations for personalized medicine and lay the foundation for nanomedicine design to accelerate clinical translation.

Engineering nanoparticles using chemical and biological approaches for tumor targeted delivery

by

Tuyen Duong Thanh Nguyen

B.Sc., Cantho University, Vietnam, 2014

A DISSERTATION

submitted in partial fulfillment of the requirements for the degree

DOCTOR OF PHILOSOPHY

Department of Chemistry
College of Arts and Sciences

KANSAS STATE UNIVERSITY
Manhattan, Kansas

2019

Approved by:

Major Professor
Prof. Santosh Aryal

Copyright

Abstract

Nanotechnology offers exciting options for the site-selective delivery of chemotherapeutics and diagnostic agents using nanoparticles. Varieties of organic and inorganic nanomaterials have been explored extensively as a delivery system either in the form of drug carriers or imaging agents. Successful stories include the clinical translation of anticancer nanomedicines such as PEGylated liposomal doxorubicin (DOXIL®), albumin-bound paclitaxel (Abraxane®), and polymeric micelle loaded paclitaxel (Genexol®), which are currently used in the clinic as one of the first lines for cancer chemotherapies. These conventional nanomedicines rely on passive-drug targeting taking advantage of leaky tumor vasculature, called the Enhanced Permeability and Retention (EPR) effect. However, delivering biologically active components selectively to the diseased cell, for example, cancer, is highly challenging due to the biological barriers in the body including blood pool cells/proteins, heterogeneous microenvironment, and intracellular degradation. Therefore, the **goal of this dissertation** is to develop nanoplatforms that can deliver the agents of interest in targeted fashion to cancer while bypassing or collaborating with the biological barriers. The **design consideration** of these nanoplatforms centralizes on using simple chemical reactions and cell biology to engineer nanoparticles. The presented nanoparticles were extensively studied and evaluated for their biological functions using *in vitro* and *in vivo* models. These nanoconstructs described herein address current limitations of conventional nanomedicine such as (1) the lack of understanding of the interaction of nanoparticle and biological system, and (2) the lack of an effective targeting strategy to deliver drugs to the cancer cell in the tumors. The significant findings of each system will be highlighted and discussed throughout this dissertation. Results obtained highlight key findings such as nanoparticle intracellular fate, maximized tumor accumulation, and unique pharmacokinetics could open the avenues for systemic investigations for personalized medicine and lay the foundation for nanomedicine design to accelerate clinical translation

Table of Contents

List of Figures

List of Tables

Acknowledgments

Being a Ph.D. student at K-State has been exciting as well as a challenging experience for me. During these years, many people have directly, indirectly, and in different ways, been a part of my journey, and encouraged and supported me along the way.

Foremost, I would like to express my special thanks to my advisor, Prof. Santosh Aryal; you have been a tremendous mentor for me. I would like to thank you for encouraging in my research and for teaching me how to become a research scientist. Your advice on my research and career development has been invaluable. You have set up a great example of who I want to become in the future.

I would also like to thank my committee members, Prof. Stefan Bossmann, Prof. Mark Weiss, Prof. Jun Li, and Prof. Ryan Rafferty for serving as my committee. I am also grateful to Prof. Deryl Troyer who was one of my former committee members. I highly appreciate your guidance and support throughout my Ph.D. program. The valuable discussion with you has helped me to shape my research trajectory and diversify my way of thinking.

I would especially like to thank my former and current colleagues, Dr. Arunkumar Pitchaimani, Dr. Meghana Ramani, Mukund Koirala, Soma Sekhar Sriadibhatla, Ramesh Marasini, Sagar Rayamajhi, Colin Ferrel, Jessica Marchitto, Javier Abello, Achini Eliyapura, Cesar Aparicio, my friends, faculties, and staffs at Department of Chemistry and Nanotechnology Innovation Center of Kansas State University. I am such a lucky girl that I have many special people surrounding me and supporting me in all aspects. Thank you, everyone, for being in my life, making it become so meaningful, and making every bit of my Ph.D. life so special. I am grateful to have all of you around.

Most importantly, I would like to express my special thanks to my family. Words are not enough to express how grateful I am to you, Mom and Dad, for all of the love that you have for me. Thank you for supporting me, believing in me, and encouraging me in this journey. To my beloved sister, Thi Nguyen, you were the one who opened this door for me, gave me the opportunity so that I can become who I am now. I am so lucky to have you there, love me unconditionally, and take care of me on every step that I go. As promised, I will be your elder sister in the next life. Finally, I would like to thank all my family members, friends (there are a long list), and well-wishers for their support through this program.

Dedication

To my mentor

Dr. Santosh Aryal

To my dad and mom

Thien Xuan Nguyen and *Tuyet Thi Bach Duong*

To my beloved sister

Dr. Thi Duong Thanh Nguyen

Without whom this day would never come.

Chapter 1 - Introduction

1.1 The concept of "Nanomedicine"

In 1966, a movie named "Fantastic Voyage" presented a fantasy concept of miniaturizing submarine crews and sending them into a body to dissolve a life-threatening blood clot in the brain. At that time, the concept was just some kind of filmmakers' imagination as millions of other Hollywood movies. They would never have thought that the "miniaturizing" idea for treatment of disease would someday become the foundation of an exciting research area with a rocket rate of development called "nanomedicine". By definition, nanomedicine is a branch of nanotechnology, where the materials in sub 100 nm are investigated for possible prophylactic, diagnostic, and therapeutic applications.[1] The ability to get smaller in size offers new opportunities to reveal exceptional properties of materials and the capability of manipulating individual atoms and molecules.

Thirty years after the "Fantastic Voyage", the first nanomedicine was approved by FDA under the name of DOXIL®, a polyethylene glycolated (PEGylated) liposomal doxorubicin (DOX, a clinical anticancer drug). The use of DOXIL® in cancer treatment has shown significant improvement in diminishing DOX-related cardiotoxicity, enhancement of drug tolerability, and extending overall pharmacokinetic profile in comparison to that of free DOX. Followed by the first successful story, other nanomedicines comprised of protein (Abraxane®), polymer (Genexol®), crystal (Emend®), and inorganic components (NanoTherm®) made their ways to the clinics.[2] To date, various nanomedicines have been developed and commercially available in both clinical and non-clinical areas. Within the USA, more than 50 nanomedicines were approved along with hundreds of other nanoformulations entering various stages of clinical trials (**Figure 1.1**).[2–4]

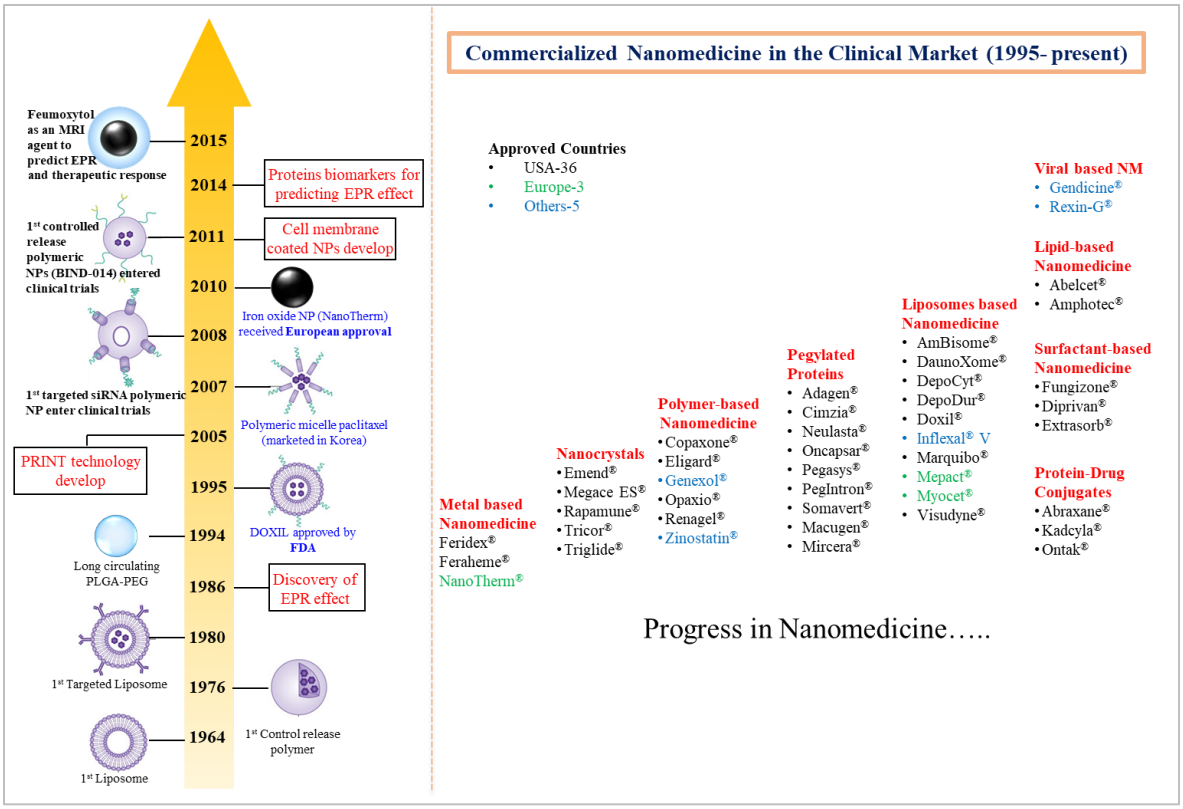

Figure 1.1 The progress in the development of nanomedicine (collected from ref. 5 and 6)

The attractive features of nanomedicine can be accountable for its versatility of modification with a variety of ligands, ability to incorporate both water-soluble/insoluble molecules, the capability of tuning the pharmacokinetic/pharmacodynamics of active components, and the opportunity of combining diagnostics with therapy in a single setting to achieve precision medicine. Varieties of organic and inorganic nanomaterials have been extensively explored as nanomedicine, and they can mainly be divided into two main areas including nanotherapeutics and nanodiagnostics. These two outstanding areas are further forwarded in recent years to explore their combination capabilities to form a multifunctional nanomedicine called theranostics.

1.1.1 Nanotherapeutics for treatment of disease

One of the biggest interest in exploring the area of nanomedicine is to design a nano-sized drug delivery system for the treatment of diseases. The idea of having a “magic bullet”, that can

(1) protect the active ingredient from degradation while traveling in the body and (2) be able to deliver its cargo precisely to the site of action while avoiding off-target effects, has always been an ultimate goal of researcher across the field. Most of the conventional drugs, when injected into the body, exhibit a short circulation time due to their small molecular structures. As a consequence, free drug molecules are often excreted out from the body before they can reach the intended site with the effective therapeutic concentration. The use of a nano-sized carrier for free drug provides an innovative mean of transportation to pass through the traffic jam in the biological system and overcome the shortcomings of conventional formulations. An example can be seen in the case of DOXIL, when free DOX is crystallized and enveloped in a lipid bilayer vesicle with polyethylene glycol decorated outside, the circulation half-life increases from 5 mins to 55 h.[6]

Another aspect that makes nanotherapeutics becoming a "hot" topic, especially in cancer therapy, is driven by the discovery of the "enhanced permeability and retention" (EPR) effect in solid tumor. The EPR phenomenon arises due to the ability to develop a new vascular system in the tumor to enhance the sources of blood and nutrition supply for cancer progression.[7] Consequently, blood vessels in the solid tumor are often highly disorganized and abnormal with unaligned endothelial cells, lack of smooth muscle layer, and poor lymphatic drainage.[7] These unique properties of tumor allow intravenously injected long-circulating nanoparticle to permeate and be retained within the tumor region. The first observation of EPR effect was reported by Matsumura and Maeda in which the injection of high molecular weight protein-polymer-dye complex revealed an extensive accumulation in cancer tissue and slower recovery via blood vessel and lymphatic system in compare to normal tissue when the molecular weight of complex increase from 15,000 to 70, 000 Da.[8] As a result, the ratio of concentration of high molecular weight complex in tumor to blood (T/B) could go up to 5, whereas its counterpart's T/B ratio never

reached to 1.[8] Since then, the EPR effect stood out as a lodestar in designing nanosized drug delivery system. With the demonstrated success in various tumor models, EPR effect has now been widely accepted as a passive targeting strategy to deliver drugs or any kind of cargos to the solid tumor when non-targeted nanoparticles are used as carriers.

1.1.2 Nanodiagnostics for early disease detection

It is a common thought that improved patient outcomes rely on how early and precisely the diagnosis and treatment of a disease can be. To date, medical imaging has become an essential tool for clinical practitioners to assess disease pathology based on anatomical or functional evaluations. As the need of diagnostic imaging has grown significantly in treatment planning, a variety of imaging technologies such as positron emission tomography (PET), computed tomography (CT), optical imaging, magnetic resonance imaging (MRI), X-ray, and ultrasound are becoming routine procedures in the clinics.[9] Aligning with the development of imaging modalities, a wide range of small molecules and molecular complexes used as tracer or contrast agents are also maturing and diversifying over time. These contrast agents or imaging tracers are employed to assist the conventional imaging modality for a clearer visualization of abnormality allowing the diagnosis of previously undetectable pathologies. The advantages of using imaging probes are further pushed forth by incorporating into nanosized materials with the hope of continuing the improvement in sensitivity, stability, and plasma residence times as compared to that of small molecules.

The benefits of using a nanomaterial-based imaging probe have been well-documented in a wide range of imaging modalities.[10–13] For example, when thousands of iron oxide molecules clustering and rearranging to form iron oxide nanocrystals, it becomes strongly paramagnetic to use as MR active agent. Moreover, the confinement of this small molecule or particulate contrast agent in the second stage nanoparticle system provides enhancement in contrast as well as an

increase in targeting specificity. For an instant, tiny iron oxide nanoparticles when confined into sub 100 nm polymeric matrix enhance an order of magnitude of its magnetic relaxivity, which will help on reducing the dose thereby reducing associated toxicity.[14] Gao et. al. encapsulated superparamagnetic iron oxide nanoparticles into the polymeric micelles to enhance the imaging efficacy of tumor biomarker *in vivo*.[15] Similarly, gadolinium (Gd)-based contrast agent in mesoporous silica nanoparticles is reported to be effective in enhancing contrast.[16] In some other cases, the incorporation of gadolinium-based macromolecules into a liposomal system assist the brighter contrast compared to that of the small molecule counterpart via altering water tumbling mechanism.[17,18,16]

1.2 Biological barriers for nano-delivery system

1.2.1 Protein blood opsonization and reticuloendothelial system sequestration

Despite their potential in the pre-clinical trial, the therapeutic impact of the nanomaterial-based delivery system in the clinic remains modest due to the complexity of the biological environment. One of the first obstacles that nanoparticle encounters upon administration is the opsonization and the formation of protein corona.[19] The interaction with these endogenous materials alters the designed properties of nanoparticle preventing them from performing their desired tasks in physiologically relevant condition. In 2013, Tenzer and coworkers identified the 20 most abundant corona proteins that rapidly form onto the surface when silica and polystyrene nanoparticles are treated with human plasma.[20] The constituents of corona highly depend on the physicochemical properties (size, surface chemistry, shape) of nanoparticles, but they all share common proteins including serum albumin, apolipoproteins, complement proteins, and antibodies. The formation of protein corona subsequently conceals the targeting ligands presence on the surface of the nanoparticle and ultimately change its pharmacokinetic behavior. An example can

be seen when transferrin (a transferrin receptor targeting ligand) functionalized silica nanoparticle was used to study the targeting efficiency toward lung cancer cell (A549).[21] The result indicated that no matter if polyethylene glycol (a polymer that is believed to minimize the formation of protein corona) was used or not, the targeting specificity of all nanoparticle formulations toward corresponding receptors on A549 cells was lost upon the exposure to biological serum.[21] In the case of nanodiagnostics, the binding of protein is more severe as it is also responsible for causing fluorescent quenching effect in optical imaging modality,[22,23] reducing relaxivity of MRI contrast agent due to metal displacement competition with endogenous ions,[24,25] and accelerating the decay rate of nuclei in PET.[26]

Following the formation of protein corona, nanoparticles exhibit a new biological identity which is far different than its original synthetic characteristic. As a consequence, nanoparticle‘s unexpected biological events are initiated due to the recognition of resident macrophages of the mononuclear phagocyte system (MPS). The sequestration by MPS results in high accumulation of nanoparticles in organs, such as the spleen and the liver, preventing it to navigate to the targeted location successfully. More than 31.30% of targeted and 62.33% non-targeted gold nanoparticles (55nm) injected dose were found in reticuloendothelial system organ such as liver.[27] With this excessive excretion phenomenon, just 0.7% of injected nanoparticle dose could make its way to solid tumor as reveal in a meta-analysis of literature related to nanoparticle-based drug carriers conducted by Wilhelm et al.[28]

1.2.2 Tumor-microenvironment

Once the remaining small portion of nanoparticles get to the site of action, it continues to experience other obstacles in the disease microenvironment. Taking tumor as an example, tumor microenvironment is highly heterogeneous encompassing with fibroblast, stromal cells, and

immune cells along with distinct intratumoral conditions such as hypoxia, acidic pH, and interstitial pressure gradients.[29] Such complex cellular network and physiological condition within tumor microenvironment making delivering the drug to the cancer cell becomes highly challenging (**Figure 1.2**).

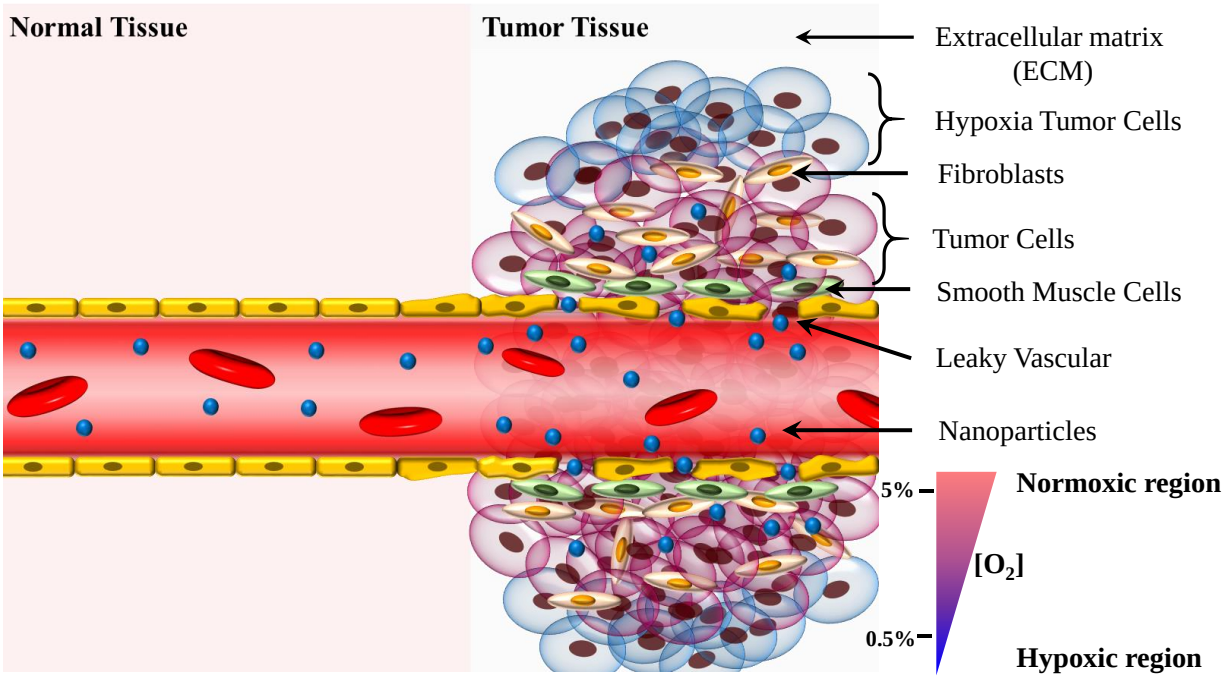

Figure 1.2 Schematic demonstrates the physiology of solid tumor encompassing with fibroblast, stromal cells, and the gradient of oxygen level along with necrotic and hypoxic regions.

Tumor-associated endothelial, pericytes, and fibroblast cells: Apart from the cancerous cell, the tumor microenvironment contains other cells that create structural support and generate neovascularization for cancer growth. The thick layer of these cells surrounding the cancerous region hindering nanoparticle extravasation efficiency. Intractable pancreatic cancer is a good example of this scenario.[30] The use of DOXIL® for the treatment of pancreatic cancer-bearing mouse model showed a minimal effect on tumor volume reduction.[31] However, when DOXIL was used with TβR-I inhibitor that can decrease the coverage of pericyte in the neovasculature of pancreatic tumor, the accumulation, and antitumor efficiency was significantly increased.[31,32]

Tumor-associated immune cells: Throughout tumor development, cancer cells behave like a "never healing wound" to recruit immune cells and turns them into their "partners". Variety of immune cells including T-cell, B-cells, Natural Killer Cell, macrophages, dendritic cells, and neutrophils can be found in the tumor region. These cells play an important role in tumorigenesis and tumor progression. In the context of drug delivery, the phagocytic cells located in the tumor area serve as nanocarriers' digesters, which responsible for capturing nanoparticles before they even have a chance to get close to cancer cells. As a result, 90% of intratumoral nanoparticles were found to be residing in tumor-associated macrophages or other non-cancerous cells, leading to just 0.001%-0.003% nanoparticle injected dose found in cancer cells of human ovarian SKOV-3 xenograft mouse model.[27]

Acidic pH: In comparison with the pH in normal tissues, the pH of the tumor extracellular matrix (pH_e) is slightly acidic with pH value around 6.0.[33] The acidity found in the tumor region is a result of excessive glucose metabolism under anaerobic condition of cancer cells so-called "Warburg effect", leading to the increased production of lactic acid and protons intracellularly.[34,35] These acidic metabolites are then transferred in the extracellular milieu causing the acidic physiological condition. The gradient of acidic pH_e appears as a barrier to drug delivery due to its ability to switching the charged state of the carriers and chemotherapeutic molecule, which further reduce the probability for active component reaching the cancer cell.

Hypoxia is a pathological phenomenon used to depict the location where the shortage of oxygen occurred.[36,37] Hypoxia has long been recognized to associate with various intractable diseases such as rheumatoid arthritis, tumor, ischemic heart disease, and stroke.[37] In solid tumor, this phenomenon arises due to disorganization of the vascular network, sluggish, and irregular blood flow generated during the aggressive growing process of cancer.[38] Such altered vasculature

consequently leads to a heterogeneous oxygen gradient within tumor microenvironment, where an extremely low partial pressure of oxygen (pO_2) is present **(Figure 1.2)**. Indeed, the median pO_2 in breast tumor microenvironment accessed by electrode measurement revealed a value of 10 mmHg, which is 6 folds lower than that of normal breast tissue.[39,40] In order to adapt to such severe conditions, cancer cell at hypoxic region must undergo a genetic modification to continue their survival and proliferation.[41] Consequently, these hypoxic cells become even more aggressive and untreatable which have been linked to increased metastasis, and resistance to radiotherapy and chemotherapy.[36,41,42]

1.2.3 Intracellular environment

When nanoparticles are near cancer cells, a series of events take place before the nanoparticle‘s encapsulated cargo reach its intracellular target. The nanoparticles first attach to the cell surface via a non-specific or specific binding manner. Subsequently, bound nanoparticles trigger the cellular endocytic pathway to be transported across the cell membrane.[43] Via this process, the nanoparticles get trapped in the acidic endosomal compartment (pH~6).[44] These endosomal vesicles later mature to become late endosomes, lowering the pH further to ~5. The nanoparticle contained late endosome can continue to fuse to lysosome at which point the acidic pH of ~4.5 and presence of enzymes start the process of nanoparticle digestion and degradation.[44] As a result, the bioactive molecules are also destroyed with its carrier before they can get to the intracellular intended targets.

1.3 Scope of dissertation

Since the first nanosized delivery system was invented and approved by FDA, significant efforts have been given to obtain an optimized nanocarrier to bypass biological system and advance the therapeutic and diagnostic efficiency of drugs and contrast agents. Within the past 10

years, we observed an exponential increase in publications focusing on the topic of "nanomedicine". However, although an extensive amount of research has been devoted to nanoparticle development, only a handful of nanoparticulate systems find their way to FDA approval. The retardation in the clinical translation of nanomedicine is a direct consequence of the nanoparticle's inability to overcome many of the above mentioned biological barriers.

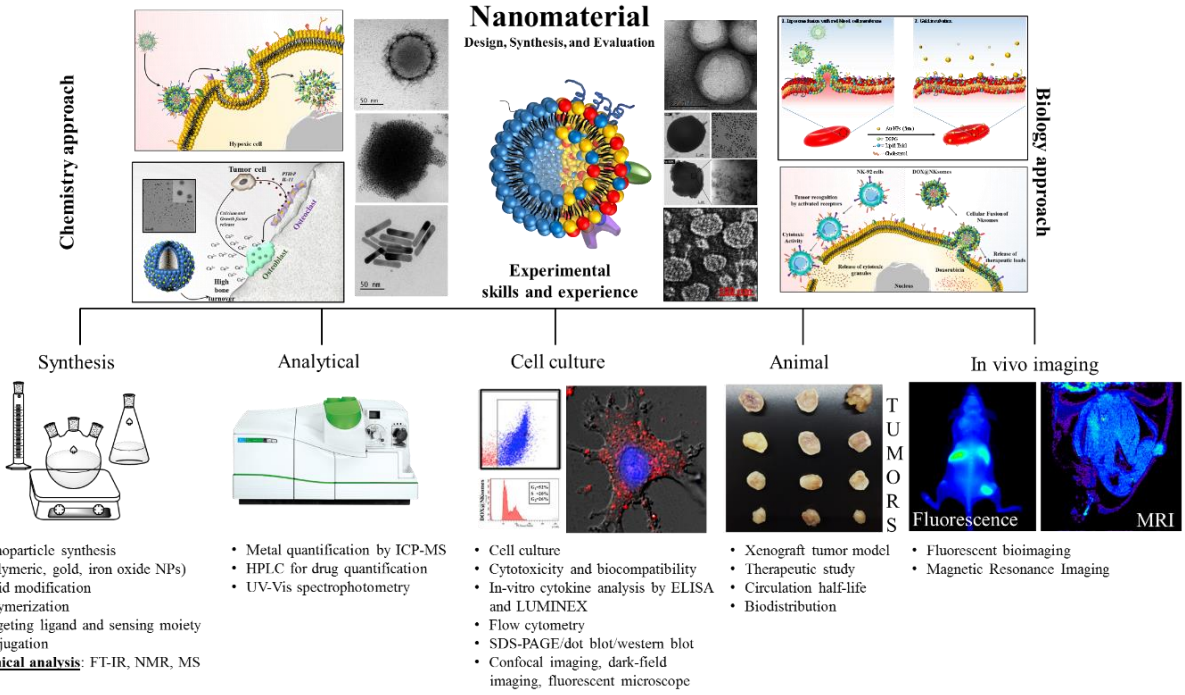

Figure 1.3 Scope of the dissertation for developing nanomaterials using chemical and biological tools to study their biological functions for cancer diagnosis and therapy

1.3.1 Central objective

The central objective of this dissertation is to put forth the engineering strategy of nanomedicine using chemical and biological approaches (**Figure 1.3**). The proposed nanomedicines were extensively studied and evaluated for their biological functions in term of cancer diagnosis and therapy. Via the new design considerations, the nanoconstruct described

herein addresses the current limitations of the conventional nanoparticle. The significant findings of each system will be highlighted and discussed throughout this dissertation.

1.3.2 Chemistry approach

Under the chemical approach, targeted drug delivery systems which are made up of poly(lactic-co-glycolic acid) (PLGA) cores containing chemotherapeutic drug doxorubicin (DOX) and decorated peripherally by Alendronic acid-a bone targeting agent was developed (**Chapter 2**). The engineered nanoconstruct exhibit combinatorial actions including targeting and therapy for the treatment of cancer occurring in the bone. As a one step forward from the project, the nanomaterial was further advanced by incorporating contrast agent that can partner with Magnetic Resonance Imaging to enhance the effectiveness of early and non-invasive cancer diagnosis. In the approach, a confinement strategy was used to enhance the magnetic property of superparamagnetic iron oxide nanoparticle (SPIONs) (**Chapter 3**). By controlling the cluster density of SPIONs in the polymeric core of targeted nanoconstruct, we successfully tuned the magnetic properties of magnetic nanosystem up to 641 $mM^{-1}.s^{-1}$. The magnetic property of engineered nanoconstruct is five times higher than that of the clinically used contrast agent such as Feridex® (r_2 = 120 mM^{-1} s^{-1}). With these results, we moved forward to test our nanomaterial using tumor-bearing mice model where we could observe the accumulation of SPIONs in the tumor by enhancing dark contrast at the tumor site.

1.3.3 Biology approach

On the other hand, under the biological approach, a biomimetic system that can communicate with our immune cells for precise delivery of chemotherapeutics and contrast agents to cancer was investigated. In this approach, the nanoparticle surface was modified with Natural Killer (NK) cell membrane and Magnetic Resonance Imaging (MRI) contrast agents (**Chapter 4**).

Since a NK cell naturally seeks and destroys cancer cells, the incorporation of its membrane onto the synthetic nanoconstruct could work in a similar manner to that of naïve NK cell. With the biomimetic nanosystem, that has advantages of both synthetic and biological derived materials, NK cell membrane coated nanoconstruct has been studied the tumor targeting *in vivo* for bioimaging and precise drug delivery. In addition, to further explore the structural relationship of cell membrane coating and MR contrast agent, a red blood cell membrane disguised gadolinium-based polymeric nanoconstruct was fabricated (**Chapter 5**). This study resulted in an optimized red blood cell membrane disguised gadolinium-based polymeric nanoconstruct for tunable T_1 relaxivity to elucidate their corresponding MR mechanism on image enhancement output and biological performance under *in vitro* and *in vivo* condition. The isolated RBC membrane directly fused onto polymeric core pre-labeled with gadolinium lipid conjugate. The biomimetic strategy allowed to conceal contrast agent from the endogenous components, resulting in a long circulating and high longitudinal relaxivity of blood pool contrast agent for improved MRI visualization of the vascular lumen.

Chapter 2 - Engineering nanomedicine with Alendronic acid corona improves targeting to Osteosarcoma

***Chapter 2**, in full, is a reprint of the material as it appears in Scientific Reports, 2016, Tuyen Duong Thanh Nguyen, Arunkumar Pitchaimani, and Santosh Aryal. doi: 10.1038/srep36707*

Abstract

We engineered nanomedicine with the stealth corona made up of densely packed bone-seeking ligand, alendronic acid. In a typical nanoconstruct, alendronic acid is conjugated with hydrophilic head moiety of phospholipid that has an ability to self-assemble with hydrophobic polymeric core through its hydrophobic long carbon-chain. Proposed nanomedicine has three distinct compartments namely; poly(l-lactic-co-glycolic acid) polymeric core acting as a drug reservoir and skeleton of the nanoconstruct, phospholipid monolayer covers the core acting as a diffusion barrier, and a densely packed alendronic acid corona acting as a stabilizer and targeting moiety. Thus engineered nanomedicine attain spherical entity with $\sim 90 \pm 6$ nm having negative zeta potential, -37.7 ± 2 mV, and has an ability to load 7 ± 0.3 wt% of doxorubicin. *In vitro* bone targeting efficiency of nanomedicine was studied using hydroxyapatite crystals as a bone model, and found significant accumulation of nanoparticle in the crystals. Moreover, cellular internalization studies with mouse osteosarcoma confirm the selectivity of nanomedicine when compared to its internalization in non-targeted mouse melanoma. This nanomedicine shows prolong stability in serum and deliver the drug into the cell exhibiting an IC50 of 3.7 μM. Given the strong interacting property of alendronic acid with bone, the proposed nanomedicine hold promises in delivering drug to bone microenvironment.

2.1 Introduction

According to the American Cancer Society, an estimated 3,300 new cases of primary bone cancer are expected to occur during 2016.[45] Although this number just accounts for 0.2% of new cancer diagnoses, bone is one of the most common sites to depot migrating cancerous cells from distant organs owing to its largest bodily scaffold covering from head to toe around compartmentalized organs. Every year, approximately 80% of breast, lung, and prostate cancer patients ultimately develop bone metastasis, which further entry the disease into an incurable phase.[46,47] Since the connection between bone microenvironment and cancerous cells was proposed by Stephen Paget in 1889, this metastatic phenomenon has been extensively studied and widely accepted as "soil and seed" relation in which the unique property of bone microenvironment provides favorable environment for cancerous cells to develop, survive, and proliferate.[48,49] Specifically, once cancerous cell homing to bone marrow, it starts to interfere bone remodeling process by a complex cascade of events including upregulating the expression of receptor activator of nuclear factor κB ligand (RANKL); thereby, activating bone resorption via receptor activator of nuclear factor κB (RANK) on osteoclast to assist its growth and expansion.[50–52] This in turn leads to bone being broken down without new bone being made i.e.; immoderate production of osteoclasts, or bone being made without breaking down old bones i.e.; excessive production of osteoblasts. With the abnormal acceleration or deceleration in osteoclasts and osteoblasts production, bone releases its mineral, becomes more fragile, porous, and consequently leads to bone fracture.

Despite intensive efforts in the development of therapeutic agent for cancer occurring at bone, tumor localized in bone still remains as an incurable fatal disease due to either the fast clearance or non-specific binding profile of therapeutic agents. In addition, due to the solid

composition and larger surface area of bone, targeting therapeutics to the desire location is the major problem in treating bone cancer. The difficulty of eliminating bone-residing cancer necessitates novel alternative treatment regimens to manipulate the tumor cells, drug resistance, and their microenvironment, with minimal off-target effects.

Among different types of bone targeting ligands, bisphosphonate has been long emerging as a bone-seeking agent owing to its greatly binding affinity with hydroxyapatite - a major mineral component in bone environment. In addition, with the acidic property and hydrophilic nature, bisphosphonate's permeability through cellular membrane is insignificant, which in turn makes it more extensively accumulates in skeleton than other organs after the administration.[53,54] Once considering bisphosphonate's distribution within skeletal system, researchers have shown that bisphosphonate accumulates more in bone defect site where high bone turnover is associated.[55,56] High bone turnover occurs when the activity of osteoclasts and osteoblasts are uncontrolled or are aggressive. Taking an advantage of these properties at bone lesion sites, the bisphosphonate conjugation can be a promising approach to design targeted chemotherapy for bone cancer treatment. Moreover, the antiresorptive properties of bisphosphonate makes it suitable combination candidate with other drugs to treat cancer at bone.[57]

Recently, studies have been focused on utilizing bisphosphonate to construct bone-homing nanomedicine by either conjugating alendronic acid (a member in bisphosphonate class) with polymeric backbone or chemotherapeutic drugs via polyethylene glycol (PEG) linker.[58–62] These targeted nanocarriers possess common stealth properties provided by well-hydrated PEG moiety decorated on the surface which could evade nanoparticle from reticuloendothelial system (RES). In 2006, Uludag et. al., reviewed on attempt to engineer bone seeking therapeutic agents based on formulating therapeutic agents with bisphosphonates.[63] In this review authors have summarized

various classes of bisphosphonate and therapeutic agent conjugates such as: small molecule drugs, protein, and imaging agents capable of targeting bone. In recent study conducted by Swami et. al., bortezomid, a proteasome inhibitor, loaded polymeric nanoparticle was proposed, in which the stealth PEG corona was conjugated with alendronic acid to target bone.[61] Despite promising achievements in enhancing antitumor activity on mice-bearing tumor models, a number of limitations and challenges related to those systems need to be considered. For examples, the acceleration on using PEG moiety in both pharmaceutical and non-pharmaceutical products have consequently leaded to anti-PEG antibody development in human body.[64–68] Recent finding shows that 22-25% occurrence of anti-PEG in healthy blood donors is most probably due to the greater exposure to PEG containing consumer products.[68] Therefore, a substitute material need to be developed in order to diminish the excessive usage of PEGylated products. Considering the important role of hydrophilic corona layer on the surface of nanoconstruct in stabilizing nanosystem, we hypothesized that the Alendronic acid moiety with hydrophilic phosphate groups could provide favorable environment for water to form hydration layer around the particle protecting it from opsonization when properly structured in nanoconstruct and further sustain the stability of nanosystem under physiological condition.

To this end, we proposed a targeted nanoparticle (TNP) which is made up of Alendronic acid modified lipid and PLGA polymeric core encapsulating chemotherapeutic drug - Doxorubicin (DOX) to simultaneously offer combinatorial actions including targeting and therapy of bone cancer treatment. Proposed nanostructured construct has three distinct layers (1) PLGA core acting as a skeleton of the nanoparticle and drug reservoir, (2) lipophilic phospholipid layer acting as a middle passivating layer and diffusion barrier for the encapsulated drug, and (3) hydrophilic alendronic acid, an outer corona layer, acting as stabilizer and driving of nanoparticle to its target

(**Figure 2.1**). This densely packed phospholipid conjugated alendronic acid creates a sufficiently thick hydrated shell and prevents nanoparticle from being disassembled. Therefore, the engineered nanomedicine not only has stealth properties providing by bone mineral targeting moiety but also deliver a large quantitative amount of therapeutic agent which could enhance the effectiveness of treatment.

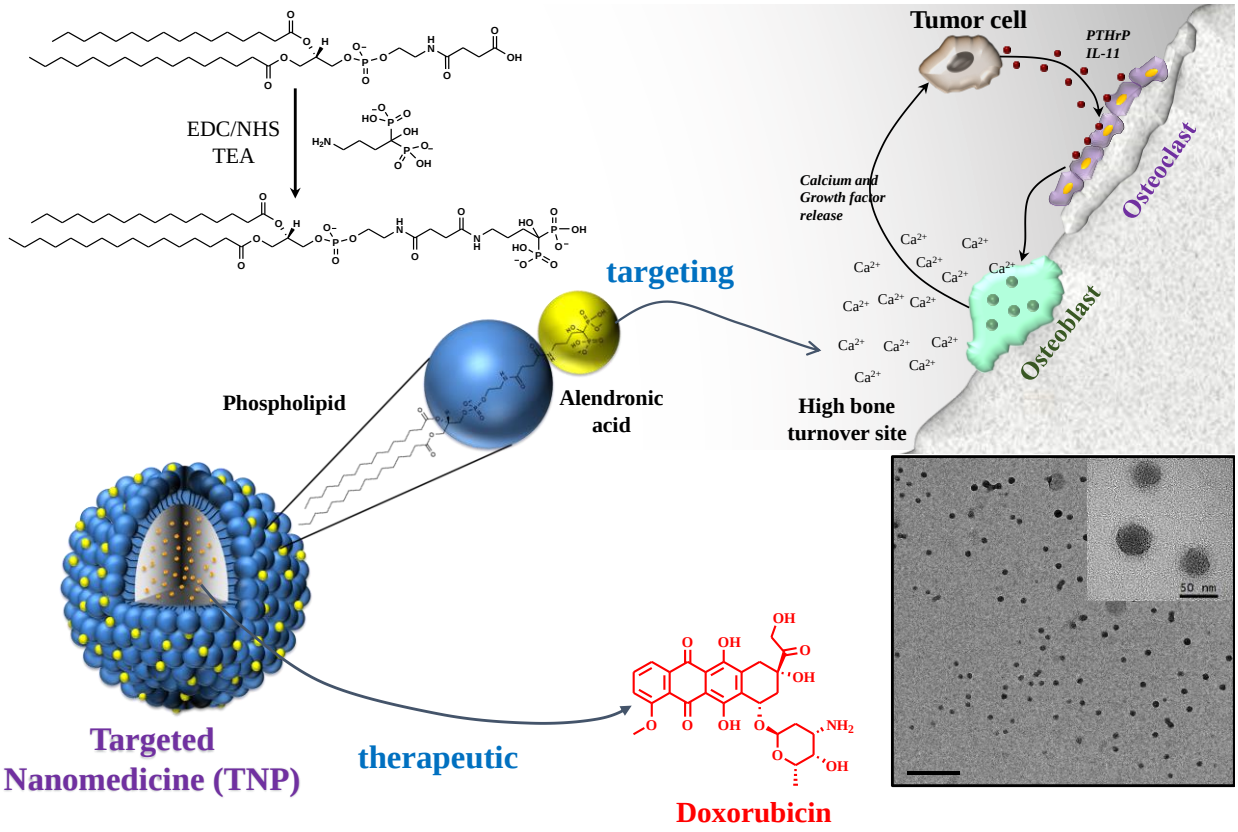

Figure 2.1 Design of proposed bone targeted nanoconstruct. The Alendronic modified phospholipids drive nanoparticle containing chemotherapeutic drug (Doxorubicin) to the high bone turn over site where tumor occur.

2.2 Materials and Methods

Chemicals and reagents.

Poly(D,L-lactide-co-glycolide) carboxylate end group (50:50, 0.55-0.75 dL/g) was purchased from DURECT Corporation (Birmingham, AL, USA). 1,2-dipalmitoyl-sn-glycero-3-phosphoethanolamine-N-(succinyl) (sodium salt) (16:0 Succinyl PE) and L-α-Phosphatidylethanolamine-N-(lissamine rhodamine B sulfonyl) (Ammonium Salt) (Egg-Transphosphatidylated, Chicken) (Egg Liss Rhod PE) were purchased from Avanti Polar Lipid Inc. (Alabaster, AL, USA). Alendronic acid was purchased from TCI America. 1-ethyl-3-(3-dimethylaminopropyl)carbodiimide hydrochloride (EDC) and N-hydroxysuccinimide (NHS) were purchased from Sigma-Aldrich (Milwaukee, WI, USA). Doxorubicin hydrochloride salt was purchased from LC Laboratories (Woburn, MA, USA). Osteosarcoma Cell line K7M2 and Mouse Melanoma (B16-F10) were purchased from ATCC and maintained according to the manufacturer's recommendation. All other chemicals and solvents were purchased from Sigma-Aldrich (Milwaukee, WI, USA) and used as received.

Synthesis of lipid bisphosphonate conjugates.

Alendronic acid conjugated lipid (ALE-lipid) was synthesized by simple coupling chemistry initiated by EDC and NHS. Briefly, 15 mg of Succinyl PE lipid was dispersed in 2-(*N*-morpholino)ethanesulfonic acid (MES) buffer (4 mL, pH=4.5), activated by 35.9mg EDC and 37.5mg of NHS and stirred at room temperature for 15 min. To this 47.4 mg Alendronic acid (ALE) in 6 mL Phosphate Buffered Saline (PBS) containing 10% triethylamine (TEA) was added and stirred for additional 24h at room temperature. In order to purify product, conjugated lipid was placed inside the benzoylated cellulose dialysis bag (MWCO ~500 Da), and dialyzed against water

for 24 hours at room temperature. The samples were lyophilized to obtain a dry powder and stored at -20ºC for further use. FT-IR and ^{1}H-NMR were used to confirm the formation of ALE-lipid.

Nanofabrication of lipid bisphosphonate nanoparticles and multifunctional polymeric nanoparticles.

Targeted hybrid nanoparticles were prepared by single step nanoprecipitation. In brief, 400µL of PLGA (1mg) in acetonitrile was added drop wise to 2 mL of 200µg ALE-lipid (dispersed in 4% ethanol) under magnetic stirring condition at 60ºC. To this, 1 mL of Mili-Q water was added to cool down the mixture and stirred continuously for additional 1 hour to facilitate the formation of nanoparticles and evaporation of organic solvent at room temperature. The TNPs were further purified using Amicon Ultra-4 centrifugal filter (Millipore, MA) with a molecular weight cut-off of 10kDA and stored at 4ºC for further use.

For DOX-loaded TNP preparation, different amount of DOX (10, 25, 50, 100, and 150 µg) were mixed with 100 µL of PLGA (10 mg/mL) and dried under vacuum. Polymeric film with drug was then dissolved in 400µL acetonitrile prior to nanoparticle preparation. Controlled PLGA nanoparticles were also prepared by dropwise adding 100 µL of PLGA (1mg) in acetonitrile to 1 mL of Milli-Q water and purified following aforementioned protocol.

Rhodamine dye labelled TNPs were also prepared by hydrating 20µg of L-α-Phosphatidylethanolamine-N-(lissamine rhodamine B sulfonyl) (Ammonium Salt) (Egg Liss Rhod PE) film with 200µL ALE-lipid (1mg/mL) before performing nanoprecipitation process.

RhB-labeled PEGylated nanoparticles were prepared by adding 400µL PLGA (1mg) into 2mL 4% ethanol containing 200µg DSPE-PEG-suc, 260µg DSPG, and 20µg of L-α-Phosphatidylethanolamine-N-(lissamine rhodamine B sulfonyl) (Ammonium Salt) (Egg Liss Rhod

PE) under magnetic stirring condition at 60ºC, followed by addition of 1mL Milli-Q water and purified as described above.

Characterization of nanoparticles.

The hydrodynamic size and zeta potential measurements of the prepared TNPs and DOX-loaded TNPs were analyzed by Dynamic light scattering (DLS) using a Zeta sizer Nano ZSP (Malvern, Worcestershire, UK). The Smoluchowski model was used to calculate the zeta potential value. All data represents the average of triplicate measurements of samples prepared in different preparations. The morphology of the prepared TNPs was further analyzed using Transmission Electron Microscope (TEM, Tecnia G2, Spirit Bio TWIN). TEM samples were prepared by drop casting and evaporation technique using fomvar coated cupper grid (400 mesh). TEM images were analyzed by GATAN digital imaging system (GATAN, Inc.). The amount of encapsulated DOX and the resulting encapsulation efficiency was quantified spectrophotometrically using UV-VIS microplate reader by measuring the absorbance at 490 nm.

Stability study of nanoformulation.

The stability of TNPs in physiological ionic condition was investigated at pH 7.4 using PBS. In brief, 500 µL of 1mg/mL nanoparticles suspension were added to 500 µL of 2X PBS and incubated at 37ºC with rotating motion for 7 days. The stability of nanoparticles was determined by measuring the particle size and PDI every 24hr. The serum stability of the prepared PLGA NPs and TNPs were carried out as reported. [69–71] Specifically, 100µL of 1 mg/mL nanoparticles were incubated with 100µL of 10% Fetal Bovine Serum at 37°C and measure its change in absorbance at 560nm kinetically every 5s over a period of 1h, double-orbital shaking with slow speed was applied prior to each measurement using Microplate reader (BioTek, Synergy H1 hybrid reader).

Calcium binding affinity.

Nanoparticles engineered herein are highly monodispersed and recovered as aqueous suspension. Under mild centrifugation (1000 to 3000 rpm for 10 mins), they are not pelleted down. We have taken this advantages for Ca^{2+} binding assay. The binding affinity of TNPs to Calcium was determined indirectly by measuring the fluorescence intensity of RhB-labelled NPs presence in supernatant and compare to the initial fluorescence intensity of NPs fluorescent spectrophotometrically. To optimize binding assays, we first used different concentration of RhB-labelled TNPs (100, 200, 400, 600, 800, and 1000 µg/mL) to incubate with 5 mg Hydroxyapatite (HAp) for 30 mins at 37°C. At the end of incubation time, samples were centrifuged at 1,500 rpm for 5 min to spin down HAp aggregates and the nanoparticles that bound to them. 100 µL of supernatant was used to indirectly quantify the relative amount of nanoparticles bind to HAp. In the case of kinetic binding experiment, 1 mL of RhB-labelled TNPs (100 µg/mL and 1 mg/mL) were incubated with 5 mg HAp in macro-crystal form for varying periods of time (30s, 2, 5, 15, 30, 60, 120, and 240 mins) at 37°C and processed as aforementioned protocol. In addition, RhB-labelled PEGylated NPs (100µg/mL and 1 mg/mL) were used as controlled particles followed the same experimental condition.

Drug release study.

The cumulative drug release from the DOX loaded TNPs was assessed under physiological condition at 37°C. In brief, DOX loaded TNPs (25µg/mL, 1mL) were placed in a dialysis bag membrane (Mw. Cutoff=10kDa) and dialyzed against 250mL of PBS (pH=7.4). At constant stirring (100 rpm), 200µL of sample was taken at predetermined time intervals. The amount of released DOX was quantified by measuring the DOX fluorescence with the excitation and

emission wavelength of 490nm and 580nm, respectively. As control experiment, 25µg/mL of Free DOX was placed in a dialysis bag and processed under the same condition.

Intracellular uptake study.

In order to verify cellular uptake efficiency of ALE-Lipid decorated NPs, RhB-labeled TNPs was used in mouse Osteosarcoma bone cancer cell line (K7M2). In brief, cells were seeded in Poly-D-lysine coated 8 chamber slide at a density of 50,000 cells per well and incubated for 24h. Then, the cells were treated with 50µg/mL RhB-labeled TNPs suspension prepared in complete DMEM and incubated for 4h. After incubation, treated cells were washed twice with 1X PBS (pH 7.4), fixed with 4% paraformaldehyde for 30 min at room temperature, stained with DAPI for additional 10 min and imaged under a Confocal Laser Scanning Microscope (Carl Ziess, LSM-700).

Fluorescence-activated cell sorting (FACs) studies.

To quantitatively evaluate the cellular internalization efficiency of ALE-Lipid decorated NPs, a comparative experiment was conducted on targeted Osteosarcoma cell line and non-targeted Melanoma (B16-F10) cells. In brief, K7M2 cells (or B16 cells) were seeded in T25 tissue culture flasks at 4×10^6 cells per flask for 24 hr. After incubation, cells treated with 2 mg RhB-labeled TNPs suspended in DMEM. Cells were then incubated at 37°C at varying periods of time (30 min, 1, and 3 h) at 37°C. After incubation, cells were washed twice with ice-cold PBS, detached with 0.08% w/v trypsin and analyzed on a flow cytometer. RhB-labeled PEGylated NPs at the same concentration were used as control particles.

***In vitro* cytotoxicity assays.**

The *in vitro* cytotoxicity of TNPs was conducted on Osteosarcoma K7M2 using MTT assay. In brief, 2 x 10^4 cells per well in DMEM medium were seeded in a 96-well plate and incubated for 24h. After incubation, the media were replaced with different TNPs concentration (10, 25, 50, 100, 150 and 200µg/mL) and DOX loaded TNPs along with free DOX (0.01, 0.05, 0.1, 0.5, 1, 2, 3 and 5µM) and incubated for additional 24, 48, and 72 hr. Control cells were also maintained without any TNPs treatment (n=6). After incubation, MTT was added to each well and further incubated for 3h according to the manufacturer recommendation. The insoluble formazan crystals were solubilized using DMSO and their absorbance was recorded at 570 nm using a microplate reader (BioTek, Synergy H1 hybrid reader).

2.3 Results and discussion

Synthesis and characterization of ALE-Lipid conjugate.

The synthesis of the lipid conjugate was carried using ethylcarbodiimide hydrochloride/N-hydroxysuccinimide (EDC/NHS) conjugation chemistry as described in **Figure 2.2A**. The chemical structure of synthesized ALE-Lipid conjugate was confirmed by FT-IR and ^{1}H-NMR. As shown in **Figure 2.2B**, the FT-IR spectrum of ALE-Lipid (spectrum in black) exhibits all of the characteristic peaks of both unconjugated lipid (spectrum in blue) and alendronic acid (spectrum in red) including strong signal of aliphatic C-H stretch at 2900 cm^{-1} corresponds to lipid backbone and broad O-H stretch at 3500-3100 cm^{-1} belongs to ALE moiety (**Figure 2.2B**). It is notable that after the conjugation, C=O acid stretch of lipid at 1750 cm^{-1} was shifted to 1650 cm^{-1} due to the formation of C=O amide. Most importantly, broad peak ranges at 1300-750 cm^{-1} corresponds to phosphate functional groups was broaden in ALE-lipid spectrum which could be attributed to the overlap of

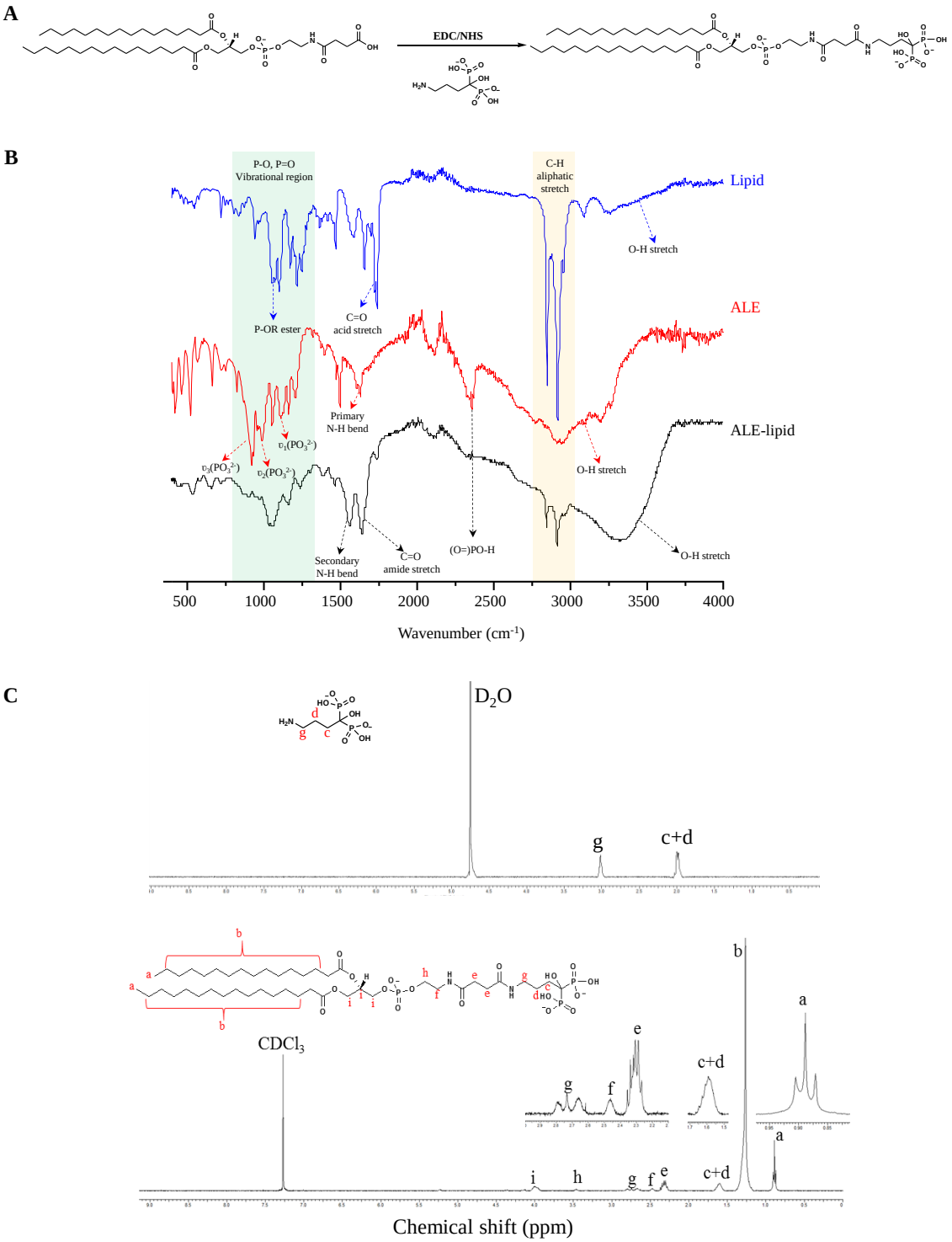

Figure 2.2 Chemical characterization of synthesized ALE-lipid. (A) Coupling reaction scheme. (B) FT-IR spectrum showing functional peaks of starting materials (Alendronic acid, Lipid) and product (ALE-Lipid). (C) ^{1}H-NMR spectra of Alendronic acid in D_2O and ALE-lipid in $CDCl_3$ and its corresponding proton signals.

phosphate ester (1050 cm^{-1}) and phosphonate vibration (985 cm^{-1}, 1050 cm^{-1}, and 1205 cm^{-1}) of lipid and ALE, respectively. In addition, the primary N-H bend (1700 cm^{-1}) in ALE spectrum was replaced by secondary N-H bend (1550 cm^{-1}) in the spectrum of conjugated product; thereby confirming the formation of amide bond. Furthermore, in order to understand the structure of ALE-lipid in detail we conducted ^{1}H-NMR study. In the ^{1}H-NMR spectrum **(Figure 2.2C),** Alendronic acid gave a simple spectrum characterized mainly by a triplet at 2.91 ppm corresponding to N-C$\underline{H}_2$ protons and two complicated multiplets arise at 1.9 ppm and 1.88 ppm due to magnetically non-equivalent nature of prochiral C$\underline{H}_2$ protons.[72] In the case of synthesized ALE-Lipid, proton signals that relate to lipid were observed at 1.26 ppm owing to the methylene groups of long hydrocarbon chain and proton signals of terminal methyl group appear as a triplet at 0.88 ppm. The presence of ALE moiety in conjugated product was confirmed by a small broad peak appears at 1.6 ppm and triplet locates at 2.73 ppm which were assigned for -CC$\underline{H}_2$C$\underline{H}_2$CH$_2$NHCO- and C$\underline{H}_2$NHCO-, respectively. With the formation of ALE-Lipid conjugate these proton signals were upfield shifted from their original chemical shift to 1.8 ppm and 2.91 ppm (in ALE spectrum), respectively, due to the emergence of amide bond and the attachment of lipid, which further verifies the presence of covalently conjugated ALE on fatty acid backbone.

Physicochemical properties of nanoparticles.

After successfully attaching ALE with lipid (ALE-lipid), conjugate ALE-lipid was used along with PLGA and DOX for nanofabrication of TNP and DOX-loaded TNP using nanoprecipitation (**Figure 2.3A**). The physicochemical properties and morphological characterization of TNP and DOX-loaded TNP were determined using dynamic light scattering (DLS), surface zeta potential, and transmission electron microscopy (TEM) as shown in **Figure**

2.3 B, C, and **D** respectively. The hydrodynamic size of the TNP showed a diameter of 69±5nm whereas DLS size

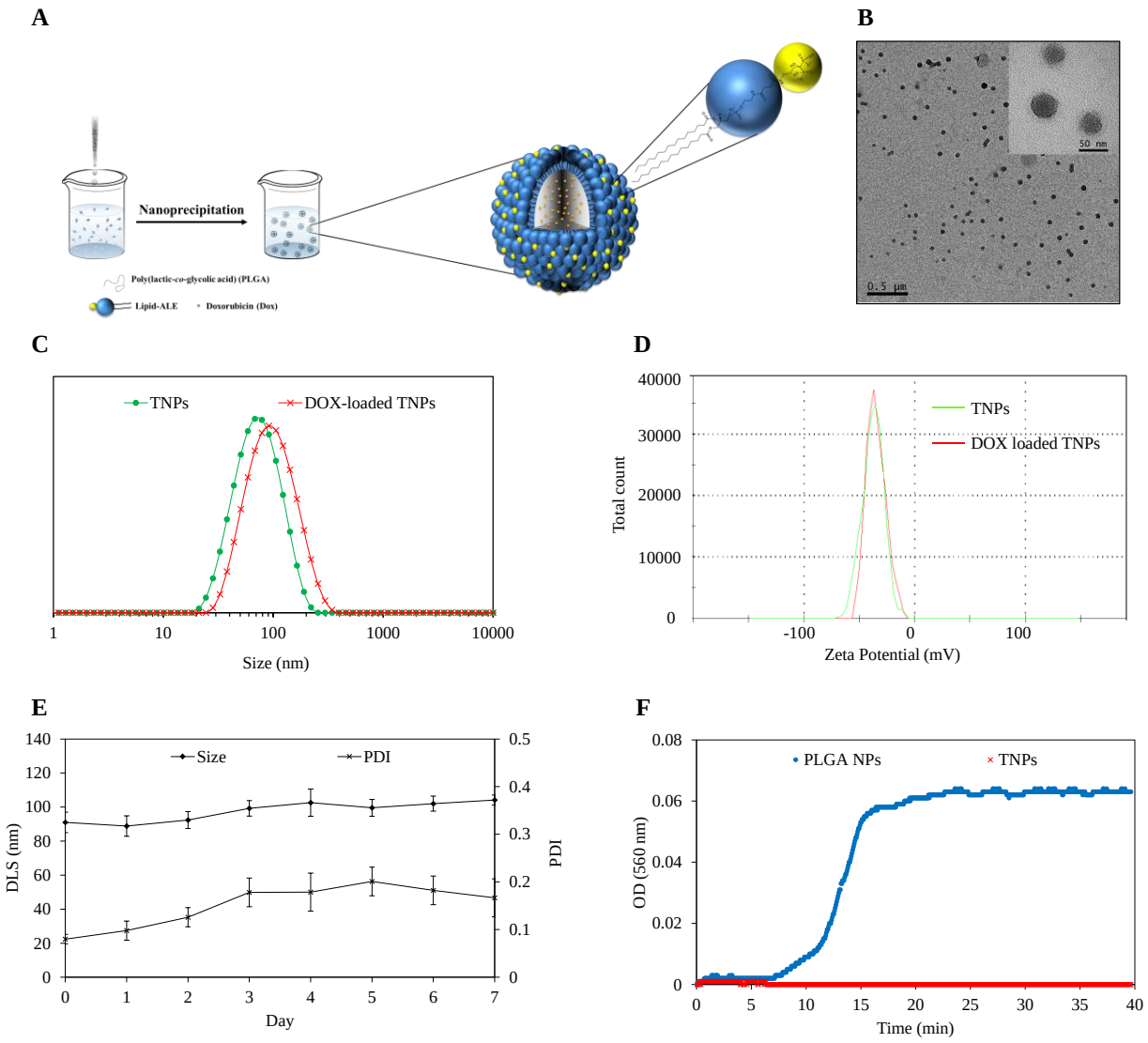

Figure 2.3 Characterization of TNPs. (A) Schematic demonstrates nanofabrication technique and components of TNPs. (B) TEM showing morphology and uniformity of TNPs. (C) Dynamic light scattering showing hydrodynamic size of TNPs and DOX-loaded TNPs. (D) Surface charge Zeta potential. (E) Stability test conducted in ionic condition (PBS, pH 7.4). (F) Kinetic stability study in 10% Fetal Bovine Serum (FBS). Values represent mean ± s.d., n = 3.

of DOX-loaded TNP was found to be 90±6nm. Importantly, in both cases, the DLS data showed unimodal distribution with low poly dispersity index (PDI) which demonstrates that the TNP and DOX-loaded TNP are highly monodispersed in aqueous solution. The TEM image of TNP further confirmed the uniformity of nanoparticles with the size is around 50 nm. The significant different between hydrodynamic size and dry-stage diameter is likely due to well thick hydrating layer in which the densely packed hydrophilic phosphate moiety acting as a corona of nanoparticle. This hydrophilic corona layer works in a similar way to that of PEG moiety which could make nanoparticle bypass immune system and prolonged the circulation time. By taking this advantage, we not only avoid overusing of PEG moiety but also creating new material that can give similar stealth property.

In addition, the measurement of the TNP and DOX-loaded TNP surface zeta potential revealed a net charge of -37.7±2 mV owing to the presence of negatively charged phosphate moiety on the surface. The similarity in zeta potential value of bare and drug loaded nanoparticles further confirmed the unchanged of surface property of TNP after DOX encapsulation. Taking into account that DOX is the cationic drug, if it is nonspecifically absorbed onto the surface of TNP, the surface charge property of this NPs could change, however, after DOX encapsulation, the surface charge of TNPs remains constant. This observation gives strong evident for the localization of DOX into the core of NPs.

Besides physicochemical properties, stability of nanoparticles is another essential parameter that needs to be carefully evaluated in order to translate to biological application stage. Therefore, we conducted stability tests in various *in vitro* physiological conditions including ionic and pooled protein milieu at 37ºC using phosphate buffer saline (PBS) and Fetal Bovine Serum (FBS), respectively. After 7 days of incubation in PBS (pH 7.4), there is no noticeable

nanoparticles aggregation was observed demonstrating by unchanged in DLS and PDI indexes **(Figure 2.3E)**. In addition, TNPs are found to be highly stable in its colloidal state when expose to serum environment as revealed by constant optical density at 560 nm (**Figure 2.3F**), whereas in the case of bare PLGA NPs, the absorption at 560 nm increase rapidly and reaches to plateau within 15 mins indicating rapid aggregation of PLGA NPs. These kinetic absorption experiments conducted at 560 nm is the measurement of aggregation when NPs aggregated with protein and precipitated to block transparency of the light from the medium.[71] These results implied that the TNPs exhibit robust stability which could enlarge therapeutic window by prolonging circulation time in bloodstream and enhancing chances of designed nanoparticles to target and accumulate at bone tumor site. This serum stability further supports our claim that the hydration layer around the NPs due to hydrophilic phosphate moiety is sufficient enough to act as a stealth layer of protection in a manner similar to that of PEGylated system.

Calcium binding affinity.

Since the surface of TNPs was decorated with bisphosphonate, we next investigated *in vitro* binding affinity of TNPs with hydroxyapatite (HAp) as a bone-model. Our expectation is that with increase in NP concentration treated with HAp, the more NPs bound to HAp. However, as the nanoparticle concentration increases, percentage nanoparticle bind to HAp decrease **(Figure 2.4A)**. This realized us to optimize the concentration of TNPs that need to be treated with HAp, and the results for optimized concentration is presented in **Figure 2.4A**. With the optimized concentration, we found that nearly 80% of NPs bind to HAp at concentration of 100 µg/mL, whereas only 20% of NPs were bound at the concentration of 800 µg/mL and 1000 µg/mL. Therefore, we selected minimum and maximum concentration (100 µg/mL and 1000 µg/mL, respectively) to elucidate kinetic binding property of TNPs toward HAp. Along with targeted NPs,

PEGylated NPs at the same concentrations was used as control sample. To our expectation, more than 80% TNPs bound to the surface of HAp within 15 mins of incubation time (**Figure 2.4B**). This trend plateaued on further increase of incubation time. In contrast, in the case of PEGylated NPs, just 20% of NPs bound to

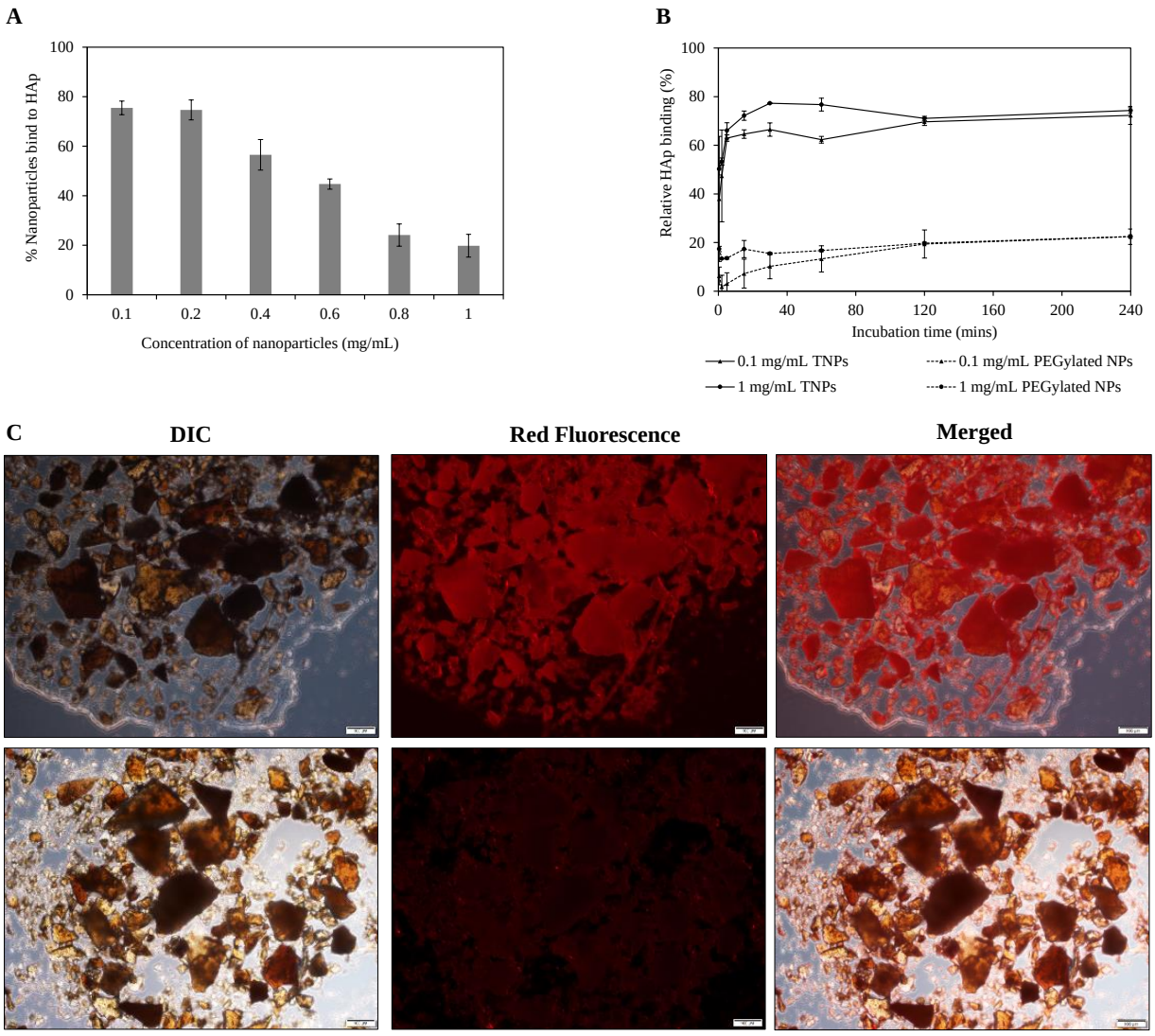

Figure 2.4 TNP's interaction with Hydroxyapatite (HAp). (A) Quantitative evaluation of HAp binding of NPs with varying concentration of TNPs. (B) Time dependent binding of TNPs with HAp. PEGylated NPs were used as control. (C) Representative fluorescence images of HAp crystal after incubation with RhB-labeled TNPs showing the interaction between HAp and targeted NPs. Values represent mean ± s.d., n = 3.

HAp after 2 hours of incubation, at this stage when bounded PEGylated NPs with HAp were centrifuged down and the supernatant was measured spectrophotometrically under fluorescence reader which shows sufficient amount of NPs. This non-specific binding of control NPs could be accounted for carboxylic functional groups presence on the surface of PEGylated NPs. The interaction between HAp and TNPs labelled with RhB was further confirmed by imaging of HAp crystal under fluorescent microscope where the presence of TNP highly enhanced fluorescent signal captured on the surface of incubated HAp crystals, while insignificant fluorescent signal were obtained on HAp samples incubated with PEGylated NPs (**Figure 2.4 C & D**, respectively).

Drug loading and release study.

TNP's drug loading capacity and drug release profile were also evaluated. **Figure 2.5A** shows the DOX encapsulation efficiency of TNPs at varying DOX concentrations. There was more than 7wt% of DOX was successfully encapsulated in 1mg/mL PLGA. Among these five different formulations, 100µg/mL initial input of DOX gave the most effective loading efficiency without changing nanoparticle physicochemical property. Thus, this formulation was chosen to use in further experiments.

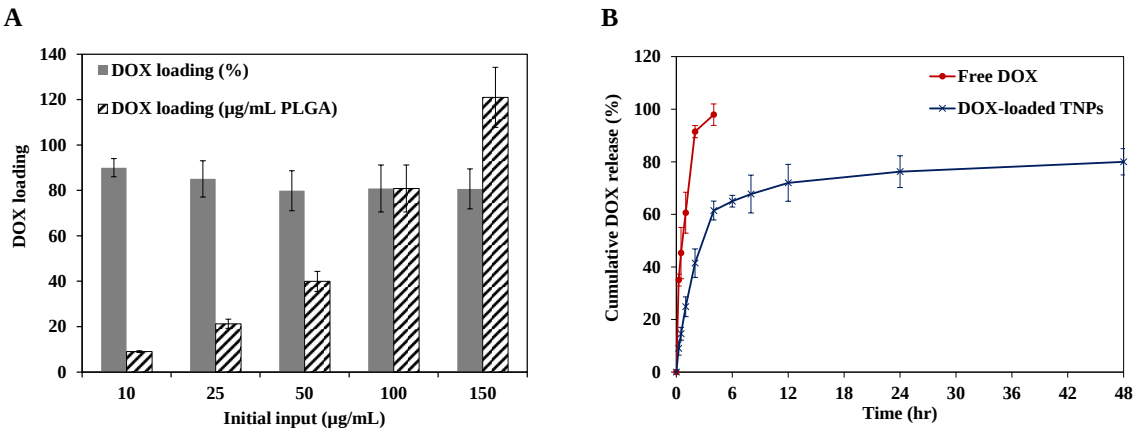

Figure 2.5 Drug loading and release study. (A) Dox loading efficiency and (B) *In vitro* doxorubicin release study at pH 7.4. Values represent mean ± s.d., n = 3.

With the optimized DOX loaded TNPs sample, the *in vitro* drug release was investigated at pH=7.4 in phosphate buffer saline (PBS). A cumulative drug release study was performed using 10kDa molecular cut-off dialysis bags. A control experiment was also performed using an aqueous solution of free DOX placed in the dialysis tubing. As can be seen in **Figure 2.5B**, in the case of free DOX, 100% drug was burst released within the period of 6h, whereas DOX loaded TNP shows the extension of drug release up to 24h. This result indicates that DOX loaded TNPs exhibit typical sustained drug release profile of nanomedicine over a 24h time period at 37°C (**Figure 2.5B**).

Cellular uptake study.

After understanding the drug loading efficiency of the TNPs, we next studied the cellular internalization to evident the targeting capability of TNPs in *in vitro* environment against mouse osteosarcoma K7M2 cells. The cellular internalization of TNPs was first visualized under confocal laser scanning microscope by incubating RhB-labeled TNPs with K7M2 cells for 3h. Confocal micrographs revealed that a large quantity of NPs internalized into the cell and localized around the periphery into the cellular compartment (**Figure 2.6A and B**) with some localized into the perinuclear region as evident from merged z-stack CLSM images (**Figure 2.6B**).

A quantitative cellular uptake of RhB-labeled TNPs was then conducted using flow cytometry in compare to conventional PEGylated NPs. Our results showed the cellular uptake of both TNPs and PEGylated NPs displayed time-dependent uptake (**Figure 2.6C**). As the nanoparticle incubation time increased, the enhancement of cellular uptake was observed in both TNPs and PEGylated group. However, at an equal incubation time, the TNPs were taken up by K7M2 cells is higher than that of PEGylated NPs (**Figure 2.6D**), suggesting that conjugation with

bisphosphonate plays a significant role in targeting nanoparticles to bone cancer cell in compare to PEGylated NPs.

As most cancer cells display aggressive profile in unselectively uptake of substances presence in their growing environment, it is important to set up a comparative experiment in order

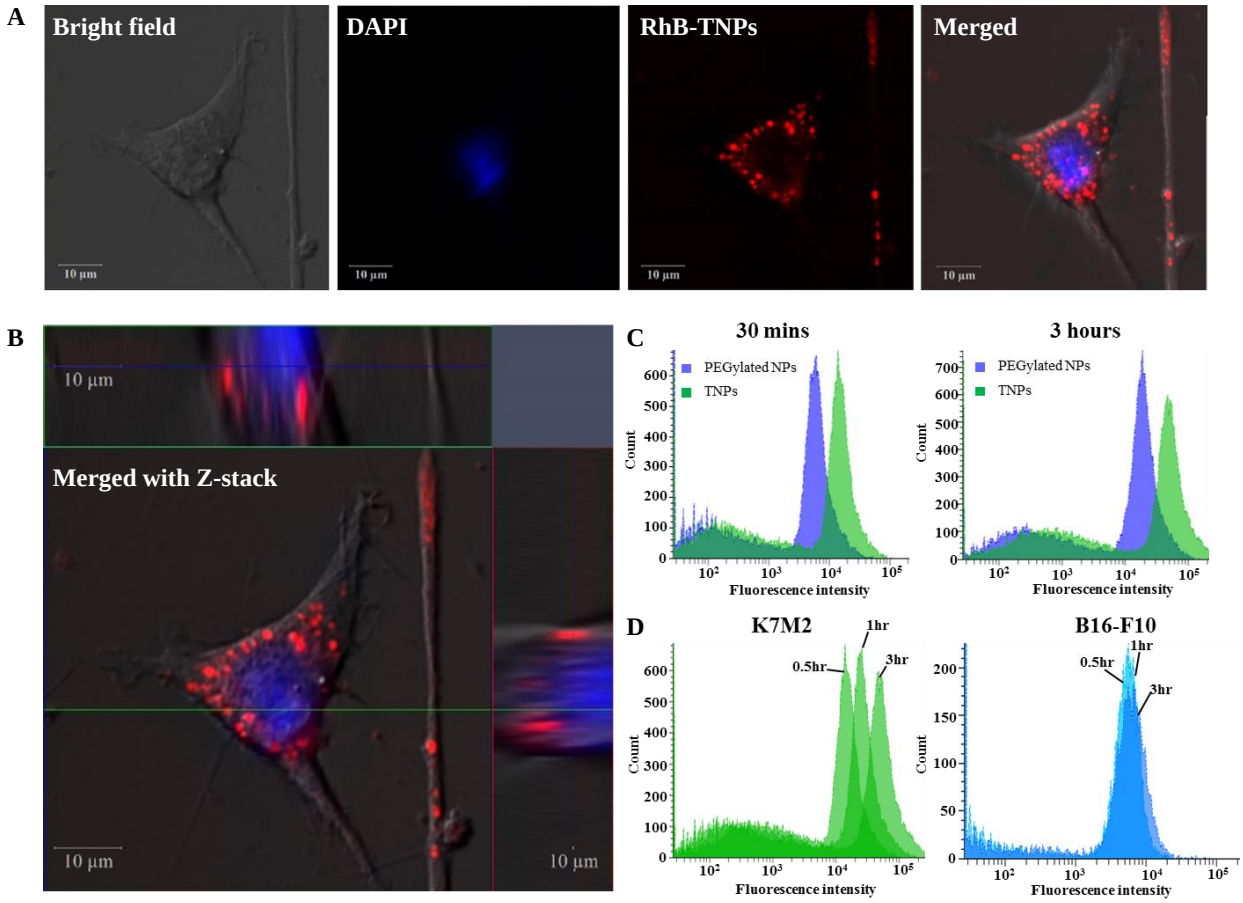

Figure 2.6 Cellular internalization study. (A) Confocal microscopic micrograph of Rhodamine labeled TNPs. (B) Z-stack of single K7M2 cell incubated with Rhodamine-labeled targeted nanoparticles showing intracellular distribution of particles throughout the cytoplasm and perinuclear regions. (C) Time dependent fluorescence-activated cell sorting (FACs) studies showing TNPs time dependent internalization pattern into the K7M2 cell. PEGylated NPs without ALE-Lipid were used as controlled NPs. (D) Selectivity of TNPs among 2 different aggressive cancerous cell lines (K7M2: left; B16-F10: right)

to assess specificity of targeting ligands among different cancerous cell types. With this in mind, we have chosen another aggressive non-targeted melanoma (B16-F10) cell line to rationally evaluate the distinctive property of TNPs under cellular environment. As a result, a dramatic increase in K7M2 cellular uptake was observed from 30 min to 3 hours of incubation as evidenced by an increase in fluorescence intensity. This time-dependent cellular uptake pattern was absence in the case B16-F10 melanoma cells where fluorescent intensity remains constant even after 3 hours of incubation. The high cellular uptake of targeted nanoparticle toward K7M2 cells was attributed to cell membrane specific interaction with phosphate moiety of Alendronic acid, in a typical endocytosis-mediated receptor uptake. This observation was in agreement with previous study conducted by T.-K. Ryu et. al., where Alendronic acid conjugated nanodiamond showed extensive accumulation in osteoblastic cells (MC3T3-E1) but not non-targeted HepG2 and NIH3T3 cell types.[73] Specifically, protein tyrosine phosphatases was investigated as one of the possible bisphosphonate binding receptor presence on the surface of osteoblastic cells.[74] Moreover, protein phosphatases were identified to be overexpressed in osteosarcoma in compared to that of normal osteoblast and osteoclast cells which would help targeting ligand to target cancerous cells efficiently.[75,76] Also, the same phenomenon was observed by Toledo et. al., where researchers were studied in the bone tumor of thirty osteosarcoma patients and found that protein tyrosine phosphatases is over expressed in osteosarcoma.[76] Osteosarcoma cells are of the osteoblastic lineage, which is characterized by cells secreting the osteoclast-inducing factor, receptor activator of nuclear factor-κB ligand. Receptor activator of nuclear factor-κB-Fc, osteoprotegerin, bisphosphonates, and Src inhibitor are shown as positive candidates and can control various aspects of osteoclast function.[77] From the results, it could be interpreted that phosphate moiety on

the surface of nanoconstruct can selectively facilitate the accumulation of the nanoparticles in the targeted cancerous cells.

Biocompatibility and cellular cytotoxicity study.

The biocompatibility of TNPs and *in vitro* cytotoxicity of DOX loaded TNPs were studied in K7M2 Osteosarcoma bone cancer cells using MTT assay. As can be seen in **Figure 2.7A**, at low TNPs concentration, no significant toxicity related to TNPs was observed indicating the excellent biocompatible of ALE-lipid at low concentration. However, when this concentration increases up to 150ug/mL, cell viability decreases to 80%, this reflection could be explained by masking of cellular surface under 96-well plate environment, hence reduce the cellular accessibility to oxygen and creating unfavorable growing environment to cell which further induce unexpected cell death.

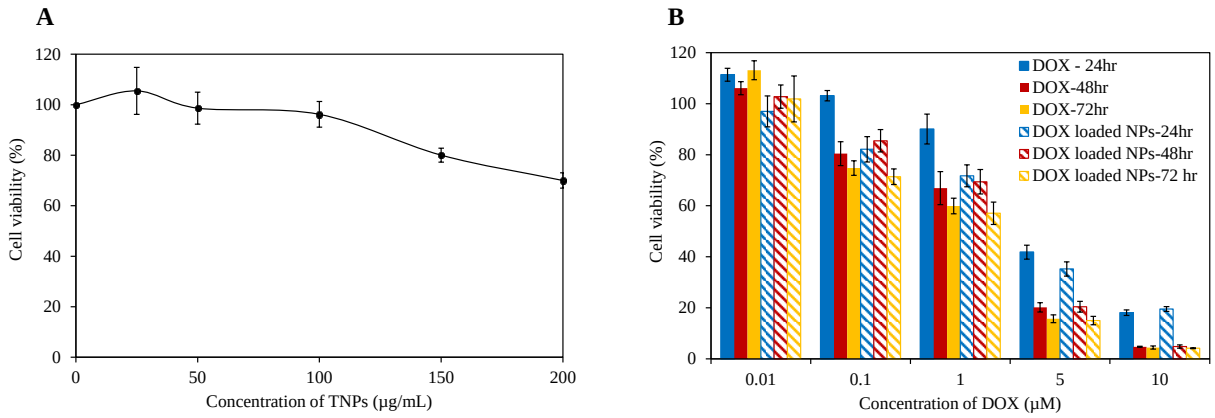

Figure 2.7 Cellular cytotoxicity studies. (A) Concentration dependent cytotoxicity of TNPs. (B) A comparative cytotoxicity studies of free Dox and Dox loaded TNPs against K7M2 Osteosarcoma. Values represent mean ± s.d., n = 6.

In a typical cellular cytotoxicity experiment of free DOX and DOX loaded TNPs, the results revealed that both agents exhibit a time- and dose-dependent cytotoxic effect **(Figure 2.7B)** in which at low incubation time (24hr) the drug loaded NPs showed higher cytotoxicity than free

DOX with the IC50 of 3.7 and 6.1µM, respectively (**Table 2.1**). This enhancement in cytotoxicity of DOX loaded TNPs in lower incubation time is likely due to nanoparticle's internalization mechanism. First, the exterior phosphate groups of targeted NPs were attracted by protein tyrosine phosphatases receptor present on the surface of osteosarcoma cells leading to the acceleration in accumulation and distribution throughout cell membrane. These targeted nanoparticles further internalized into the cell via endocytosis with core holding drug; thereby, intensely increase intracellular drug concentration and resulted in enhanced cytotoxicity. Whereas, in the case of free DOX, water soluble drug slowly diffuse into the cell limiting intracellular drug concentration. However, when cells were under treatment for longer period of time (48hr and 72hr), both free DOX and DOX loaded TNPs exert similar cytotoxicity effect. This further supports the evidence of rapid uptake of nanoparticulate system thereby increasing intracellular drug concentration as compare to that of free drug molecules.

Incubation time	**IC50 value (µM)**	
	Free DOX	**DOX loaded NPs**
24 hr	6.144	3.793
48 hr	2.621	3.064
72 hr	1.44	1.717

Table 2.1. IC50 of free DOX and DOX loaded TNPs on K7M2 cells.

2.4 Conclusion

Targeted therapy holds great potential for minimizing drug related non-specific toxicity. Towards this end, we have demonstrated the target specific delivery of DOX using nanoparticulate system consisting of densely packed alendronic acid corona that strongly binds with bone mineral, hydroxyapatite, aiming to target bone microenvironment. Engineered nano-system shows active

accumulation into the osteosarcoma cell exhibiting dose dependent toxicity similar to that of DOX in *in vitro* condition. However, in lower incubation time nanomedicine shows higher toxic effect than that of free DOX, which reveals that the nanomedicine deliver higher dose of DOX into the cells. Most importantly, higher ionic and serum stability of nanoparticle revealed that decorating nanoparticle surface with alendronic acid provides sufficient hydration layer and strong negative surface charge to sterically stabilized NP, which could be an alternative to PEGylated system to design nanocarrier. Overall, alendronic acid decorated proposed nano-system could provide a promising and most effective platform technology in the treatment of osteosarcoma.

Chapter 3 - Nano-confinement driven enhanced magnetic relaxivity of SPIONs for targeted tumor bioimaging

***Chapter 3**, in full, is a reprint of the material as it appears in Nanoscale, 2018, Tuyen Duong Thanh Nguyen, Arunkumar Pitchaimani, Colin Ferrel, Ravindra Thakkar, and Santosh Aryal. doi: [10.1039/C7NR07035G](10.1039/C7NR07035G)*

Abstract

Superparamagnetic iron oxide nanoparticles (SPIONs) are highly biocompatible and have documented versatile synthetic technique based on coprecipitation, reduction-precipitation, and hydrothermal methods where Fe^{3+} and Fe^{2+} ions react in aqueous solutions. Both of these ions are present in our body and have clear metabolic pathways, therefore, have attracted extensive research and development in the field of diagnostic imaging and therapy. However, most of the SPIONs based clinical diagnostic contrast agents were discontinued due to severe pain, lower transverse magnetic relaxivity ranges from 80-180 $mM^{-1}s^{-1}$, short-lived, and lack of disease specificity. Therefore, in this research, we put forth to engineer bone cancer targeted hybrid nanoconstruct (HNC) with a higher transverse magnetic relaxivity of 625 $mM^{-1}s^{-1}$, which is significantly higher than that of clinical contrast agents. Engineered HNC is peripherally decorated with a bone-seeking agent, alendronic acid conjugated phospholipid, exhibiting hydrodynamic size of 80 nm with negative surface potential, -35mV. The interior skeleton of the HNC is made up of biodegradable and biocompatible poly(l-lactic-co-glycolic acid) (PLGA) in which 5 nm SPIONs are confined. We have successfully tuned the distance between the confined SPIONs from 0.5 to 4 nm as revealed by transmission electron microscopy (TEM) micrographs and the magnetic resonance image (MRI) phantoms. Such cluster confinement dramatically enhances the magnetic relaxivity possibly due to the increase in net local magnetization due to the proximal field inhomogeneity. In an *in vitro* examination, 80% of HNC was found to bind with hydroxyapatite (HAp), which when imaged under TEM shows a painting of SPIONs over a HAp crystal. HNC was found to accumulate in mouse osteosarcoma tumor (K7M2 tumor model), both MRI and histological examination of tumor show the potential of HNC as targeting agents for diagnosis of tumor at the bone.

3.1 Introduction

Engineered magnetic nanoparticles, more specifically superparamagnetic iron oxide nanoparticles (SPIONs), have attracted extensive research and development in the field of diagnostic imaging and therapy.[78–81] Iron being one of the major mineral components of a biological system, whose biocompatibility is extensively investigated and better understood, becomes a preferred choice for various biomedical applications.[82–88] Among them, contrast-enhanced magnetic resonance imaging (ceMRI) is one which widely explored, as these contrast agents can create extremely large microscopic field gradients, which shorten longitudinal and transverse relaxation times (T_1 and T_2) of proton thereby producing "bright" and "dark" image contrast, respectively. SPIONs used as T_2 contrast agents primarily increase the rate of T_2 relaxation and create "dark" contrast effects, whereas paramagnetic metal ions such as Gd^{3+} used as T_1 contrast agents accelerate T_1 relaxation and produce the "bright" contrast in the image.

Highly studied paramagnetic ions in MRI are manganese (Mn), chromium (Cr), and gadolinium (Gd). These metallic ions are relatively toxic in free metal ion forms, therefore need to be encapsulated into the chelating agents.[17,89,90] In particular, Gd-based MR contrast agents, where Gd^{3+} is chelated into the macromolecular chelating agents such as Gd-BOPTA (gadobenate dimeglumine, Multihance®), GdDTPA (gadopentetate dimeglumine, Magnevist®), and Gd-EOB-DTPA (gadoxetic acid disodium, sold as Primovist® in Europe, Eovist® in the USA), are in clinics with the greatest value. However, development of nephrogenic systemic fibrosis (NSF) has been recognized in patients with severe renal impairment.[91–93] Reports have emerged regarding the accumulation of gadolinium in various tissues including bone, brain, and kidneys of patients who do not have renal impairment.[94–96] Due to this reason, the United States Food and Drug

Administration (FDA) published a safety announcement in July 2015 that it is investigating the risk of brain deposits associated with the repeated use of GBCAs MRI.[97]

On the other hand, SPIONs are highly biocompatible and have documented versatile synthetic technique based on coprecipitation, reduction-precipitation, and hydrothermal methods where Fe^{3+} and Fe^{2+} ions react in aqueous solutions.[98–100] Both of these ions are present in our body and have clear metabolic pathways such as degradation in lysosome due to an acidic environment, or eliminated via hepatobiliary excretion due to their uptake by the reticuloendothelial system (RES). Owing to its safe and clear excretion pathway, there is a huge interest in the development of SPIONs based contrast agent. Unfortunately, commercially available iron oxide MRI contrast agents, such as Feridex® produced by Berlex-USA, Endorem™ produced by Guerbet-France, and Resovist® produced by Bayer Schering Pharma AG-Germany, were discontinued from the manufacturers. These clinical agents consist of 4-6 nm SPIONs, which are susceptible to rapid renal clearance (renal filtration threshold size is ~6 nm), and transverse magnetic relaxivity ranges from 80-180 $mM^{-1}s^{-1}$ at 3T. Broad applications of these discontinued MRI agents were strictly limited due to rapid uptake by the RES cells viz.; Kupffer cells lining the hepatic sinusoids, as well as similar cells in the spleen, lymphnodes, and bone marrow but not in neoplasms.[87,88] Therefore, organ-specific cancer targeted SPIONs with high magnetic relaxivity is highly desirable in the clinic for the detection and monitoring therapeutic response against cancer.

Among the organs susceptible to cancer, bone is a favorable site for tumor growth and a predominant destination for the metastatic cancer cells to reside such as metastatic breast cancer. Despite intensive efforts in the development of therapeutic and diagnostic agents against cancer occurring at the bone, tumor localized in bone remains as an incurable fatal disease due to the fast clearance or the non-specific binding profile of the agents. Among different types of bone targeting

ligands, bisphosphonate (e.g. alendronic acid (ALE)) has been long emerging as a bone-seeking agent owing to its strong binding affinity with HAp, a major mineral component in bone environment.[101–104] However, there exists a knowledge gap regarding the unique design of the system that precisely targets to the bone and enhances the diagnostic effect. Herein, we uniquely engineered targeted HNC made up of PLGA and superficially decorated with covalently conjugated ALE whose inner polymeric core is loaded with 5 nm SPIONs in a controlled fashion by tuning the distance between the clustering SPIONs as demonstrated in **Figure 3.1**. Effect of such cluster confinement in the magnetic properties of HNC was studied in detail, and the possibilities of using proposed nanoconstruct as a MR contrast agent were also studied to picture the system as a bone tumor imaging contrast agent.

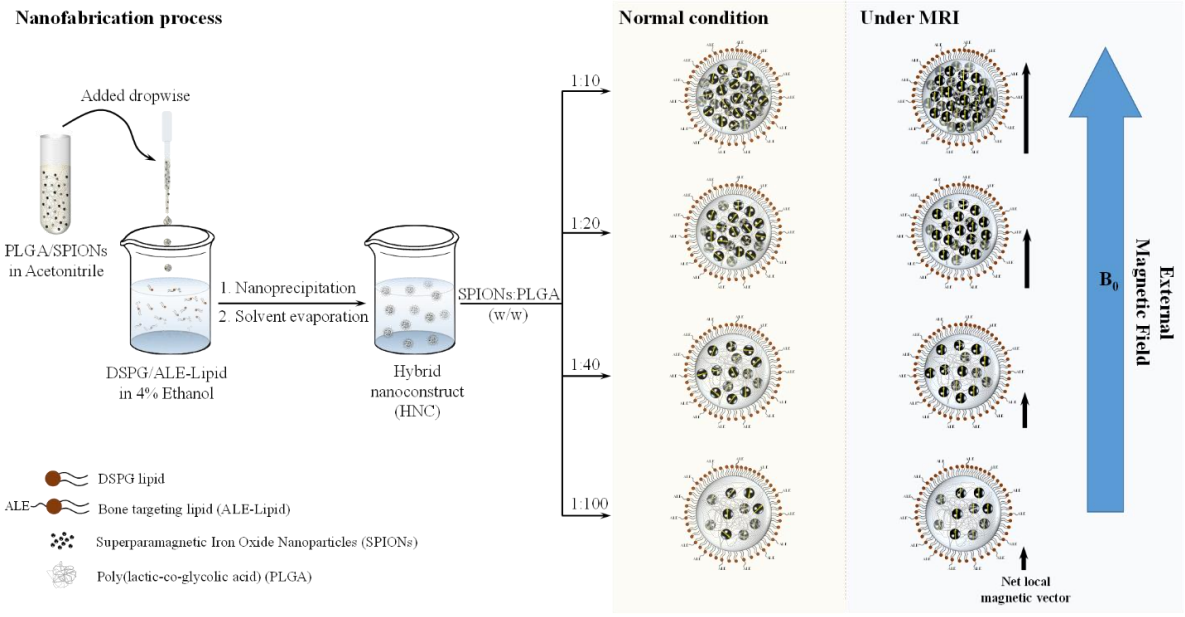

Figure 3.1 Schematic represents the preparation process of HNC using nanoprecipitation technique. The clustering degree of HNC is tunable by changing the ratio (w/w) of SPIONs and polymeric matrix PLGA in organic phase. In the designed experiment, the amount of PLGA was kept constant at 1 mg while the amount of SPIONs was varied at 10, 25, 50, and 100 µg correspond to SPIONs:PLGA (w/w) ratio of 1:100, 1:40, 1:20, and 1:10, respectively. As a consequent, the interparticle distant of SPIONs get reduced and confined within polymeric matrix. Such cluster confinement dramatically enhances the magnetic relaxivity which could be attributed to the increase in net local magnetization due to the proximal field inhomogeneity when the external magnetic field (Bo) is applied.

3.2 Materials and Methods

Chemicals and reagents

Alendronic acid was purchased from TCI America. 1,2-Dipalmitoyl-*sn-glycero*-3-phosphoethanolamine-*N*-(succinyl) (sodium salt) (16:0 Succinyl PE), 1,2-distearoyl-*sn-glycero*-3-phospho-(1′-*rac*-glycerol) (sodium salt), and L-α-phosphatidylethanolamine-*N*-(lissamine rhodamine B sulfonyl) (Ammonium Salt) (*egg*-transphosphatidylated, Chicken) (Egg Liss Rhod PE) were purchased from Avanti Polar Lipids Inc. (Alabaster, AL, USA). Iron oxide nanocrystals with an oleic acid coating (5 nm) were purchased from Ocean NanoTech (San Diego, CA, USA). 50 : 50 poly(D,L-lactide-*co*-glycolide) carboxylate end group (0.55–0.75 dL g^{-1}) was purchased from DURECT Corporation (Birmingham, AL, USA). Osteosarcoma cell line K7M2 was purchased from ATCC and maintained according to the manufacturer's recommendation. All other chemicals and solvents were purchased from Sigma-Aldrich (Milwaukee, WI, USA) and used as received.

Animal and tumor model

All animal experiments and protocols were performed in strict accordance with the NIH guidelines for the care and use of laboratory animals (NIH Publication No. 85-23 Rev. 1985) and approved by the Institutional Animal Care and Use Committee (IACUC) and Institutional Biosafety Committee (IBC), Kansas State University, Manhattan, Kansas. Six-week-old female NU/NU nude mice were purchased from Charles River Laboratories International, Inc. and used for the study after 7 days of adaptation. For mice bearing K7M2 tumor models, 1×10^6 K7M2 cells in 1× PBS were subcutaneously injected into the hind rear flank region of the mice. Tumor size and body weight were monitored periodically.

Synthesis of ALE–lipid conjugate

The reaction scheme for bone targeting ligand modified phospholipid is shown in supporting information **Figure A.1** and generally follows previously reported procedure using EDC/NHS coupling reaction.[105] To prepare head group modified phospholipid, 50 mg of Succinyl-PE lipid was hydrated in 6 mL deionized water at 60^0C until a clear viscous solution was obtained. After the mixture was cooled down, the lipid was activated by 67.2 mg EDC and 58 mg of NHS subsequently under a vigorous stirring condition at room temperature for 30 min. To this reaction mixture, 120 mg of ALE dissolved in 2 mL water containing 15% TEA was added and stirred for additional 24h at room temperature. At the end of reaction time, the reaction mixture was transferred into a cellulose dialysis bag (MWCO ~500 Da), and dialyzed against water for 24 h at room temperature; the water was freshly changed every 6h. The samples were lyophilized to obtain a dry powder and stored at -20°C for further use. The obtained product was 35 mg (90% yield). The formation of lipid bisphosphonate (ALE-Lipid) was confirmed by FT-IR and ^{1}HNMR.

Preparation of nanoparticles

Bone-targeted hybrid nanoconstruct (HNC) was prepared using one-step nanoprecipitation. Briefly, SPIONs were precoated with PLGA polymer by mixing 1 mg PLGA with different amounts of hydrophobic SPIONs (10, 25, 50, 100, and 150 μg) in chloroform and dried under vacuum. The iron oxide nanoparticles entrapped in the polymeric film was dissolved in 400 μL acetonitrile. The mixture was then added drop-wise to 3 mL of 4% ethanol containing 200 μg ALE–lipid conjugate and 260 μg DSPG under a magnetic stirring condition at 60 °C. At the end of the nanoprecipitation process, 1 mL of Mili-Q water was added to cool down the reaction mixture. The mixture was stirred continuously for an additional 1 h to facilitate the formation of nanoparticles and evaporation of the organic solvent at room temperature. The obtained

nanoparticles were further purified using an Amicon Ultra-4 centrifugal filter (Millipore, MA) with a molecular weight cut-off of 10 kDa and stored at 4 °C for further use. Nanoparticles labeled with RhB-lipid were prepared following a similar protocol with the introduction of 20 μg RhB-lipid in the lipid mixture prior to nanoparticle preparation. The controlled PEGylated nanoparticles were also prepared following a similar protocol using DSPE-PEG-COOH as an alternative to the ALE–lipid conjugate.

Characterization of HNC

The morphology of the prepared nanoparticle loaded SPION cluster was analyzed using a transmission electron microscope (TEM, Tecnai G2, Spirit Bio TWIN). TEM samples were prepared by drop casting and evaporation using formvar coated copper grid (400 mesh). TEM images were analyzed by a GATAN digital imaging system (GATAN, Inc.). The hydrodynamic size and zeta potential measurements of the prepared nanoconstructs were analyzed by dynamic light scattering (DLS) using a Zeta sizer Nano ZSP (Malvern, Worcestershire, UK). Brownian motion and the Smoluchowski equation were used to calculate the average hydrodynamic size and zeta potential value, respectively. The colloidal stability of HNCs was investigated in both ionic and serum conditions to mimic biological environment. In brief, 1 mg HNC was dispersed in PBS (pH 7.4) or 10% FBS. The change in size was recorded at a predetermined time using DLS. All data represent the average of triplicate measurements of samples prepared in different preparations. The amount of iron loaded into the HNC was determined using inductively coupled plasma mass spectrometry (ICP-MS, PerkinElmer, NEXion 350X). For ICP-MS, the HNC samples were digested with 2.0 ml of concentrated HNO_3 for 5 h. After chemical digestion, 100 μl of the sample was diluted with 10 ml of 2% HNO_3 and analyzed using ICP-MS.

***In vitro* bone targeting assay**

The binding affinity of HNCs to HAp was determined directly by measuring the amount of iron oxide nanoparticles present in HAp pellets and comparing it with the initial concentration of iron oxide nanoparticles by ICP-MS. Briefly, 100 μL of HNC (100 μg mL^{-1}) was incubated with 1 mL HAp (1 mg mL^{-1}) in 1 ml Eppendorf tubes for varying periods (0.5, 2, 5, 10, 15, 30, 60, and 120 min) at 37 °C. At the end of the incubation, the samples were centrifuged at 1500 rpm for 5 min to obtain HAp crystals and the HNC bound to them. Pellets were substantially washed 3 times with Milli-Q water, digested with 70% HNO_3, and quantified using ICP-MS.

***In vitro* magnetic properties**

The MRI relaxivity of HNC was performed using a 14.1 T MRI system (Bruker Avance III, WB, 600 MHz NMR-MRI). The transverse relaxation time (T_2) of different formulations of the HNCs (10, 25, 50 and 100 μg mL^{-1} initial input concentration) in Milli-Q water was determined using turbo spin echo sequence. T_2 relaxation was calculated using six measurements acquired with a constant repetition time (TR) of 1500 ms by varying echo time (TE) from 8 ms to 240 ms. The transverse relaxivity (r_2) was determined from the T_2 relaxation time and the concentration of iron (in mM). The corresponding T_2 weighted MRI phantoms were recorded using a turbo spin echo sequence with TR = 1500 ms, TE = 15 ms and slice thickness = 1 mm. The confinement effect of the SPION nanocluster in the polymeric core of nanoparticles was confirmed by evaluating the r_2 relaxation time of different SPION cluster compactness at the same iron concentration.

***In vitro* cellular uptake study**

To detect the presence of intracellular SPIONs, we performed cellular histology using the Prussian blue staining procedure. K7M2 mouse osteosarcoma cells were seeded onto poly-D-lysine coated glass coverslips at the density of 2×10^5 cells per coverslip and incubated for 24 h

for adherence. Then cells were treated with 100 μg mL^{-1} non-targeted or targeted NPs for 3 h at 37 °C. At the end of the incubation time, cells were washed twice in PBS, fixed with 4% paraformaldehyde for 30 min followed by Prussian blue staining (5% potassium ferrocyanide II in 5% hydrochloric acid (ratio 1 : 1)) for 1 h at 37 °C. Then, the cells were washed with PBS and subsequently counterstained with a 0.1% (w/v) nuclear fast red solution in distilled water for 1 min. After washing with distilled water, the images of the cell were obtained through an inverted microscope.

To further quantify the amount of HNC taken up by the cells, ICP-MS was adapted. In brief, cells were seeded in a 12-well plate with a density of 6.5×10^5 cell per well and incubated for 24 h. When cell confluency reached 80%, the cell medium was replaced with 1 mL of 10 μg mL^{-1} of HNCs or PEGylated NPs suspended in culture media and incubated for 3, 6 and 12 h. At the end of the predetermined time, the cells were washed 3 times with PBS, trypsinized, and collected by centrifugation at 5000 rpm for 10 min. Cellular uptake of HNCs and PEGylated NPs was further processed by sonicating with 2 mL HNO_3 at 70 °C for 60 min. The digested cell was diluted and subjected to ICP-MS for iron concentration analysis. Cells without HNC treatment was taken as the control.

Confocal study

Confocal laser scanning microscopy (CLSM) with *Z*-stack was used to confirm the intracellular distribution of HNCs. Non-treated cells and non-targeted SPION loaded PEGylated NPs were used as the control. In brief, cells were seeded in poly-D-lysine-coated 8 chamber slides at a density of 20 000 cells per well and incubated for 24 h. Then, the cells were treated with 50 μg mL^{-1} RhB-labeled NP suspension and incubated over varying periods (1, 2, and 3 h). After incubation, the treated cells were washed twice with 1× PBS (pH 7.4), fixed with 4%

paraformaldehyde for 30 min at room temperature, stained with DAPI for an additional 10 min and imaged using CLSM (Carl Ziess, LSM-700). The cellular uptake was accessed by measuring RhB fluorescence intensity using Image-J software (National Institute of Health).

Cellular cytotoxicity studies

The *in vitro* biocompatibility of HNCs was investigated on osteosarcoma K7M2 using MTT assay. In brief, 2×10^4 cells per well in DMEM were seeded in a 96-well plate and incubated for 24 h. To evaluate the biocompatibility of NPs, the media were replaced with different NP concentrations (10, 25, 50, 100, 150 and 200 μg mL^{-1}) and incubated for an additional 24, 48 and 72 h. Control cells were also maintained without any NP treatment (n = 6). After the completion of incubation, MTT was added to each well and further incubated for 3 h according to the manufacturer recommendation. The insoluble formazan crystals were solubilized using DMSO and the absorbance was recorded at 570 nm using a microplate reader (BioTek, Synergy H1 hybrid reader).

***Ex vivo* magnetic resonance imaging study**

A pilot MRI study was conducted in female Nu/Nu mice bearing subcutaneous mouse osteosarcoma (K7M2) tumors. When the tumor size reached around 40–80 mm^3, the animals were treated with HNCs or non-targeted SPION-loaded PEGylated NPs containing 0.25 mg of Fe per kg of body weight in 100 μL volume *via* the tail vein. Two hours post-injection, the animals were euthanized to simplify the MRI pilot experiment and immediately imaged using a Bruker WB 600 MHz NMR-MRI (14.1 tesla). The MR images were obtained using a QTR 30 mm coil at 25 °C with a FLASH (fast slow angle shot) protocol. The T_2 weighted images were taken with fat suppression parameters *viz.* TE/TR = 21/1500 ms, slice thickness = 1 mm, flip angle = 90°, image size 256 × 256, FOV = 30 × 30, and the total acquisition time = 16 min. The signal intensity of the

tumor area was further analyzed using Image-J software (National Institute of Health) to access signal distribution within the tumor region quantitatively.

Histological analysis

After imaging, the animals were euthanized and the tumors were dissected and fixed in formalin for histology analysis. The tumor samples were embedded in paraffin wax and sections were made of around 6 μm thickness. Further, the tissue sections were stained with H&E and Prussian blue to locate iron distribution in the tumor.

3.3 Results and Discussions

Design, synthesis, and characterization of targeted HNC

ALE is a member of bisphosphonate that has a high binding affinity toward bone cancer.[101] Structurally, ALE is a zwitterion compound functionalized with phosphate, primary amine, and tertiary hydroxyl that have rich electron density and capable of undergoing a coupling reaction with carboxylic acid. However, due to acidic functionality (pK_{a2} = 2.6, pK_{a3} = 6.73, pK_{a4} = 11.51, and pK_{a5} = 12.44), the reaction capability of primary amine of ALE was severely hindered.[106] Therefore, it is critical to use a certain kind of base (e.g., Triethylamine) to neutralize and further expose the lone pair electron presence on primary amine of ALE to drive the coupling reaction. Previously, we have established a protocol to attach ALE to the hydrophilic head of phospholipid using triethylamine as a base to deprotonate primary amine of ALE and increase the solubility of this compound in water.[105] A two-step coupling reaction was performed as outlined in **Figure A.1**. The obtained phospholipid conjugation was characterized by its proton environment to confirm the conjugation, as can be seen from the change in neighboring proton at δ 2.75 (m) and δ 3.29 (m), which corresponds to -CC$\underline{H}_2$C$\underline{H}_2$CH$_2$NHCO- and -CCH$_2$CH$_2$C$\underline{H}_2$NHCO-, respectively.

With the confirmation of the formation of ALE-Lipid conjugate, next, we synthesized HNC in which 5 nm SPIONs **(Figure A.2)** were embedded and confined into the core of the nanoconstruct. Nanoprecipitation of SPION and polymer mixture in lipid suspension resulted in spherical SPIONs clusters entrapped in a polymeric matrix and decorated peripherally with a bone targeting ligand (ALE-Lipid), as demonstrated in schematic representation (**Figure 3.1)**. HNCs exhibited unimodal size distribution with *Z*-average hydrodynamic diameter of 80±6 nm regardless to SPIONs number and density of confinement (**Table A.1**), while the average core size of the SPIONs clusters in HNC was 50 nm (**Figure 3.2 C**) as shown in transmission electron micrographs (TEM). This significant difference between hydrodynamic and TEM sizes indicates that ALE-Lipid provides significantly thick hydrating layer over the surface of the nanoparticle. Such dense hydrating layer could enhance the nanoparticle stability by minimizing steric attraction between nanoparticles, which also minimizes the protein corona formation in the blood stream and evade nanoconstruct from being recognized as a foreign material by the immune system.[105,107] Indeed, over a long period of incubation in ionic and serum condition, the size of HNC remained constant (**Figure 3.2D and Figure A.3**). The stability of nanoconstruct, being coated by bone targeted ALE-Lipid, would be advantageous not only for prolonging circulation time in biological condition and enhancing bone tumor targeting but also facilitating interaction with surrounding water for MRI contrast enhancement.

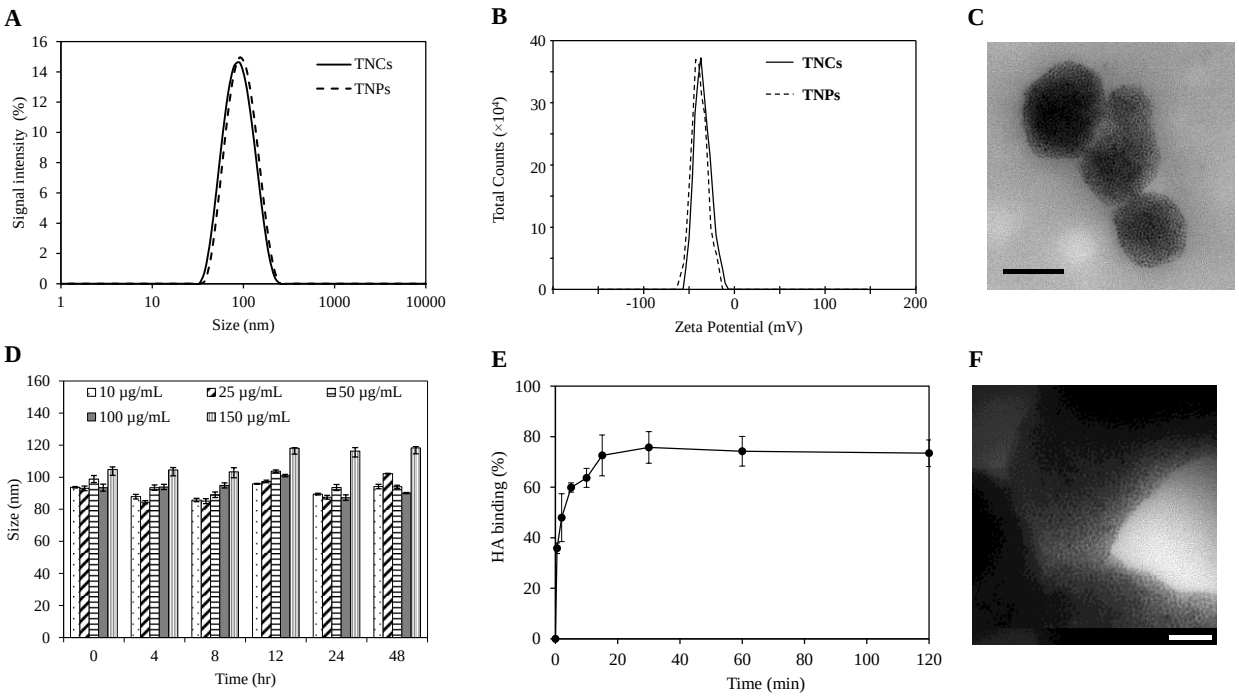

Figure 3.2 Physicochemical characterization of targeted HNC. (A) Hydrodynamic size distribution of nanoparticles with and without SPION loading. (B) Zeta potential showing consistent negative surface charge property of HNCs before and after loading of SPION nanocluster. (C) Representative transmission electron micrograph demonstrates SPION clustering in the core of the targeted nanoconstruct. (D) Stability of HNCs with different SPION loading in medium mimicking biological conditions (10% FBS in PBS). (E) Representative binding profile of HNCs with biomimetic bone hydroxyapatite (HAp) crystal. (F) TEM showing the interaction between HAp and HNC with abundance of SPION aggregates on the surface of HAp. Values are represented mean ± s.d., n = 3.

In bone microenvironment, the prevalence of osteosarcoma cells subsequently lead to the abnormal activity of osteoblast and osteoclast and consequently cause the release of bone mineral, predominantly in the form of calcium ion for tumor persistence.[108] Previous studies have shown that the released calcium ion at bone cancer sites can be selectively targeted by using Ale in the form of free molecule or nanoformulation.[109,110] Hence, by formulating nanoconstruct with the surface decorated with ALE to target the areas with high bone turnover could be advantageous for bone-targeted bioimaging. In this present study, HAp, a biomimetic bone mineral, was used for

preliminary evaluation of the *in vitro* binding affinity of targeted HNC toward the bone cancer. The binding affinity was measured by quantifying the amount of iron presence on HAp crystal using inductively coupled plasma-mass spectroscopy (ICP-MS). The result demonstrated a rapid binding kinetic in which more than 80% NPs bound to the surface of HAp within 10 mins of incubation (**Figure 3.2E**). Imaging of HAp crystal under TEM further confirmed the targeting ability of HNCs, which showed the presence of SPIONs (dark spot) on the surface of HAp (**Figure 3.2E**), note: as no staining agents were used, the polymer was not visualized under TEM.

Controlling SPION cluster density and tuning magnetic relaxivity

Clustering of SPIONs is an interesting phenomenon that governs the r_2 relaxivity of SPIONs.[111–114] In general, T_2 relaxation of water proton depends on the water diffusion rate, interaction time between water protons and local magnetic moment of nanocluster.[111,114–116] Therefore, to simplify and fully gain the understanding of the confinement effect, in this study, we controlled nanofabrication process in such a way that the obtained HNC exhibit consistency in size distribution regardless to SPIONs confinement (**Figure 3.1).** The overall hydrodynamic and TEM size distribution of HNC with different SPION loading were well-ordered by consistently following the same ratio between polymer and lipid suspension during the preparation process. Meanwhile, the SPIONs loading density was tuned by changing SPIONs feeding amount in polymer pre-coating step. As shown in **Figure 3.3A**, the degree of clustering increased when the feeding amount of SPIONs increased from 10 µg to 100µg per 1 mg PLGA. As a result, the inter SPIONs distance inside the polymer core got shorter and confined. Specifically, the average interparticle distance (distance between the confined SPIONs) inside the polymer core obtained from TEM images by measuring 100 HNC in each formulation indicated the average gap between two individual SPIONs was successfully tuned from 5, 3, 2, to 0.4 nm in accordance to initial

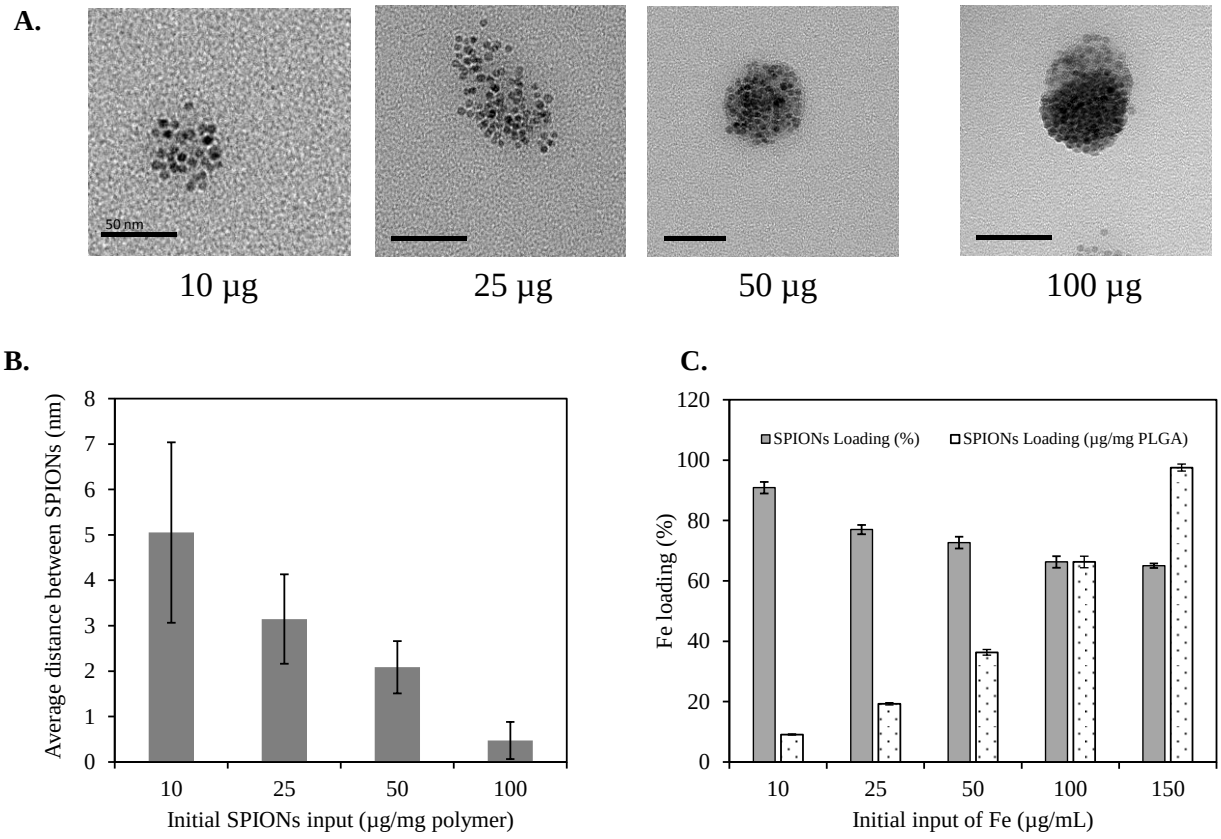

Figure 3.3 Controlling SPION cluster density. (A) TEM images showing tunable SPION packing density. (B) Average distance between two SPIONs in various packing nanoclusters (data obtained from 100 HNCs of each formulation using TEM images). (C) Iron loading efficiency measured by ICP-MS (n = 6).

feeding amount of 10, 25, 50, and 100 µg SPIONs, respectively (**Figure 3.3B**). The Fe loading efficiency in these formulations was assessed by ICP-MS, which gets plateaued at 100 µg/mL input with the maximum loading of 7% (w/w) SPIONs per 1 mg polymer (**Figure 3.3C**). When the feed amount of Fe increases up to 150ug per 1mg PLGA, the nanoconstruct started to aggregate due to the destabilization initiated by the excess amount of hydrophobic SPIONs in the suspension (**Figure A.3**). Therefore, we used the feeding amount of 10, 25, 50, and 100 µg SPIONs per 1 mg PLGA for further investigation.

To further investigate the effect of SPIONs confinement in MR-relaxivity, a serial dilution of each HNC samples corresponds to 0.4, 2, 3, and 5 nm interparticle distant was carried out to obtain constant Fe concentration. Resulting diluted samples were subjected to T_2 map measurement using a Bruker 600MHz (14.1T) Avance III with microimaging capability. The magnetic properties of HNCs were first investigated by measuring the signal intensity of water proton in the presence of different formulation with an echo time (TE) varying from 0 to 240 ms at constant repetition time of 1500 ms. Surprisingly, even though the Fe content in 4 different HNCs was kept constant at 0.4 mM, the signal intensity of water proton dramatically decreased (becomes dark) when interparticle distance decreased (**Figure 3.4A**). In comparing to 5 nm interparticle (SPIONs) confined clusters, the 0.4 nm exhibited 5.5 fold shorter T_2 relaxation time and ~40 times faster than pure water. To further investigate the dependence of MR relaxation rate on clustering density, we measured T_2 relaxation time of two more Fe concentration in HNC (0.1 and 0.2 mM) for each formulation (**Figure A.4**). T_2 relaxation time obtained from 0.1 and 0.2 mM concentration Fe was used to convert T_2 relaxation rate in s^{-1} (1/T2) and plotted against Fe content in mM concentration. The transverse relaxation rates exhibited a linear relationship with respect to iron concentration in bulk solution in all cases **(Figure 3.4B)** with the coefficient factor (R^2) greater than 0.98. In our measurements, the confined structure that had interparticle distant of 0.4 nm was measured to exhibit an r_2 of 641.2 $s^{-1}mM^{-1}$ [Fe], while the less dense confined nanoconstruct had r_2 of 335.3, 162.6, and 124.2 $s^{-1}mM^{-1}$ [Fe] in relation to interparticle distant of 2, 3, and 5 nm, respectively (**Figure 3.4B**). The results showed that a denser packing of SPIONs in HNCs could serve as an excellent T_2 contrast agent. This phenomenon was also depicted by T_2 -weighted images of different HNC samples with the equivalent amount of iron concentration as shown in **Figure 3.4C**, water was used as a control. Our results demonstrated that the sample that

has 0.4 nm interparticle distant always give darker contrast in comparison to that of other samples at the same iron concentration. Hence, MR relaxivity of designed nanoconfinement displayed the SPIONs density-dependent behavior, characterized by dramatically increasing the relaxivity with higher packing density.

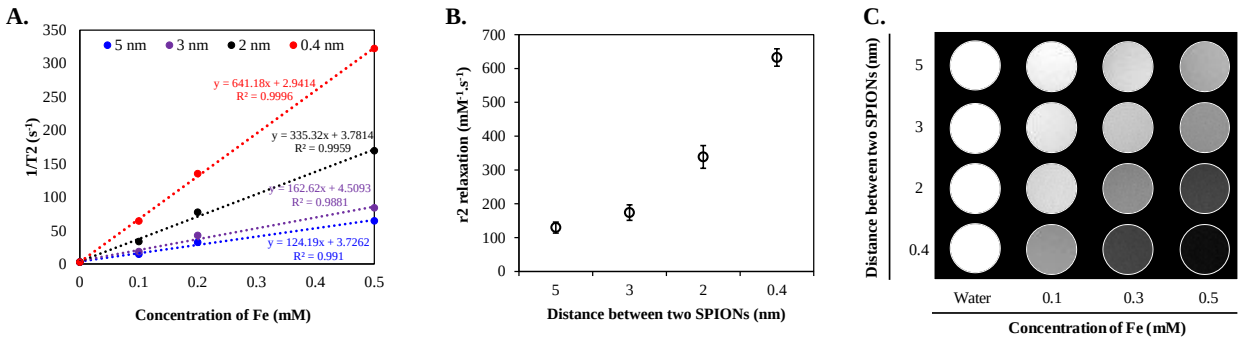

Figure 3.4 Confinement driven relaxivity enhancement. (A) Plot of $1/T_2$ *vs.* the concentration of iron in aqueous solution measured in a 14.1 T MRI system at 25 °C. (B) r_2 relaxation rate (s^{-1} mM^{-1}) with different SPION packing density. (C) T_2-Weighted MR images of HNC aqueous suspensions with different concentrations and packing densities. The T_2-weighted MRI phantoms were taken at TR = 1500 ms, TE = 15 ms, and slice thickness = 1 mm.

The relaxivity of Iron oxide nanocluster with a hydrophilic coating was governed by these following factors: net magnetic moment, interaction time between water protons and magnetic fields, and water diffusion rate. Of the different design consideration to rebuild the relaxivity of SPIONs, packing individual SPIONs into the cluster is one of the effective ways observed so far.[111–117] Clusters of different sizes are created by encapsulating SPIONs into the self-assembled amphiphilic polymers. This is the principle that an increase in the size of SPION increases its transverse relaxivity. The core of densely packed SPIONs generates high relaxivity due to the resulting high magnetic moment of the particles, and if the envelope is hydrophilic, it enhances the interaction with water proton thereby boosting the relaxivity up. An approach has been put forth by Paquet et. al., where authors encapsulated the cluster of SPIONs into the core of hydrogel,

which results in 2 to 3 times enhancement in the relaxivity.[114] It has also been reported that clinically used contrast agents, such as Resovist® or Endorsed®, when encapsulated into the liposome exhibit a high degree of particle aggregation and therefore high r_2 relaxivity, ranges from 150 to 200 $mM^{-1}s^{-1}$.[118,119] Similarly, Lin et. al. demonstrated the encapsulation of iron oxide nanoparticles into the chitosan matrix showing an 8-fold increase in magnetic relaxivity and assumed this is due to the effect of the cluster of iron oxide nanoparticle.[112] In an another study, an oil-in-water emulsion technique was used to encapsulate SPIONs into the Poly(isobutylene-*alt*-maleic anhydride) polymer to enhance the relaxivity and observed maximum r_2 of ~430 $mM^{-1}s^{-1}$.[120] A number of theoretical studies have illustrated that such enhancement in relaxivity is due to the fact that the decrease in the diffusion coefficient of water at the vicinity of the clustering particles increases the interaction time of water protons and the magnetic field generated by the particles. In efforts above, although the attention has been given in the enhancement in T_2 relaxivity of SPIONs, less attention has been given to the distance induced confinement of individual SPIONs and the influence of confinement in the T_2 relaxivity.

In the present study, densely packed SPIONs core generates a cooperative magnetic effect among each particle led to the increase in magnetic moment resulting in high relaxivity.[121] The ALE-Lipid with phosphate moiety on the outer layer traps water molecules via hydrogen bonding, creating bulk water protons environment surrounding magnetic fields near the SPIONs core which further increase the possibility of the interaction between water and magnetic particles. Similarly, the PLGA polymeric matrix also contributes in arresting water, which in turn slows down the water diffusion rate and as a consequence extending the interaction time of water proton and contrast agent, which is also observed in a similar system where chitosan was used as a polymeric matrix.[112] As a result, these three components together generate a synergistic effect of shortening the T_2

relaxation times, resulting in the relaxivity enhancement of the nanoconstruct. Therefore, by controllably confining SPIONs, the r_2 relaxivity of HNCs could be easily tuned and used as a technological platform for designing T_2 MRI contrast agent.

***In vitro* uptake of HNCs in osteosarcoma cells**

Before evaluating the cellular targeting capability of HNC, we first assessed the cellular biocompatibility of HNC *in vitro* by incubating HNC with K7M2 for 24, 48, and 72hr with a wide range of concentration from 10 to 200 µg/mL. As shown in **Figure 3.5A**, there was no dose-dependent cytotoxicity of HNC over a long period of incubation, suggesting biocompatibility of HNC in the cellular environment. To confirm the cellular interaction of HNC with K7M2, a cellular Prussian blue staining technique was adopted. By using this technique, the ferric iron present in the cell undergoes histochemical reaction with potassium ferrocyanide to form ferric ferricyanide exhibiting blue. For this experiment, cells were incubated with 100 µg/mL PEGylated SPIONs (control nanoparticle) or HNC (targeted nanoparticle) in culture media at 37°C for 3hr. **Figure 3.5B** showed a higher accumulation of iron in K7M2 cell treated with HNC as indicated by the blue staining of a large number of cells, whereas a few cells treated with control PEGylated SPIONs nanocluster showed accumulation. Although the Prussian blue staining technique can give an idea about the presence of iron in the cell, intracellular distribution of HNC is not clearly understood. Therefore, to study the cellular colocalization of HNC, we peripherally labeled HNC with red fluorescent dye (Rhodamine B) and investigated the intracellular distribution of HNC using confocal laser scanning microscope (CLSM). The CLSM technique is capable of providing continuous slices along the z-axis for acquiring an image of exterior and interior compartment of the cell body.[122] The representative middle slice of cell image was shown in **Figure 3.5C**, a blue channel for DAPI stained nuclei, and RhB labeled targeted HNCs in the red channel, which

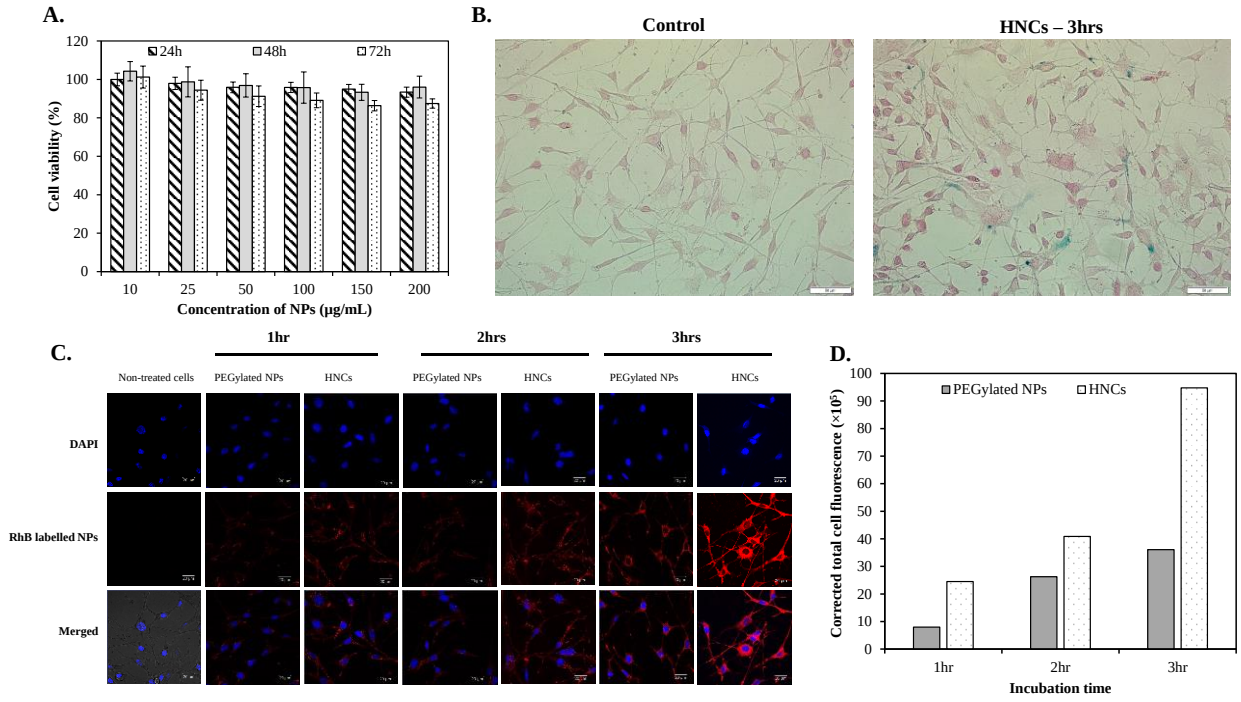

Figure 3.5 *In vitro* cellular studies. (A) Biocompatibility of HNCs. The result is represented as mean ± SD (n = 8). (B) Prussian blue cellular staining showing the presence of intracellular SPIONs. (C) Confocal images of K7M2 cells incubated with RhB labeled NPs over the period of incubation at 37 °C. The cell nuclei were stained by DAPI (blue). (D) A quantitative cellular NP uptake by measuring RhB fluorescence intensity in panel C using Image-J software.

indicated the relative distribution of HNC throughout cell body. A control experiment with non-targeted SPION loaded PEGylated NP was also carried out to evaluate the HNC. As shown in **Figure 3.5D**, it is clear that the cellular accumulation of HNC is the order of magnitude higher than that of non-targeted NP over the period of incubation. The quantitative evaluation of cellular internalization was also conducted by measure the RhB fluorescent intensity using Image-J software, which supported our hypothesis of targeting **(Figure 3.5D)**. In addition, the z-stack image of single cell presented in supporting information **Figure A.5**, further assured that these NPs are inside the cell body. The sequential slices taken horizontally from a stack of images indicated that targeted HNCs predominantly distributed in the cell, implying the targeting property

of targeted HNCs towards K7M2. This observation was further quantitatively supported by measuring cellular iron concentration using ICP-MS (**Figure A.6**). The results revealed that targeted HNC was associated with cell more efficient than that of control PEGylated HNC giving us strong evidence of targeting property of HNC.

***Ex vivo* imaging study and tumor histological analysis**

To further examine the tumor targeting ability of HNC for potential MRI application, we injected 100 µL of HNC (0.25 mg/kg of iron) into nu/nu mice bearing K7M2 tumor systematically via the tail vein. After 2-hour post-injection, the mouse was euthanized and immediately taken for T_2-weighted MR imaging acquisition. Since HNC showed significant enhancement in transverse relaxation, the dose of iron used in our experiment is lower than previously reported dose as well as the clinical dosage of Feridex® (0.56mg/kg).[123] Representative T_2-weighted MR images taken at TE/TR = 21/1500 ms along z-axis was shown in **Figure 3.6A**. As can be seen in **Figure 3.6A**, the significant reduction in MR signal (negative contrast) was observed not only around the periphery of the tumor but also from the different depth of tumor slice, and this signal dramatically reduced at the central of tumor region. The results indicated the effective accumulation and penetration of HNC into the deep tumor. On the other hand, there is less contrast enhancement was observed in the case of non-targeted SPION loaded PEGylated NPs (**Figure A.7A**). The darker contrast enhancement of HNC was further confirmed using ImageJ software to quantitatively access the signal intensity distribution throughout the tumor (**Figure A.7B**). Such significant enhanced contrast at depth MR signal localization behavior is probably caused by the selective accumulation of HNC driven by ALE that targets to the bone tumor lesion. The ALE can distinctively chelate with released Ca^{2+} ions at the tumor site thereby increasing the possibility of HNC accumulation in K7M2 cells as demonstrated in *in vitro* studies. To further verify the

presence of HNC accumulation in tumor, after imaging, the tumor tissue was subjected to histological analysis to study the distribution of SPIONs in the tumor. It is well known that Prussian blue dye has higher affinity with iron and can be used to detect the presence of iron in hard tissues. As expected the large number of blue-stained iron oxide NPs were observed in the histological slice of the tumor, augmenting the distribution data of NPs (**Figure 3.6B**). This further supports the accumulation potential of HNC in tumor tissues for tumor diagnosis.

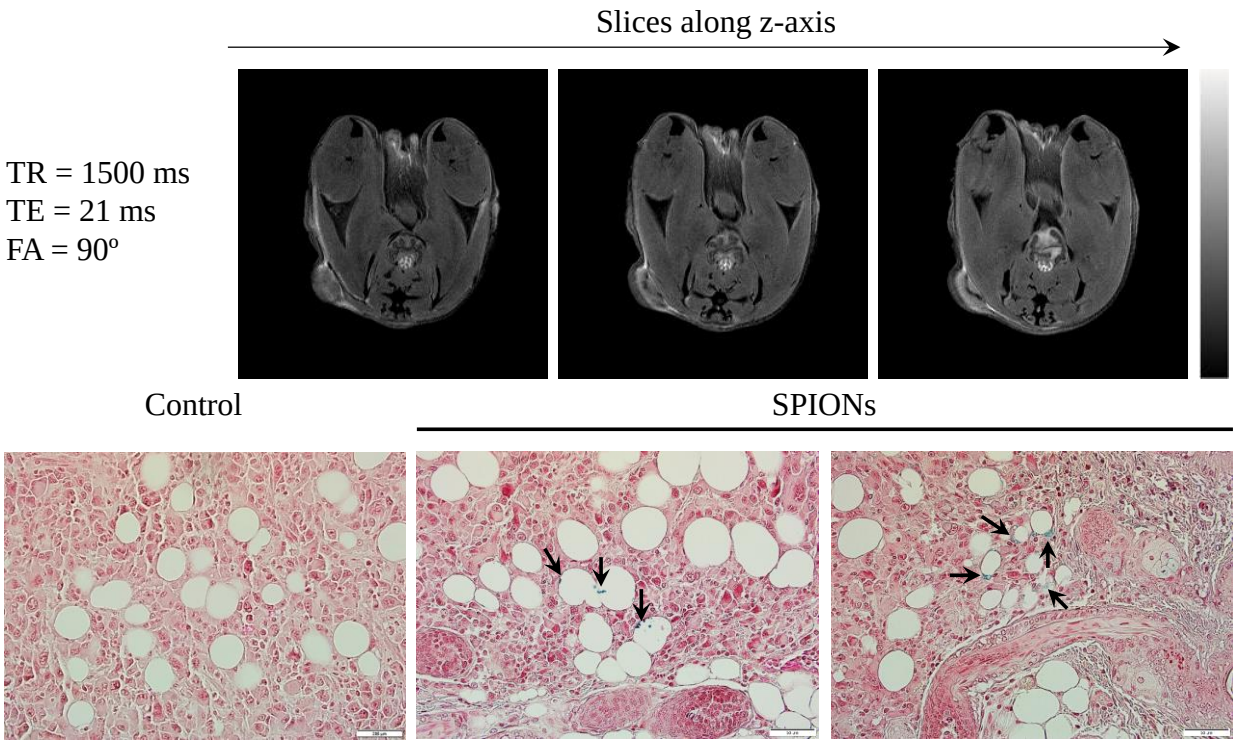

Figure 3.6 ***Ex vivo*** **study.** (A) MR images of a tumor bearing mouse at different *z*-planes with plane thickness of 1 mm, TE/TR = 21/1500 ms, flip angle = 90°. (B) Histology of tumor section of HNC treated animals stained with Prussian blue indicates the presence of SPIONs at the tumor site.

3.4 Conclusion

In summary, a targeted hybrid nanoconstruct was successfully engineered using a bone targeting ligand, ALE, and hydrophobic PLGA polymeric core. The core of the nanoconstruct was loaded with SPIONs in a controlled fashion by tuning the distance between the clustering SPIONs. The designed HNC was found to be of 80 ± 5 nm size and showed enhanced r_2 relaxivity from 124 to 641 mM^{-1} s^{-1} at 14.1 T, which is one order of magnitude higher than that of iron oxide-based clinically used magnetic contrast agents, such as Feridex® (r_2 = 120 mM^{-1} s^{-1}, 3 T) and Supravist® (r_2 = 57 mM^{-1} s^{-1}, 3 T). Moreover, the results from a binding study using HAp as a bone model revealed that HNC had strong binding affinity to the bone. In an *in vitro* cellular study against K7M2, HNC showed biocompatibility over a range of concentrations and exhibited higher cellular uptake than conventional PEGylated nanoparticles. Due to its higher targeting affinity and magnetic relaxivity, the MRI of the bone tumor-bearing mice showed an enhanced contrast capable of distinguishing the surrounding soft tissue. Therefore, the targeting and nanoconfinement strategy presented herein could be a promising design to enhance the contrast ability of SPION based contrast agents in the diagnosis and treatment of cancer.

Chapter 4 - Biomimetic Natural Killer Membrane Camouflaged Polymeric Nanoparticle for Targeted Bioimaging

***Chapter 4**, in full, is a reprint of the material as it appears in Advanced Functional Materials, 2019, Arunkumar Pitchaimani, Tuyen Duong Thanh Nguyen, Ramesh Marasini, Achini Eliyapura, Tahmineh Azizi, Majid Jaberi-Douraki, and Santosh Aryal. The dissertation author is equal co-first authors of this paper. doi: 10.1002/adfm.201806817*

Abstract

In the present study, a biomimetic nanoconstruct (BNc) with a multimodal imaging system is engineered using tumor homing Natural Killer cell membrane (NKM), near-infrared (NIR) fluorescent dye, and gadolinium (Gd) conjugate-based magnetic resonance imaging (MRI) contrast agent onto the surface of a polymeric nanoparticle. The engineered BNc is 110 ±20 nm in size and showed successful retention of NKM proteins. The magnetic properties of the BNc are found to be tunable from 2.1±0.17 to 5.3±0.5 $mM^{-1}s^{-1}$ under 14.1T, by adjusting the concentration of Gd-lipid conjugate onto the surface of the BNc. Confocal imaging and cell sorting analysis reveal a distinguishable cellular interaction of the BNc with MCF-7 cells in comparison to that of bare polymeric NP suggested the tumor homing properties of NKM camouflage system. The *in vitro* cellular interaction results are further confirmed by *in vivo* NIR fluorescent tumor imaging and *ex vivo* MR imaging, respectively. Pharmacokinetics and bio-distribution analysis of the BNc show longer circulation half-life (~9.5h) and higher tumor accumulation (10% of injected dose) in MCF-7 induced tumor-bearing immunodeficient NU/NU nude mice. Owing to the proven immunosurveillance potential of NK-cell in the field of immunotherapy, the BNc engineered herein would hold promises in the design consideration of nanomedicine engineering.

4.1 Introduction

The recent advent of biomimetic nanocarrier system shows tremendous progress in the field of nanomedicine.[69,70,124] Biomimetic nanoconstructs (BNcs) inspired by biologically occurred materials show promising biomedical applications, not only as a biocompatible methodology in nanotechnology, but also it mimics the function of natural biological materials.[125,126] This technology has already proven the advantages of transforming natural materials into functional materials ranging from drug delivery to bio-sensors, for example, application of nanomaterials in cancer theranostics.[127,128] The advantages of incorporating biological materials with synthetic materials include biocompatibility, resistivity, cellular interaction, enhanced circulation half-life, and cellular retention.[70,127,129] Among various biological materials, mammalian cell membranes such as blood pool materials like red blood cell membrane,[130] leukocyte membrane,[127] and platelet cell membrane[131] possess both targeting moieties, as well as immunomodulating markers, showing the potential application in cancer therapy. Among various blood pool agents, Natural Killer (NK) cell is a predominant member of the innate immune system.[132–134] The major function of NK cells includes host defense against microbial infections and tumor cells by immunosurveillance of cell surface abnormalities in major histocompatibility class I markers and cell stress markers.[132,135,136] Recently, we have shown the inclusion of NKM in the liposome for water-soluble drug delivery.[137] The result shows a promising therapeutic effect in human tumor xenografts in a mouse model.

NK cells comprise about 5-20% of total peripheral blood mononuclear cell count and are also found in tissues like liver, placenta, and peritoneal cavity. NK cells can lyse cancer cells by the mechanism of interplay between its activating inhibitory signals without prior sensitization.[132] Currently, NK cells and their products are in Phase I clinical trials for immunotherapy. [138,139] Among various engineered NK cell lines, clinical grade NK-92 shows promising results in

immunotherapy, as it lacks inhibitory markers of NK cells along with ease of *in vitro* expansion. [140–142] NK-92 cells are stable IL-2 dependent NK cells characterized by the presence of activated receptors such as NKG-2D, NKp30, NKp44, etc.

Other than therapeutics, various bioimaging contrast agents are also encapsulated/conjugated with the synthetic nanoparticles (NP) aiming to prolong circulation half-life and enhance tumor accumulation.[14] Among different bioimaging modalities, MRI has advantages with excellent spatial resolution and soft-tissue contrast for diagnosis and monitoring the therapeutic response.[143] The most predominantly used MR contrast agent belongs to the Gd-based contrast agents (GBCA) (25-30%). The GBCA include Gd-BOPTA (gadobenate dimeglumine, Multihance®), GdDTPA (gadopentetate dimeglumine, Magnevist®), Gd-EOB-DTPA (gadoxetic acid disodium, Eovist®), MS325® (gadofosveset trisodium, Ablavar®), etc. Despite advances in cancer bioimaging, early detection and targeted bioimaging using MRI are highly challenging in most tumor types. [144–146] This is due to the lack of targeting moiety, short resident time and free distribution to the extracellular spaces upon injection.

In the present study, we designed tumor targeting biomimetic nanoconstruct made up of the NKM camouflaged onto the surface of carboxylate terminated polylactic-co-glycolic acid (PLGA) NP. To this BNc, phospholipid conjugated GBCA and NIR dye was incorporated and studied their feasibilities under MRI and further supported by NIR fluorescent imaging **(Figure 4.1)**. The NKM was isolated from the NK-92 cells and hybridized with imaging components and PLGA NP using membrane extrusion technique. This technique gives us the opportunity to tune magnetic relaxivity by varying the Gadolinium- (Gd) lipid concentration onto the BNc. Considering the acquired properties of NK cell, we hypothesized that the engineered BNc would have an ability to function as NK cell, which could help in maximizing the delivery of payloads,

herein contrast agents, into the tumor by co-working with blood pool agents, hence enhancing the diagnostic efficiency in targeted cancer bioimaging.

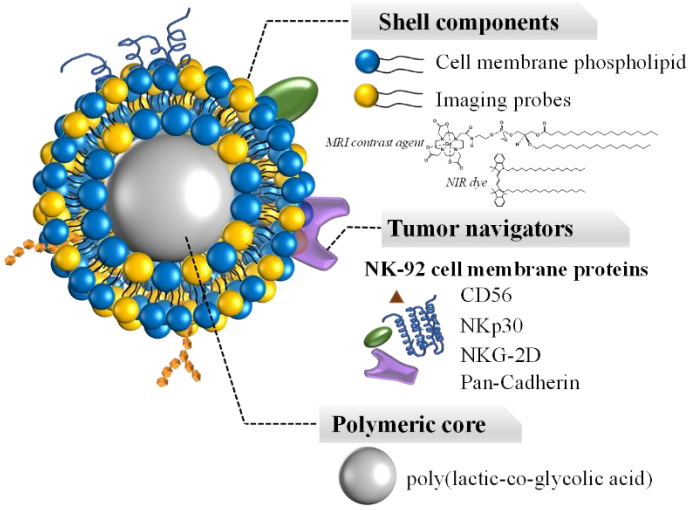

Figure 4.1 Design of Biomimetic nanoconstructs comprised of three distinct components including contrast agents, tumor navigators protein derived from cell membrane and polymeric core.

4.2 Materials and Methods

Materials

Poly (D,L-lactide-co-glycolide) carboxylate end group (50:50 dL/g) was purchased from DURECT Corporation (USA). L-α-Phosphatidylethanolamine-N-(lissamine rhodamine B sulfonyl) (Ammonium Salt) and (Egg-Transphosphatidylated, Chicken) (Egg Liss Rhod-PE) were purchased from Avanti Polar Lipid Inc. (USA). Gd (III) acetate was purchased from Alfa Aesar (USA). Primary antibodies for NKG2-D, NKp30 and Pan-cadherin were procured from Santa Cruz Biotechnology. NCAM (CD56) and secondary HRP-linked anti-mouse IgG antibody were purchased from Cell Signaling. Fluorophore-conjugated antibodies like FITC Mouse anti-Human CD56 and κ Isotype Control were purchased from BD Bioscience. All other reagents and chemicals used were of analytical grade.

Cell lines and tumor models

Human NK cells, NK-92, were procured from ATCC, Manassas, USA. NK-92 cells were grown and regularly passaged in Alpha Minimum Essential Medium (α-MEM) without ribonucleosides and deoxyribonucleosides and supplemented with 1.5 g/L sodium bicarbonate, 2mM L-glutamine, 0.1mM 2-mercaptoethanol, 0.02mM folic acid, 0.2mM inositol, 200U/mL recombinant IL-2, 12.5% (v/v) horse serum and 12.5% (v/v) fetal bovine serum. The human breast cancer cells, MCF-7, were procured from ATCC (USA). The cells were grown and maintained in Dulbecco's Modified Eagle's Medium (DMEM) supplemented with 10% (v/v) fetal bovine serum (FBS), penicillin/streptomycin (100µg/mL) and maintained at 37°C in 5% CO_2 environment.

For tumor studies, six-week-old female immunodeficient NU/NU nude mice were procured from Charles River Laboratories International, Inc. (USA). All animal experiments and protocols were approved by the Institutional Animal Care and Use Committee (IACUC) and Institutional Biosafety Committee (IBC), Kansas State University, Manhattan. For solid tumor models, 1×10^6 MCF-7 cells in saline were implanted sub-cutaneously into the hind rear flank region of the mice and the tumor growth were monitored periodically.

Isolation of NK cell membrane

Isolation of NKM were performed using sucrose gradient ultracentrifugation method as reported.[137] In brief, nearly ~2×10^8 NK cells, NK-92, grown in multiple T-75 culture flask were harvested and washed twice with 1x PBS. Further, the washed cell pellet was suspended in homogenization buffer (10mM Tris-HCl, 1mM $MgCl_2$, 1mM KCl, 2mM PMSF, 25mM Sucrose, 200µg/mL Trypsin-chymotrypsin Inhibitor, 10µg/mL DNase and 10µg/mL RNase) and homogenized in ice for 5 min (20s pulse and 30s in between pulses). The homogenized suspension was pooled over the discontinuous sucrose gradient (55%, 40% and 30% (w/v) sucrose in 0.85%

saline) in polycarbonate tubes and ultracentrifuged in a Beckman SW 27 rotor at 28,000g for 30min at 4°C. The NKM fraction at 30% to 40% interface was collected in a clean tube and analyzed for its protein characterization using the dot-blot technique. For purification, collected membrane fractions were diluted with twice the volume of normal saline and ultra-centrifuged in a Beckman SW 27 rotor at 28,000g for 1h at 4°C. The purified membranes were lyophilized, weighed, quantified for its protein content using Bradford Assay and stored at 4°C for further use.

Preparation of Biomimetic Nanoconstruct

BNc were prepared using the simple nanoprecipitation method.[70,71,81] In brief, 1mg of PLGA dispersed in acetonitrile was added drop-wise to different concentrations of Gd-lipid (50-400µg) dispersed in 2ml of 4% ethanol under magnetic stirring at 60°C. After 15 min, 1mL of Milli-Q water was added to cool down the suspension and further stirred at room temperature. After 1h of stirring, the clear nanoparticle suspension (PLGA core) was extruded in the presence of isolated NKM (100µg dispersed in PBS) using 100nm pore-size Millipore membrane filter, concentrated in Amicon centrifugal filter (10kDa), and stored at 4°C for further use. For DiR/Rhodamine labeling, 10 µg of the dye dispersed in chloroform was dissolved in the PLGA dispersion and followed the same protocol of the preparation of BNc.

Characterization of BNc

The hydrodynamic size and zeta potential of the prepared BNc were characterized using Dynamic light scattering analysis (Malvern, Nano ZSP). The size and the shape of the prepared BNc were confirmed using transmission electron microscope (FEI Technai G2 Spirit BioTWIN). Further, the concentration of Gd^{3+} in BNc were determined using an inductively coupled plasma mass spectrometry (ICP-MS, NEXion 350X, Perkin Elmer). The concentration of proteins in all samples was determined using Bradford Assay following manufacture's recommendation.

Protein Characterization of BNc

For SDS-PAGE (Sodium Dodecyl Sulphate-Polyacrylamide Gel Electrophoresis), all samples were prepared with the overall protein concentration of 50µg/wells loaded in a 4-20% Mini-PROTEAN® TGX Protein Gels and stained with Coomassie brilliant blue. For western blot, protein samples were transferred to the PVDF membrane and treated with primary antibodies for CD-56 (Cell Signaling), NKG2-D (Santa Cruz), NKp30 (Santa Cruz) and Pan-cadherin (Santa Cruz) along with HRP-conjugated anti-mouse IgG secondary antibody (Cell Signaling). The blotted films were further developed using SignalFire™ ECL Reagent (Cell signaling) and imaged chemiluminescent signals Bio-imager (Kodak).

Stability of BNc

The physiological stability of the prepared BNc at 4°C in PBS (pH=7) was investigated using dynamic light scattering size analysis. In brief, 50µg/mL of BNc samples in PBS were incubated at 4°C for two weeks and investigated their change in size by measuring the samples in DLS every day. The serum stability of the prepared BNc was carried out as reported earlier.[147] In brief, 100µL of 500µg/mL of BNc were mixed with 100µL of 90% FBS at 37°C and record their change in absorbance with incubation time kinetically by recording at every 3sec over a period of 3h using Microplate reader (BioTek, Synergy H1 Hybrid reader).

Gd^{3+} release study

The cumulative Gd^{3+} release characteristics of BNc under the physiological condition at 37°C was determined as reported periodically. In brief, 50µg/mL of BNc was placed in a 500 Da dialysis membrane bag and dialyzed against 250mL of PBS (pH=7.4) and acetate buffer (pH=5.2). At constant agitation (70rpm), 200µL of the buffer samples were collected at predetermined time

intervals (0-72h) and replace with an equivalent volume of fresh PBS buffer. The amount of Gd release from the BNc is determined using ICP-MS as reported before.

In vitro magnetic properties of BNc

The MRI relaxivity of Gd-loaded BNc was determined as reported previously.[17,148] The longitudinal relaxation (LR) time of BNc in the presence and the absence of NKM in an equivalent Gd^{3+} concentration (10 µg/mL) was determined using a RARE (Rapid Acquisition with Relaxation Enhancement) pulse sequence with variable repetition time on a 14.1T NMR system (Bruker Avance III, 600 MHz NMR-MRI). Concentration-dependent recovery curve of BNc was also investigated using a different concentration of BNc (0.05-0.4mM). The LR was determined from the T_1 relaxation time and the concentration of Gd^{3+}. The corresponding T_1-weighted magnetic resonance phantom images were also recorded using a turbo spin echo sequence (TR=1500 ms, TE= 6.50 ms, and slice thickness= 1mm).

Cellular uptake and biocompatibility studies

The cellular uptake efficiency of BNc in the presence and the absence of the NKM coating were investigated using FACS analysis (BD FACSCalibur™). In brief, 3 X 10^6 MCF-7 cells were grown in T25-flask and treated with 50µg/mL of Rhodamine-labelled BNc dispersed in DMEM media. After 6h of incubation, cells were trypsinized, washed and analyzed in FACS for the quantitative determination of NP uptake by MCF-7 cells. For the confocal study, Rh-labelled BNc were treated in an 8-chambered micro-chamber slide seeded with the cell density of 50,000 cells/well and incubated for 3h. After incubation, cells were washed, fixed, and immunostained with FITC-anti-CD 56. Nuclei of the cells were stained with DAPI, and the slides were observed directly in a Confocal Laser Scanning Microscope (Carl Zeiss, LSM-700). Further, the biocompatible nature of the BNc was investigated in MCF-7 cells using the [3-(4,5-

Dimethylthiazol-2-yl)-2,5-Diphenyltetrazolium Bromide] (MTT) Assay.[149] In brief, MCF-7 cells were seeded in a 96-well plate at the density of 10,000cells/well and incubated for 24h. After confluence, cells were treated with different concentration of BNc (10-150µg/mL) and incubated for additional 24h. After incubation, the medium was removed, 10µL of MTT (5mg/mL) dye were added and incubated further for 3h in the dark at 37°C. After 3h incubation, the formazan crystals were dissolved using DMSO, and the plates were read for absorbance at 590nm using Microplate reader (BioTek, Synergy H1 Hybrid reader).

***In vitro* cytokine release assay**

The immunogenicity of the prepared BNc along with the bare PLGA NP was tested for its immunoregulatory potential using standard cytokine release assay.[127,137] In brief, 8×10^5 THP-1 cells were seeded in a 12-well plate and treated with bare PLGA NP (100µg/mL), NKM (100µg/mL), Gd-lipid (100µg/mL) and BNc (100µg/mL) at 37°C for 24h. After 24h incubation, cell culture supernatants were collected, centrifuged, removed cell debris and stored at -20°C as small aliquots. For cytokine assay, samples were thawed and analyzed for pro-inflammatory cytokines, IL-1β (LOD:1.7 pg/ml), IL-6 (LOD:1.5 pg/mL), and TNF-α (LOD:1 pg/mL) using Magnetic Human Cytokine Multiplex Assays Kit (R&D Systems, Inc. Minneapolis, MN) in Luminex MagPix® instrument (Millipore Inc.,) as per the manufacturer recommendations. For positive control, cells were dosed with 3µg/mL of lipopolysaccharide for 24h.

Pharmacokinetics and Bio-distribution of BNc

The circulation half-life and pharmacokinetic profile of the BNc were investigated using Six-week-old female NU/NU nude mice (n=3). In brief, BNc (5mg/kg) were administered intravenously via tail vein injection, and the blood samples were collected at predetermined time intervals (0.5-48h) through tail vein puncture. The amount of BNc in the blood samples was

quantified using ICP-MS as described earlier. For the bio-distribution study, 5mg/kg of BNc were injected (i.v.) into the MCF-7 tumor-bearing mice, and after 24h of study, animals were sacrificed to collect major organs and tumor tissues. The tissue samples were weighed, digested using 2 mL of aqua regia (3:1 ratio of HCl:HNO_3), diluted in 2% HNO_3 and analyzed for the Gd concentration in ICP-MS as described earlier. Pharmacokinetic parameters were analyzed by a two-compartmental model using the MATLAB software (MathWorks, 2017b).[150–152]

Mathematical model

Pharmacokinetic models are employed to illustrate the process of nanodrug distribution in the whole body. When we follow a particular nanodrug administered with a specific route, we may study the whole body as a kinetically single unit, conventionally termed as compartment, which is homogeneous. For this purpose, we assume that the administered drug distributes uniformly in the body and that the drug equilibrates between different tissue/organ in a time-dependent fashion. However, we cannot conclude that the concentration of drug is the same in tissue or plasma. The bicompartmental model divides body into two different units or compartments. This division helps us study each tissue and its interaction with its relative components. In bicompartmental model, we assume that the administered drug enters the first compartment and then transported into the second compartment, tissue or organ.[153]The remaining drug will come back to the compartment 1 and then we have elimination of drug from first compartment.

In this study, we assumed that disposition of drug from blood to tissue follows a bicompartmental model (scheme 1). For the bicompartmental model, we assume that we have a first order transfer rate between two compartments, k_{23} and k_{32}, and we consider a first order elimination rate from the second compartment, k_{el}, without any elimination or metabolism in the

tissue. The schematic diagram for this case is outlined in the following diagram (Please see supporting information for details).

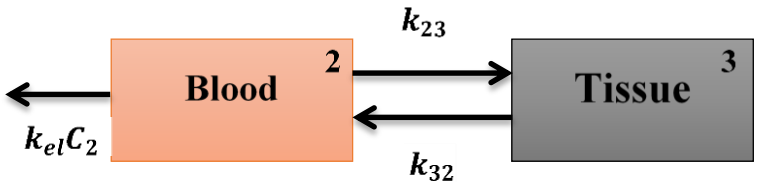

Figure 4.2 Model diagram for two compartments.

***In vivo* bio-imaging**

For *in vivo* bio-imaging studies, near-infrared fluorescent dye 1,1'-Dioctadecyl-3,3,3',3'-Tetramethylindotricarbocyanine Iodide (DiR) labeled BNc (10mg/kg) were injected intravenously into the MCF-7 tumor-bearing mice along with bare control PLGA NP and analyzed its bioaccumulation and tumor targeting efficiency using Pearl® Trilogy Small animal imaging system (LI-COR®). The fluorescent images at the near-infra-red window were taken at pre-determined time intervals (0, 3, 6, 12 and 24h) and the images were analyzed in Image Studio® software. At the end point, mice were euthanized, and excised organs were imaged and analyzed for the quantitative determination of BNc accumulation.

***Ex vivo* MRI imaging**

A pilot *ex vivo* MRI study was performed using NU/NU mice bearing MCF-7 tumors on a 14.1T NMR system (Bruker Avance III, 600 MHz NMR-MRI, 14.1T). In brief, NU/NU mice were intravenously injected with BNc (equivalent Gd concentration of 0.008 mmol/kg), and the animals were sacrificed after 2h post-injection. Within 15min of the sacrifice time, animals were imaged in MRI. The T1-weighted MR images were recorded using a QTR 30 mm coil with a FLASH (Fast, slow angle shot) protocol at 37ºC. The axial MR imaging parameters were TR = 1500ms,

TE = 6.5ms, flip angle = 90, image size 256x256, FOV=30x30 and slice thickness = 0.5mm. Further, the *ex vivo* MRI images were analyzed using DICOM software (Santesoft Ltd). All animal experiments and protocols were approved by the Institutional Animal Care and Use Committee and Institutional Biosafety Committee, Kansas State University, Manhattan.

Statistical Analysis All experimental data represent the mean ± standard deviation. Depending on the experiment parameters One-way and Two-way ANOVA were used for the statistical analysis. ***P<0.001, **P<0.01, *P<0.05 were considered statistically significant.

4.3 Results and Discussion

BNcs were fabricated using membrane extrusion method in the manner similar to that of liposomal fabrication.[69–71] The process involves the preparation of PLGA NP, extraction and isolation of NKM, and the cloaking of PLGA NP with isolated NKM, GBCA, and NIR dye. The biocompatible polymeric NP, PLGA, was prepared using the simple nano-precipitation following our earlier reports.[70,71] Further, the NKM was isolated and extracted from the NK-92 cells through sucrose gradient centrifugation.[137] The extracted NKM was lyophilized and re-dispersed in PBS.The amount of NKM yield was quantified by measuring the protein concentration. From ~2 x 10^8 NK-92 cells, the NKM yield was found to be ~300µg protein equivalent. Finally, the BNc were fabricated by extruding PLGA NP and Gd-lipid with isolated NKM [with the weight ratio of (5:1:1)] through 200nm pore sized polycarbonate membrane. For NIR dye labeling, constant 1.0 wt% of dye with respect to the 1 mg of PLGA was used in all cases. Gd3+ conjugated phospholipid (Gd-lipid) was synthesized via simple convenient coupling chemistry as described in earlier reports.[17,148,154] **Figure 4.3A** illustrated the schematic representation of the process of BNc fabrication. The hydrodynamic size of the bare PLGA NP was found to be 109±2.8nm, whereas the BNc were found to be in the range of 110±20nm, respectively (**Figure 4.3B**). The

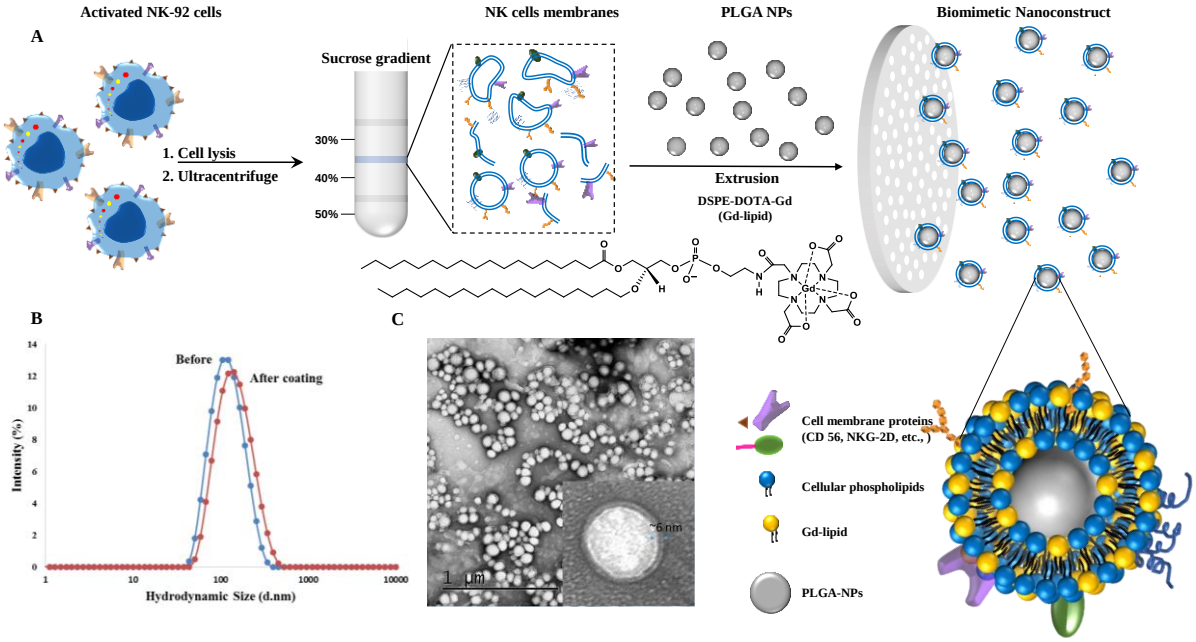

Figure 4.3 BNc physicochemical properties. (A) Schematic illustration of the preparation of biomimetic nanoconstructs made up of natural killer cell membrane isolated using sucrose gradient differential centrifugation. BNc were prepared using simple extrusion technique, where PLGA nanoparticles and Gd-lipids were extruded with isolated NKM. (B) DLS size of the BNc before and after NKM coating. (C) Transmission electron microscopic image of the prepared BNc, inset shows the magnified image of the BNc with distinct biomolecular corona (NKM and Gd-lipid).

transmission electron microscopic images of the BNc show clear coating materials onto the surface of the PLGA NP (**Figure 4.3C**). Further, to investigate its fabrication efficiency, three different formulations of BNc were fabricated as represented in **Table 4.1** as follows: BNc-A = (1000µg PLGA) : (200µg Gd-lipid) : (20µg NKM) ; BNc-B = (1000µg PLGA) : (200µg Gd-lipid) : (100µg NKM); BNc C = (1000µg PLGA) : (200µg Gd-lipid) : (200µg NKM). The hydrodynamic sizes of the BNc A, B, and C were found to be 111±2.1nm, 128±1.6nm, and 134±4.4nm, respectively.

Table 4.1 Physicochemical characteristics of BNc.

	Hydrodynamic Size (d.nm)	PDI	Zeta Potential (mV)
BNc A (5:1:0.1)*	111 ± 2.1	0.16 ± 0.02	-20.7 ± 0.76
BNc B (5:1:0.5) *	128 ± 1.6	0.19 ± 0.01	-36.9 ± 4.07
BNc C (5:1:1) *	134 ± 4.4	0.28 ± 0.04	-41.1 ± 0.59
Bare PLGA Nps (5:1) *	109 ± 2.8	0.14 ±.0.01	-20.1 ± 0.82
NKM	NA	NA	-26 ± 0.21

*** Ratios indicate in BNc corresponds to PLGA:GD-lipid: NKM protein ratio (by weight)**

[NA] sample not measured.

The results from hydrodynamic size indicated that the size of the BNc slightly increases with the increase in the concentration of NKM, which is presumably due to the presence of a larger amount of NKM that becomes hydrated in an aqueous environment. Further, the zeta potentials of the BNc A, B, and C were found to be -20±0.76mV, -36.9±4.07 and -41.1±0.59, respectively. The zeta potentials of the isolated NKM and bare PLGA NP were found to be -26±0.21mV and -20.1±0.82mV, respectively. This proves the evidence that the coating of NKM changes its zeta potential value more negative among different formulations, which is attributed to the negative zeta potential of the cell membrane that was organized onto the negatively charged PLGA NP. Based on physicochemical characteristics, more stable BNc-C (5:1:1) were chosen for further characterization studies. Hereafter, BNc represents BNc-C.

Next, we identified signature proteins in the BNc using SDS-PAGE and western blot analysis. **Figure 4.4A** and **B** represent the SDS-PAGE and western blot of the isolated NKM along with the engineered BNc. SDS-PAGE analysis revealed that the proteins from the NKM were successfully

retained in the BNc. Among the proteins, the characteristic signature proteins such as CD56, NKG-2D, and NKp30 were identified from the western blot analysis along with the control pan-cadherin (**Figure 4.4B**). NKG-2D and NKp30 are activating receptors found on the NK-cells for effective cytolytic functions on the tumor cell, which overexpress their ligands.[155] NK cells recognize tumor cells and stressed cells through these ligands. Thus, the presence of these signature proteins would facilitate the tumor targeting, thereby delivering maximum contrast agents to help distinguish tissue contrast.

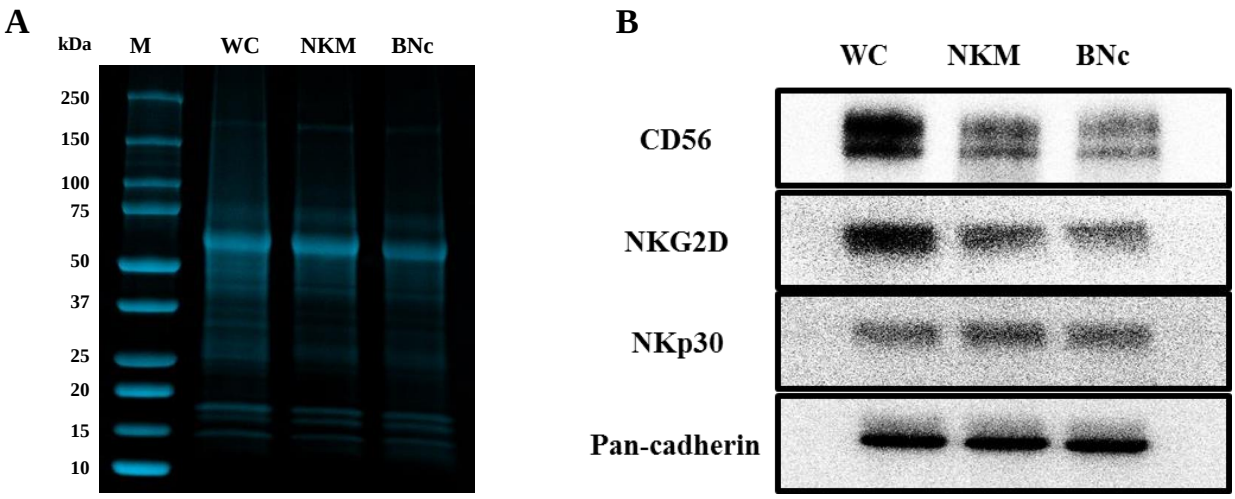

Figure 4.4 Protein characterization of BNc. (A) SDS-PAGE analysis of protein bands in NK-92 cell extract, isolated NKM, and the BNc. (B) Western blot analysis of BNc for its characteristic protein, CD 56, NKG-2D, and NKp30.

The stability of BNc in *in vivo* serum/plasma conditions was investigated by storing the BNc in PBS at 4°C and measuring the variation in hydrodynamic size for 14 days. **Figure 4.5A** shows the stability of BNc after 14 days in PBS. No significant change in its size was observed over 14 days of study. Further, the serum stability of the BNc was investigated by incubating the BNc with 90% FBS, **Figure 4.5B**. Compared to bare PLGA NP, BNc show higher stability in serum conditions as evident from the no change in its optical density over the period at 560nm. This optical measurement records the change in absorbance due to particle aggregation.[71,137]

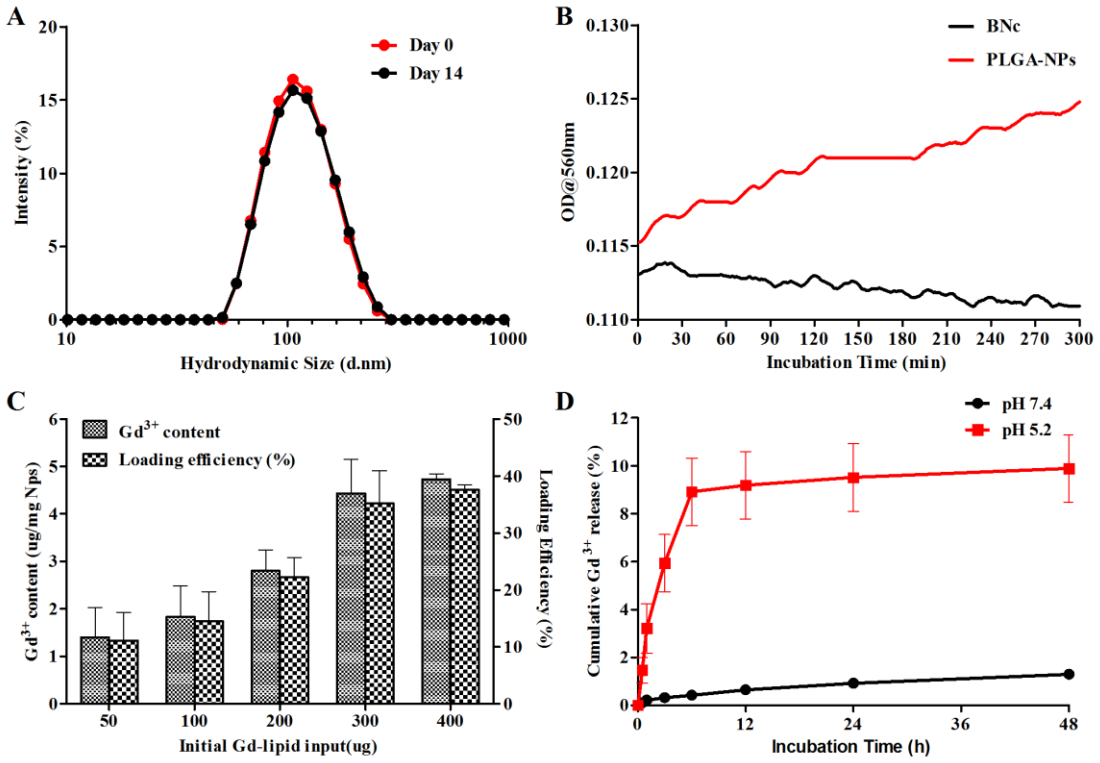

Figure 4.5 Stability and gadolinium loading/release characteristics of BNc. A) Stability of BNc in PBS (pH = 7.4) at 4 °C. B) Serum stability of BNc and bare PLGA-NP in 90% FBS at 37 °C. C) Gd3+ loading efficiency of BNc with different initial input concentrations of Gd-lipid (50–400 µg). D) Gd3+ release characteristics of BNc in PBS (pH = 7.4) and in acetate buffer (pH = 5.2) at 37°C.

The Gd^{3+} loading in BNc was further investigated in detail by increasing the concentration of Gd-lipid input during BNc fabrication. With the fixed concentration of PLGA and NKM (5:1), the concentration of Gd-lipid was varied between 50 and 400µg/mg of PLGA (**Figure 4.5C**). The maximum Gd loading efficiency of BNc was found to be ~19%, and the Gd loading content was found to be 4.5±0.1µg/mg of PLGA. However, we observed that the higher loading of Gd^{3+} results in instability of BNc in physiological pH. For further studies, BNc with the Gd^{3+} content of 3±0.4µg with the loading efficiency of 11% was used for all other experiments (BNc). Further, the Gd^{3+} release characteristics of BNc were investigated at pH=7.4 in PBS as well as at pH=5 in

acetate buffer in order to map the Gd^{3+} stability in BNc which is directly related to toxicity. We further assumed that by stabilizing Gd^{3+} in BNc, Gd^{3+} associated toxicity would be reduced as its ionic form is toxic. A cumulative Gd^{3+} release from the BNc was performed by dialyzing the samples using 500Da dialysis bag, which gives easy passage to release free Gd^{3+} (Mw 157.25 Da) to the dialysis reservoir. The cumulative release percentage of Gd^{3+} from BNc at pH=5 and 7.4 and 5.2 was found to be around 2% and 10% after 48h (**Figure 4.5D**). This further confirms the stability of Gd^{3+} in the fabricated BNc**.**

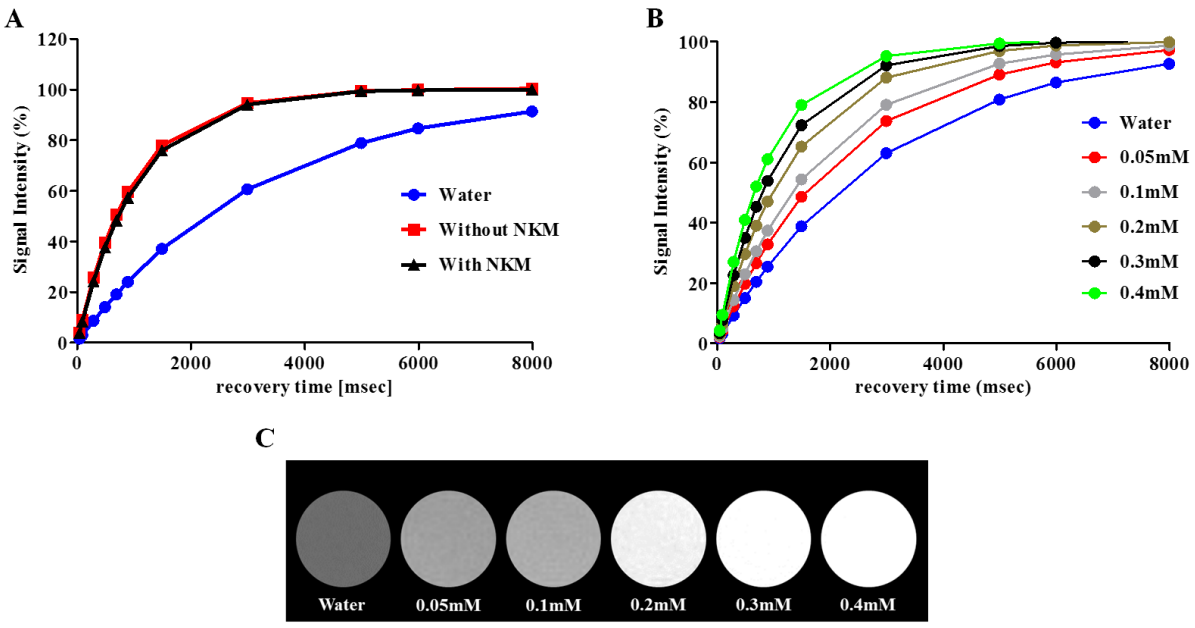

Figure 4.6 Magnetic properties of BNc. A) T1 recovery curve of BNc in the presence and the absence of NKM, showing r1 = 5.0 mm−1 s−1. B,C) T1 contrast phantoms of different concentration of BNc (0.05–0.4 × 10−3 m) with corresponding recovery curve acquired at 14.1 T.

Figure 4.6 shows the magnetic resonance properties of BNc dispersed in water. The r_1 relaxivity of the BNc in the presence and the absence of NKM was found to be 4.8±0.6 $mM^{-1}s^{-1}$ and 5.0±0.5 $mM^{-1}s^{-1}$, respectively. We did not observe significant differences in the r_1 relaxivity, which further assures us that the distribution of Gd-lipid in the BNc is not affected by the NKM

coating. This is in agreement with the earlier report where authors discussed alternation in r_1 relaxivity due to the distance induced confinement of Gd^{3+}.[145,156] In the present case, if NMK has inserted in between Gd-lipids instead of surface coating, this would increase the distance between Gd-lipids, and we should experience a significant change in relaxivity. **Figure 4.6B** shows the MR phantom images of different concentration of BNc acquired at 14.1T. The phantom images showed brighter contrast as the concentration increased to 0.4mM, this was further confirmed by corresponding T_1 curve (**Figure 4.6C**).

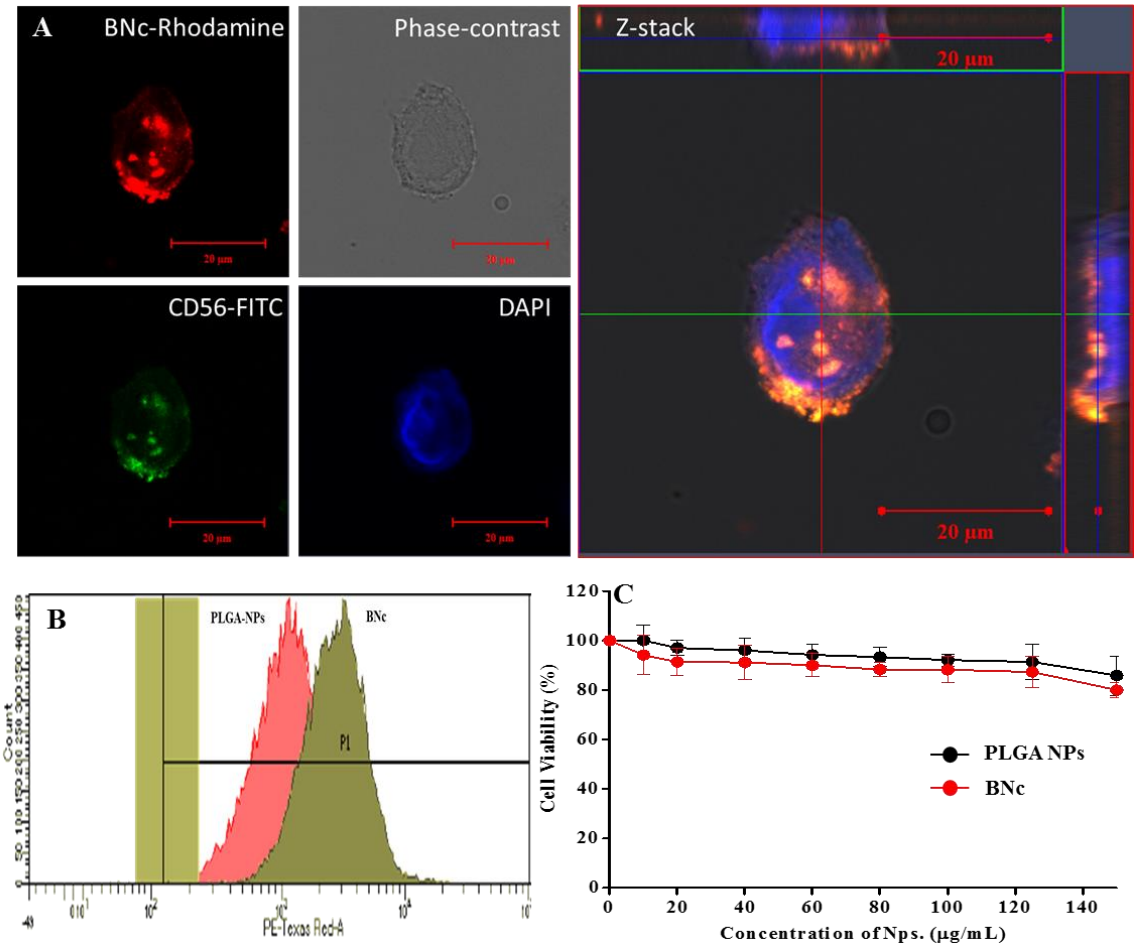

Figure 4.7 *In vitro* cellular studies. (A) Confocal laser scanning micrograph of cellular uptake of BNc in MCF-7 cells after 3 h of incubation, immunostained with FITC-anti-CD 56. (B) FACS analysis of quantitative cellular uptake of BNc in comparison with bare PLGA-NP after 6 h incubation. (C) Biocompatibility of different concentration of BNc (10–150 µg) in MCF-7 cells after 24 h incubation.

The cellular uptake and intracellular distribution of the Rhodamine labeled BNc were investigated in MCF-7 cells using confocal laser scanning microscope and flow cytometry (**Figure 4.7**). MCF-7 cells treated with BNc show rapid uptake of the BNc within 3h of incubation. The uptaken BNc were found intact in the cells as evident from the bioaccumulation of immunostained FITC-anti-CD56 and Rhodamine signals inside the cells (**Figure B.1**). The nuclei of the cells were further stained with DAPI, and this shows BNc were distributed in perinuclear regions. Z-stack images of MCF-7 show clear evidence of intracellular distribution of BNc (**Figure 4.7A**). Further, the selective targeting of the BNc in MCF-7 cells was compared with the bare PLGA NP labeled with Rhodamine dye. Flow cytometry analysis was conducted to assess the cellular uptake efficiency. The results indicate that cellular uptake of BNc was more predominant than the bare PLGA NP illustrating the targeting potential of BNc towards cancer cells (**Figure 4.7B**). The biocompatibility of the BNc and bare PLGA NP was investigated in MCF-7 cells through MTT assay. 24h incubation results show that even at higher concentration (150µg/mL) BNc were not cytotoxic (**Figure 4.7C**). This clearly demonstrated the biocompatible nature of BNc, which can be used for bioimaging applications *in vivo*.

Further, the immunogenicity of the NKM derived BNc was investigated in human peripheral blood monocytes, THP-1, using pro-inflammatory cytokine release assay (**Figure 4.8**). Pro-inflammatory cytokines (IL-1β, IL-6, and TNF-α) are important biomarkers to identify the immunoregulatory potential of nanoformulations. As documented in **Figure 4.8**, engineered BNcs are non-immunogenic as they exhibit minor response against IL-1β, IL-6, and TNF-α in comparison with the control cells and positive control (**Figure 4.8**). No significant levels of immunogenicity were observed for isolated NKM, bare PLGA NP, Gd-lipid in comparisons with the control cytokine levels (**Figure 4.8**). Only the positive control, LPS (3µg/mL), shows the

elevated levels of IL-1β, IL-6, and TNF-α in the tested cells. This clearly confirms the immuno compatibility of BNc for further *in vivo* imaging studies.

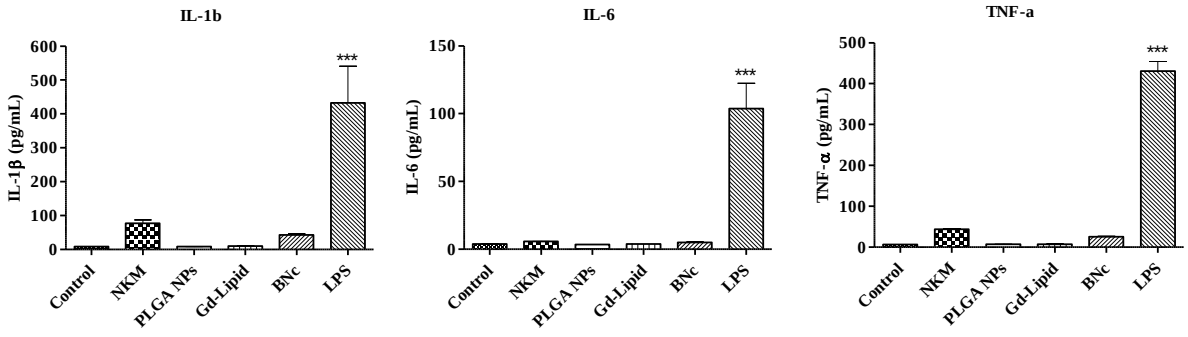

Figure 4.8. ***In vitro*** **immunogenicity of BNc** in THP-1 cells assessed by evaluating the proinflammatory cytokines (IL-1β, IL-6, and TNF-α) release after 24 h incubation.

With the assurance of BNc colloidal stability, *in vitro* cancer targeting, and biocompatibility, we moved forward to understand their *in vivo* targeting ability in immunodeficient NU/NU nude mice bearing an MCF-7 tumor. As shown in **Figure 4.9A**, DiR labeled BNc (10mg/kg) were injected via the tail vein, and the distribution of the particle was studied under live animal imaging over a period of 24h. Distinguishable kinetics of BNc accumulation in the tumor from 3, 6, 12, and 24 h, as shown by the increase in fluorescent intensity in the tumor, further suggests the tumor targeting ability of BNc. Accumulation of BNc over the 24h period also suggests us the blood availability of BNc, thereby providing us a key to its long circulating properties. After 24h of the imaging session, mice were euthanized, and the major organs were collected. These collected organs were washed with PBS and subjected to *ex vivo* fluorescent imaging (**Figure 4.9B**). *Ex vivo* imaging proves the overall tissue distribution of BNc with major accumulation in tumor and RES organs like liver and spleen. Compared to the control

group (bare PLGA NP), BNc show significant accumulation in the tumor which is twice as much as that of bare PLGA NP (**Figure 4.9C**).

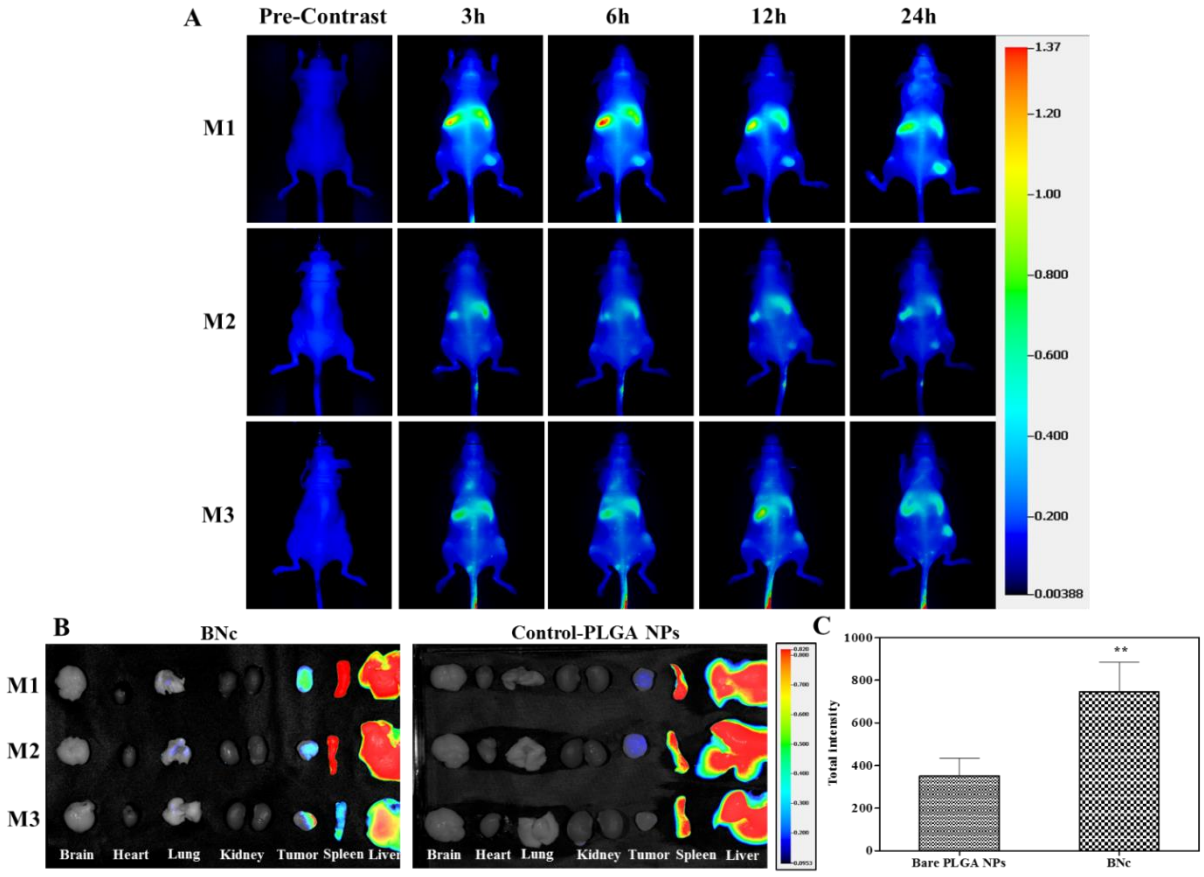

Figure 4.9 *In vivo* tumor-targeting ability of BNc. (A) Time dependent live animal imaging of MCF-7 tumor bearing NU/NU mice after intravenous injection of DiR-labelled BNc (10mg/kg). Images were recorded prior to injection and after 3h, 6h, 12h and 24h, respectively. (B) Bio-accumulation of BNc in tumor bearing mice after 24h post-injection. (C) Comparative tumor accumulation of BNc and Bare PLGA nanoparticles in MCF-7 tumor bearing NU/NU mice after 24h post-injection.

Next, *in vivo* pharmacokinetics of BNc was investigated after a single intravenous injection of 5 mg/kg of NP in MCF-7 tumor-bearing immunodeficient NU/NU nude mice. We used Gd^{3+} as a handle using ICP-MS to assess the pharmacokinetics and additional biodistribution studies. For this purpose, BNc were concentrated using Amicon Ultra centrifuge unit (3000 Da molecular

weight cutoff) and characterized for its hydrodynamic size and weight yield after lyophilization. Both size and weight of BNc were found to be consistent in a number of experiments conducted blindly by a research technician. **Figure 4.10A** shows the blood clearance of BNc after 72 h. The blood retention of BNc was found be high (60%) in the first 10h and it gradually reduced with time. The amount of BNc in the blood was determined using ICP-MS analysis. The biodistribution efficiency of BNc was investigated after a single intravenous administration of BNc (5 mg/kg). After 24h, animals were euthanized, and the major organs were investigated for the presence of BNc by estimating organ content of Gd using ICP-MS. The percentage of BNc in the liver and the spleen was found to be high, as they are the principal reticuloendothelial system that clears NP from the body. The percentage of BNc in the tumor tissue was found to be 10±3% of the injected dose (**Figure 4.10B**). This further confirms the tumor affinity of NKM fabricated BNc for targeted bioimaging applications and supports our results for NIR imaging session. The pharmacokinetic parameters of the BNc were obtained by fitting the concentration of BNc in blood and tissues with respect to time intervals and dosage using a two-compartmental model (MATLAB 2017b). **Table 4.2** shows the pharmacokinetic parameters of BNc in MCF-7 tumor-bearing NU/NU mice. The circulation half-life ($t_{1/2}$), area under the curve (AUC), volume of distribution (Vd), Clearance (CL), and mean resident time (MRT) of the BNc were found to be 9.51±6h, 1069±507 %ID h/mL, 3.85±1.16 mL, 0.28±0.14 mL/h, and 13.61±1.38 h, respectively.

Finally, the advantage of NKM coated BNc in MR imaging of tumors were demonstrated using 14.1T NMR system (Bruker Avance III, 600 MHz NMR-MRI). For *ex vivo* MR imaging, following our approved IACUC protocol, tumor animals were intravenously injected with BNc (equivalent Gd concentration of 0.008 mmol/kg) and euthanized after 2h. After euthanization, following our approved protocol for MRI, animals were rapidly imaged for T_1-weighted MR image

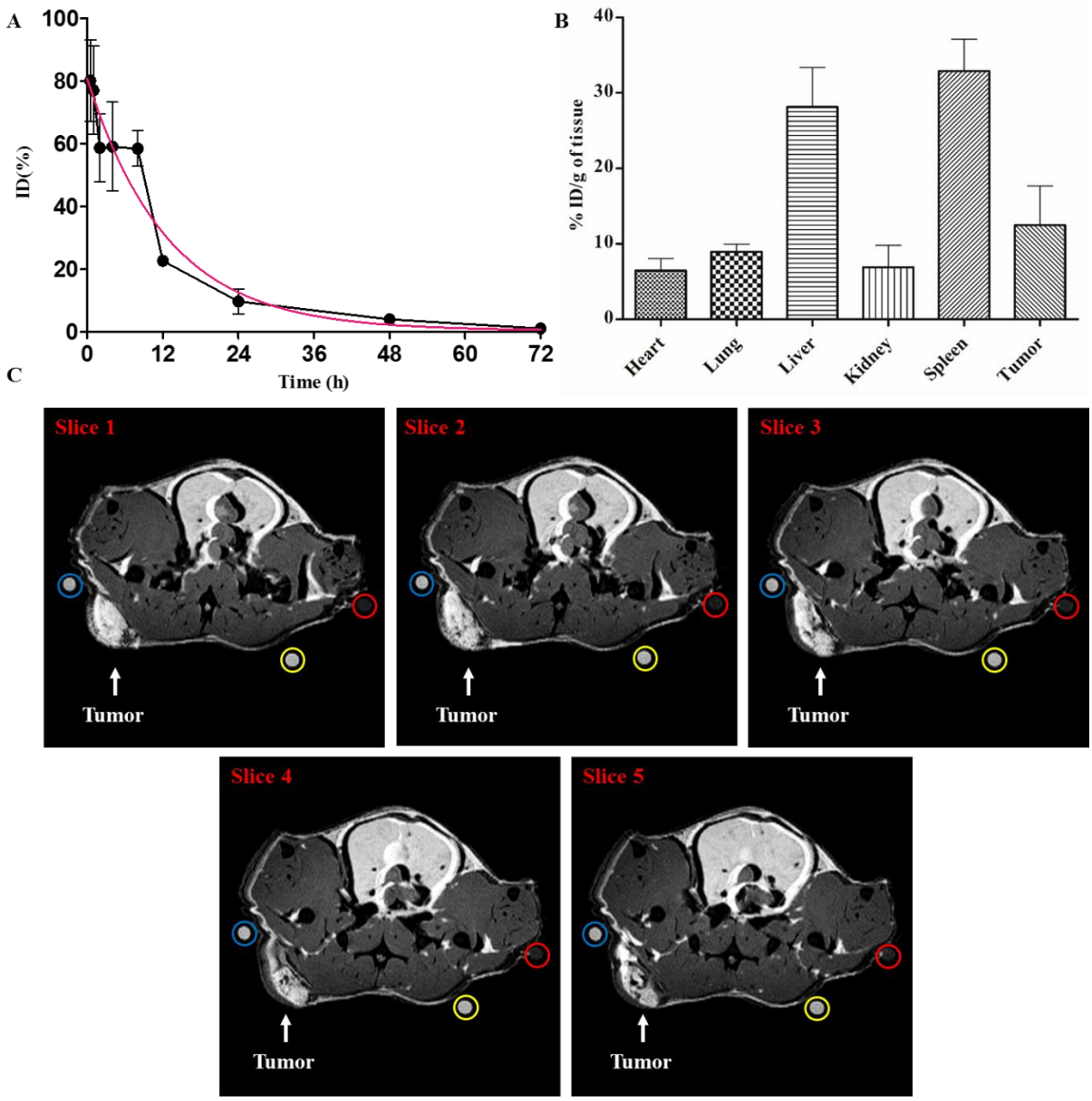

Figure 4.10. ***In vivo*** **pharmacokinetics and magnetic resonance imaging studies.** (A) Circulation half-life of BNc in MCF-7 tumor bearing NU/NU mice over 72h time. (B) Bio-distribution profile of BNc after single intravenous tail-vein injection in MCF-7 tumor-bearing NU/NU mice. (C) *Ex vivo* T1 weighted magnetic resonance image slices of NU/NU mice bearing MCF-7 tumor after 2h post-injection. Slice thickness: 0.5mm. Color circles indicate the standard controls; red: water, yellow: 18µM Magnevist®, blue: 37µM Magnevist®.

contrast, recorded using a QTR 30 mm coil with a FLASH protocol at 37ºC. **Figure 4.10C** shows the T_1-weighted MR images slice of NU/NU mice treated with BNc (Please see negative control MRI in **Figure B.2**). Compared with different image contrast of Gd standards, illustrated in different color circles (red: water, yellow:18μM Magnevist®, blue: 37μM Magnevist®), BNc shows distinctive brighter image contrast in tumor tissues. Along the various MRI slices (slice thickness of 500μm), it is clearly evident that the BNc were deeply penetrated into the tumor tissues and shown enhanced MR image contrasts to evaluate tumor as compared to that of surrounding soft tissue contrast. Comparing the data from MRI *ex vivo* imaging and data from *in vivo* NIR bioimaging, the engineered BNc show promises in targeting MCF-7 tumor.

Table 4.2 Pharmacokinetic parameters of BNc injected NU/NU mice by two-compartmental analysis.

PK parameters	**Biomimetic Nanoconstruct (BNc)**
$t_{1/2}$ (h)	9.51±5.74
AUC (%ID.h/mL)	1068.8±507.27
Vd (mL)	3.85±1.16
CL (mL/h)	0.28±0.14
MRT (h)	13.61±1.38

$t_{1/2}$*: half-life,* AUC*: Area under the curve,* Vd*: Volume of distribution,* CL*: Clearance,* MRT*: Mean residence time*

4.4 Conclusion

Herein, we described a biomimetic approach to fabricate a multifunctional NP system that has acquired properties from NK cells and studied its potential for tumor targeting and imaging. This hybrid platform technology, where synthetic and biological components were merged to exhibit unique properties, and consisting of both hydrophilic and hydrophobic assembly, shows versatile properties and feasibilities in surface functionalization and have a vacancy in the hydrophobic core for cargo encapsulation. Moreover, the existence of BNc in the cancer cells and the tumor as compared to that of bare particle suggested the dependence of targeting due to the acquired properties from the NK-92 cells. Considering the fact that successful cancer therapy requires drugs being precisely delivered to the tumors, the engineered BNc would have promises in drug delivery and monitor the therapeutic response in a single session.

Chapter 5 - Red Blood Cell Membrane Disguised Paramagnetic Polymeric Nanoparticle for Contrast Enhanced Magnetic Resonance Imaging

Abstract

Recent progress in bioimaging nanotechnology has greatly impacted on the diagnosis, treatment, and prevention of disease, especially by enabling early detection and diagnosis. Among different type of bioimaging modalities, magnetic resonance imaging (MRI) with a gadolinium-based contrast agent (GBCA) is one of the most commonly used in the clinic. These small molecular agents distribute rapidly between plasma and interstitial spaces following intravascular injection. They are ultimately eliminated through the renal route with half-lives of 1-2 h. Due to the short half-life of these agents, the clinical impact of this imaging technique is limited. To improve the usage of GBCA in diagnosis, herein, an effort has been put forth by incorporating GBCA into a nanoscale delivery system mimicking the property of red blood cell (RBC) that could facilitate contrast enhancement and prolong retention time in the biological system. The proposed nanoconstruct is made up of biocompatible/biodegradable poly(lactic-co-glycolic acid) (PLGA) polymeric core surface imprinted with RBC membrane and followed by the insertion of lipid conjugated GBCA. The proposed nanoparticle exhibits a hydrodynamic diameter of 120 ± 5 nm with a zeta potential of -25±2 mV and can load 8±0.3 wt% of gadolinium with robust stability in physiological and in blood serum condition. The retention of surface properties of RBC into the polymeric nanoparticle (PNP) was further confirmed by surface protein analysis. Upon the infusion of GBCA, the magnetic properties of PNPs exhibit r_1 relaxivity of 16±0.2 $mM^{-1}s^{-1}$ at 3 Tesla (T) which is five times greater than that of conventional clinically used MR contrast agent (i.e., Magnevist®, r1=3±0.15 mM-1s-1, 3T). As a result of higher relaxivity, it enhances the contrast in live animal and cell and the cell-free environments without causing toxicity. Given a higher magnetic and biomimetic property and stability, the biomimetic PNP proposed herein is a promising agent for therapy and diagnosis.

5.1 Introduction

Magnetic Resonance Imaging is one of the most routinely used imaging modalities in the clinic representing for total 4 million scans within the USA in 2017.[157,158] The extensive clinical use of MRI mainly attributed to its non-invasively abnormal detection of tissues and superior spatial and temporal contrast resolution when compared to that of X-ray and CT. The contrast in MR images are mathematically defined and converted based on the relaxation process of water proton within different tissue environment under strong external magnetic field. For example, when water protons undergo spin-spin T_2 relaxation process, no energy transfer occurs giving a negative contrast signal (dark images). On the other hand, when water protons undergo spin-lattice T_1 relaxation process, the absorbed energy transfers to surrounding tissue leading to the production of positive contrast signal (bright images). To further push forth the clarity of region-of-interest in advanced clinical image application, MRI is usually used in the presence of contrast agents. There are two main types of contrast agents that are classified based on their capability of altering the longitudinal (T_1) and transverse (T_2) relaxation time of the surrounding water protons. The T_2 based contrast agent, representing by super-paramagnetic iron oxide nanoparticles, generates a large local inhomogeneous magnetic field to shorten T_2 relaxation time, further enhancing the dark image.[14,159] On the other hand, T_1 based contrast agents, taken paramagnetic ions such as Gd^{3+} or Mn^{2+} as examples, facilitate bright contrast enhancement via proton-electron dipole interaction.[157] Due to the ability to produce a brighter image, T_1 contrast agents (particularly gadolinium-based contrast agents) become a preferable choice to use in the clinic for better image resolution and easy detection.

To date, approximately 40 out of 100 MR scans is acquired with the injection of GBCAs with a total up to 40 million administrations worldwide.[160] The current commercially available

GBCAs include Gd-DOTA (Dotarem®), Gd-HP-DO3A (ProHance®), Gd-BT-DO3A (Gadovist®), Gd-DTPA (Magnevist®), Gd-DTPA-BMA (Omniscan®), Gd-DTPA-BMEA (OptiMARK®), Gd-BOPTA (Multihance®), and Gd-EOB-DTPA (Eovist®). These gadolinium ions (Gd^{3+}) are chelated in linear or macrocyclic molecules comprising a total nine coordinating sites. Eight out of nine coordinate ligands bind tightly to Gd^{3+} to increase thermodynamic, kinetic stability and avoid toxicity related to free Gd^{3+}. Meanwhile, the remaining coordination site offers an open space for a single water molecule to impermanent bind and generate dipolar interactions with electron spins of gadolinium ion leading to an increase in magnetic relaxation of proton nuclei. This ultimately gives a contrast enhancement under MRI.[161,162] However, due to small chemical structure, those listed GBCAs tend to distribute throughout the body and quickly extravasate into interstitial compartment. Consequently, the ability to obtained precise image interpretation is hampered due to the increase of signal-to-noise ratio and short image window (inability of prolonging plasma residence time).[162–165] In the case of blood pool agent, the above mentioned limitations become more severe when contrast agent have to circulate for a longer time in the vascular lumen to obtain clinical relevant MR-images. As such, different strategies to incorporate GBCA into a nanoscale delivery system including liposome,[166] micelles ,[167–169] polymeric nanoparticle,[79,81] and dendrimer[170–172] have been extensively developed. However, the translational pathway of these engineered gadolinium-based nanoconstruct remains uncertain due to the difficulties of overcoming complex biological barriers of these exogenous synthetic materials.[19,173]

Recently, the development of biomimetic nanoparticle consists of cell membrane coating over synthetic core has drawn significant attention owing to its ability to translate natural materials into functional materials and conquering biological system. Over the last decade, a variety of cell

types and core materials were studied covering a broad spectrum of nanotechnology ranging from drug delivery,[70,137] vaccination,[174] detoxification,[71,175,176] immunotherapy,[177,178] and now starting to expand toward bioimaging arena.[179–182] By preserving complex biological functionalities of the cell membrane, the synthetic core can acquire the corresponding cellular designated biological function while keeping or enhancing their ordinary properties. Particularly in the field of bioimaging, different organic and inorganic imaging agents have been studied extensively for the possibility to conceal by cell membrane with the hope of further improving tumor diagnosis and tracking therapeutic response. Example of the application of cell membrane technology in MRI application can be seen in by hybrid nanoconstruct made up of red blood cell, cancer cell, and platelet cell membrane functionalized iron oxide and gadolinium-based nanoparticles.[179,182–184] The use of these proposed nanostructures has proven their outstanding disease targeting properties for the improvement of diagnosis and therapy.

Although the functional role of the biomimetic delivery agent is well-documented, the in-depth understanding on the variations in its performance at the structural levels, such as when the contrast agent is arranging in the biomimetic system, have not received sufficient attention. In the context of MRI, the questions regarding physical effects such as the imaging probe orientation, water exposure, protein interference, confinement, and quenching effects are still waiting for the investigation. Encouraged by these unanswered questions, we sought into constructing a biomimetic imaging nanoconstruct that allowed us to take a deep understanding of a structural relationship of cell membrane coating and MR contrast agent. We further extended knowledge gained to elucidate their corresponding MR mechanism on image enhancement and biological performance under *in vitro* and *in vivo* conditions. This study resulted in an optimized red blood cell membrane disguised gadolinium-based PNP for tunable T_1 relaxivity. The isolated RBC

membrane directly fused onto polymeric core pre-labeled with gadolinium lipid conjugate. The biomimetic strategy allowed to conceal contrast agent from the endogenous components resulting in a long circulating and high longitudinal relaxivity for improved MRI visualization of the vascular lumen.

5.2 Materials and Methods

Material and chemical

50:50 Poly(D,L-lactide-co-glycolide) carboxylate end group (0.55-0.75 dL/g) was purchased from DURECT Corporation (Birmingham, AL, USA). 1,2-distearoyl-*sn-glycero*-3-phosphoethanolamine (DSPE), 1,2-dipalmitoyl-sn-glycero-3-phosphoethanolamine-N-(succinyl) (sodium salt) (16:0 Succinyl PE), and L-α-Phosphatidylethanolamine-N-(lissamine rhodamine B sulfonyl) (Ammonium Salt) (Egg-transphosphatidylated, Chicken) (Egg Liss Rhod PE) were purchased from Avanti Polar Lipid Inc. (Alabaster, AL, USA). *N*-Hydroxysuccinimidyl ester activated 1,4,7,10-tetraazacyclododecane-1,4,7,10-tetraacetic acid (DOTA-NHS) was purchased from Macrocyclics (Dallas, TX). Gadolinium (III) acetate hydrate ($Gd(OAc)_3$) were purchased from Sigma-Aldrich (Milwaukee, WI, USA). All other chemicals and solvents were purchased from Sigma-Aldrich (Milwaukee, WI, USA) and used as received.

Cell line and animal model

Human peripheral blood monocyte THP-1 cells were maintained in RPMI medium with 10% (v/v) fetal bovine serum (FBS) and penicillin/streptomycin (100μg/mL) and maintained at 37 °C in 5% CO_2 environment. Macrophage (J774) was purchased from ATCC and maintained in Dulbecco's Modified Eagle's Medium (DMEM) supplemented with 10% (v/v) FBS and penicillin/streptomycin (100μg/ml) and maintained at 37 °C in 5% CO_2 environment.

Six-week-old female NU/NU nude mice were procured from Charles River Laboratories International, Inc. and used for the study after ten days acclimatization. All animal experiments and protocols were approved by the Institutional Animal Care and Use Committee (IACUC) and Institutional Biosafety Committee (IBC), Kansas State University, Manhattan

Synthesis of DSPE-DOTA-Gd

The synthesis of Gadolinium ion chelated DSPE-DOTA was performed using a two-step preparation method as previously described with some modifications. In brief, 75 mg of DSPE was first dissolved in 10 mL chloroform containing 2% (v/v) triethylamine (TEA). The mixture was stirred for 30 mins at room temperature to activate the amine end group of DSPE. After that, 86 mg DOTA-NHS ester was added and stirred vigorously until all reagents were completely dissolved. The reaction was allowed to take place for another 3 h at 40ºC. At the end of incubation, the obtained clear reaction mixture was concentrated and dried under vacuum to recover white powder. To purify the conjugating DSPE-DOTA lipid, 6 mL of deionized water was used to disperse reaction crude, the suspension underwent 5 cycles of freezing and thawing in liquid nitrogen and 60ºC water bath, respectively, and then centrifuged at 4500 g for 10 mins. The resulted DSPE-DOTA suspension was filtered through a 0.2 µm membrane to remove insoluble by-product and lyophilized to get dry powder.

The gadolinium ion was thermodynamically chelated to DSPE-DOTA conjugated lipid under an acidic condition at 50ºC. Specifically, 50 mg DSPE-DOTA (0.05 mmole) was hydrated in 10 mL of acetate buffer (pH = 5.5) and further treated with 0.1 mmole of $Gd(OAc)_3$ 50ºC for 12 h. After incubation, the Gd-DOTA-DSPE was purified by centrifugation at 4500g for 10 min. The obtained white product was washed 3 times with acetate buffer (pH 5.5) and 2 times with water to remove all non-chelated Gd^{3+} ion. The samples were lyophilized to obtain a dry powder. The

percentage yield of the gadolinium concentration in the reaction mixture was analyzed by using Inductively Coupled Plasma Mass spectrometry (ICP-MS, Perkin Elmer, NEXion 350X). The resulting yield was 98%.

Red blood cell membrane extraction

Red blood cell membrane (RBC-M) was extracted from whole blood using hypotonic treatment.[71] In brief, whole blood was centrifuged to remove any buffy coat and plasma and mixed with 10 volume of Mili-Q water to disrupt RBC. The aliquot was sonicated briefly using bath sonication for 5 mins to hemolysis RBCs. The blood suspension was then centrifuged at 5,000 rpm for 5min to separate RBC-M from the hemoglobin by carefully removing the suspension. The RBC-M pellet was washed several times to remove hemoglobin completely. The purified RBC-M was stored at -20ºC for further use. The amount of protein in extracted RBC-M was quantified by bicinchoninic acid (BCA) assay.

Preparation and characterization of red blood cell membrane coated paramagnetic polymeric nanoparticles (RBC-Gd-PLGA)

RBC-Gd-PLGA nanoparticles (NPs) were prepared by nanoprecipitation technique following by imprinting of RBC membrane on the surface. In brief, the paramagnetic polymeric cores were prepared by adding dropwise 100μL of PLGA in acetonitrile stock (10mg/mL) into 1mL Milli-Q water containing various amount of Gd-L (50, 100, 150, 200, and 400 μg/mL) under magnetic stirring condition. The mixture was stirred continuously overnight to evaporate off the organic solvent. The final RBC-Gd-PLGA were fabricated by coating RBC-M onto 1 mg of preformed paramagnetic polymeric cores at various membrane protein amount (1, 5, 10, 100, 250, 500, and 1 mg) using bath sonication (Branson CPXH 2800, 40kHz) for 10 mins with 50% power.

The sample was further purified using Amicon Ultra-4 centrifugal filter (Millipore, MA) with a molecular weight cut-off of 10 kDA and stored at 4 °C for further use.

Rhodamine dye labeled RBC-Gd-PLGA was prepared by mixing 30µg of L-α-Phosphatidylethanolamine-N-(lissamine rhodamine B sulfonyl) (Ammonium Salt) (Egg Liss Rhod PE) with Gd-L suspension prior to the fabrication of paramagnetic polymeric core.

Characterization of RBC-Gd-PLGA

The hydrodynamic size and zeta potential of the RBC-Gd-PLGA were characterized using Dynamic light scattering analysis (Malvern, Nano ZSP). The morphology of RBC-Gd-PLGA was further confirmed using transmission electron microscope (FEI Technai G2 Spirit BioTWIN). TEM samples were prepared by incubating 50 µL of RBC-Gd-PLGA (200µg/mL) with 50 µL of 2% Uranyl acetate for 2 mins at room temperature. The sample was then placed on a fomvar coated copper grid (400 mesh) and let stand for an additional 5 mins. The excess amount of sample was removed prior to TEM acquisition. TEM images were acquired at 120kV and analyzed by GATAN digital imaging system (GATAN, Inc.).

The serum stability of the prepared PLGA NPs, Gd-PLGA, RBC-PLGA, and RBC-Gd-PLGA were carried out as reported. Specifically, 150µL of 1mg/mL nanoparticles were incubated with 50µL of Fetal Bovine Serum at 37°C. The change in absorbance at 560nm was measured kinetically every 6s over a period of 1h, a double-orbital shaking with slow speed was applied prior to each measurement using Microplate reader (BioTek, Synergy H1 hybrid reader).

The stability at physiological condition was investigated by dispersing nanoparticles in phosphate buffer saline (PBS, pH 7.4) at the particle concentration of 1mg/mL. The nanoparticles

were incubated at 37°C for 7 days. The changes in hydrodynamic size were tracked daily using Dynamic light scattering analysis

Fluorescence resonance energy transfer

To track the insertion of RBC-M onto the surface of Gd-PLGA, fluorescence resonance energy transfer study was conducted. For the experiment, a FRET pair of chromophores, a fluorescent donor (L-α-phosphatidylethanolamineN-(4-nitrobenzo-2-oxa-1,3-diazole) (Ammonium Salt) (Egg-transphosphatidylated, Chicken), PE-NBD and a fluorescent acceptor (L-α-Phosphatidylethanolamine-N-(lissamine rhodamine B sulfonyl) (Ammonium Salt) (Egg-transphosphatidylated, Chicken) PE-RhB, was incorporated separately into RBC-M vesicle and Gd-PLGA (or PLGA) with a 3:7 mole ratio, respectively. In particular, the NBD labeled RBC-M vesicles were prepared by sonicating 250 μg RBC-M with 30 μg PE-NBD for 10 mins. Similarly, 99.4 μg PE-RhB was used to label 1 mg PLGA or Gd-PLGA by dispersing in 1 mL water/Gd-lipid suspension prior to polymeric core fabrication.

Typical fusion study was performed by mixing 100 μL of NBD-RBC with 100 μL RhB-PLGA/RhB-Gd-PLGA. The mixture was incubated for a varying period (5, 30, and 60 mins) at 37ºC with gentle shaking or bath sonicated for 10 mins. Thereafter, 100 μL of the suspension was used to record the fluorescence emission spectrum at λ_{ex} = 470 nm and λ_{em} = 500-700 nm.

The *in vitro* structural integrity of the RBC-Gd-PLGA was also assayed by labeling core and shell of RBC-Gd-PLGA with different color dyes following the aforementioned protocol. The colocalization of NBD and RhB fluorescent was studied using K7M2 cells, and fluorescent images were acquired with a Confocal Laser Scanning Microscope.

Red blood cell membrane protein characterization

The retention of characteristic proteins of the red blood cell membrane and its translocation into paramagnetic polymeric core was confirmed by SDS-PAGE analysis, dot blots and western blot. For SDS-PAGE analysis, whole cell lysate, RBC-M, RBC-Gd-PLGA samples were prepared at a protein concentration of 300 μg/mL. RBC-Gd-PLGA were collected by centrifugation at 13,000 rpm for 30 mins and redispersed in gel loading dye. All samples were heated at 90 °C for 5 min, and 20 μL of samples were loaded into wells of 4–20% Mini-PROTEAN® TGX Protein Gels and stained using Coomassie Brilliant Blue. For Western blot analysis, proteins were transferred to PVDF membrane by the wet-blot method. The transfer was carried out for 1 hr at 2500 mA, 500 W, and 100 V. After that, the membranes were blocked in 5% milk in TBST for 30 mins at room temperature under rocking condition. The membrane was subsequently treated with primary antibodies for Glycophorin A (Santa Cruz), β-actin (Santa Cruz), and CD47 (Santa Cruz) along with HRP-conjugated anti-mouse IgG secondary antibody (Cell Signaling). The blotted films were further developed using SignalFire™ ECL Reagent (Cell signaling) and imaged for chemiluminescence signal under Bio-imager (Kodak).

Gadolinium loading and release study

The cumulative gadolinium release from the RBC-Gd-PLGA was assessed at 37°C under physiological and endogenous ionic condition. In brief, RBC-Gd-PLGA (1mg/mL, 2mL) were placed in a dialysis bag membrane (Mw. Cutoff=500Da) and dialyzed against 250mL of PBS (pH=7.4) under shaking condition (100rpm). At predetermined time intervals, 500μL of the sample was collected and replaced by 500 μL fresh media. The amount of released Gd was quantified by ICP-MS. As a control experiment, 25μg/mL of gadolinium (III) acetate was placed in a dialysis bag and processed under the same condition.

Relaxation properties

Effect of coating on magnetic property: The changes of longitudinal relaxation time in the presence and absence of RBC membrane coating was investigated under clinical MRI (3 Tesla). Five different concentrations of GdL input (400, 200, 100, 50, and 25 µg/mL) were used to prepare RBC-M coated, and non-coated NPs follow the abovementioned protocol. A serial dilution of samples was prepared prior to MRI acquisition. The longitudinal relaxation time of RBC-Gd-PLGA in an aqueous solution at different Gd^{3+} concentration was obtained at 25^0C using a fast spin echo sequence with variable repetition time. Scans were performed with the following imaging parameters: repetition time (TR)= 6000, 3000, 1500, 800, 600, 400, 200 ms, echo time (TE) = 10 ms, slice thickness=2 mm, flip angle (FA) =90^0, image size 256×256, FOV=25.6×25.6. The representative T_1 weighted magnetic resonance phantom images of RBC-Gd-PLGA were taken at TR=400 ms, TE=10 ms, and slice thickness = 2mm. The longitudinal coefficient relaxivity value r_1 was determined from the slope of the plot of $1/T_1$ versus the sample concentration. Magnevist with similar Gd^{3+} was used as a control.

Effect of gadolinium lipid density of magnetic property: The gadolinium lipid density on the surface of the polymeric core was tuned by changing the feed amount of GdL while keeping all other parameters (volume of water, amount of polymer, and RBC-M protein) constant. The samples were concentrated to get final GdL concentration of 100 µg/mL. The longitudinal relaxation time of RBC-Gd-PLGA in an aqueous solution at different Gd^{3+} concentration was obtained as described above. The longitudinal coefficient relaxivity value r_1 was determined from the slope of the plot of $1/T_1$ versus the sample concentration. Magnevist with similar Gd^{3+} was used as a control.

In vitro immunogenicity assay

The immunoregulatory potential of the prepared nanoparticles was tested standard cytokine analysis assay. In brief, 4×10^5 human monocytic cell line (THP-1) were seeded in a 24-well plate and treated with bare PLGA NPs (10μg/mL), RBC-M (10μg/mL), Gd-lipid (10μg/mL), and RBC-Gd-PLGA (10μg/mL) at 37°C for 24h. After 24h incubation, cell culture supernatants were collected, centrifuged to remove cell debris and stored at -20°C for further analysis. For cytokine assay, samples were thawed and analyzed for pro-inflammatory cytokines, IL-1β (LOD:1.7 pg/ml), IL-6 (LOD:1.5 pg/mL) and TNF-α (LOD:1 pg/mL) using Magnetic Human Cytokine Multiplex Assays Kit (R&D Systems, Inc. Minneapolis, MN) in Luminex MagPix® instrument (Millipore Inc.,) as manufacturer recommendations. For positive control, cells were treated with 5μg/mL of lipopolysaccharide for 24h.

In vitro macrophage uptake study

J774 murine macrophage cells were plated at a density of 20,000 cells per well on an 8-well chamber slide (BD Biosciences). After 24hr, cells were treated with RhB labeled PLGA, RBC-Gd-PLGA, and PEGylated NPs with a final NP concentration of 50 μg/mL and incubated over varying periods (0.5, 1.5, 3, and 6 hrs). After incubation, the treated cells were washed twice with 1× PBS (pH 7.4), fixed with 4% paraformaldehyde for 15 min at room temperature, stained with DAPI for an additional 10 min, mounted with Fluoromount aqueous medium (Sigma-Aldrich), and imaged using CLSM (Carl Ziess, LSM-700). The cellular uptake was assessed by measuring RhB fluorescence intensity using Image-J software (National Institute of Health). The data were analyzed using one-way ANOVA with Turkey's multiple comparison post-test.

Circulation half-life and bio-distribution study

To assess the accumulation of contrast agents in the different tissues, the amounts of Gd^{3+} in organs at predetermined time points after injection of RBC-Gd-PLGA or Magnevist were analyzed by ICP-MS. In brief, each mouse was administrated of Gd^{3+} at a dose of 0.05 mmol Gd^{3+}/kg body weight of mouse in 100 μL PBS (Clinical Gd dose is 0.1 mmol/kg).[185] At an appropriate time after the intravenous injection, blood was collected and the mice were euthanized, different tissues were collected, weighed, and completely digested in 1.0 mL solution of 70% nitric acid through heating at 90°C for 8 hrs. After digestion, the solution was filtered and diluted. The Gd^{3+} concentrations in the samples were determined by calculating with a standard curve obtained with using Gd(III) calibration standard.

In vivo Magnetic Resonance Imaging

In vivo MRI study was performed using NU/NU mice on a 3T MRI clinical scanner. In brief, the mice were intravenously injected with RBC-Gd-PLGA (equivalent Gd concentration of 0.017 mmol/kg) or Magnevist (equivalent Gd concentration of 0.03 mmol/kg). The MRI images were acquired immediately at injection and post-injection at 15 mins and 30 mins. The T1-weighted MR images were recorded using fast spin echo sequence. The recorded images with different slices were subtracted with pre-contrast images and processed using maximum intensity projection. All images were analyzed using Medical Image Processing, Analysis, and Visualization (MIPAV) software. All animal experiments and protocols were approved by the Institutional Animal Care and Use Committee and Institutional Biosafety Committee, Kansas State University, Manhattan.

5.3 Result and Discussion

RBC membrane is one of the first biological materials that was utilized to provide effective concealment for nanoparticles.[69,70] A variety of nanoparticle type has been tested for the possible incorporation of this biologically derived material to extend their use to cover a broad spectrum biomedical application ranging from drug delivery, detoxification to bio-sensors.[71,137,179,180,186] Among different type of core materials being tested, PLGA is well known for its capability of being coated by RBC membrane. Even though the molecular mechanism underlying the cloaking of the cell membrane and the synthetic nanoparticle is unclear, the hybridization between RBC-membrane and PLGA core was suggested to be in favor of negatively charged core with right-side-out membrane conformation.[187,188] Adapting the well-established protocol of RBC membrane coating over PLGA nanoparticle, we engineered a biomimetic paramagnetic polymeric nanoparticle with the inclusion of Gadolinium ion (a paramagnetic ion) to obtain a long circulating MRI contrast agent.

To achieve a stable paramagnetic complex that can be inserted on the surface of biomimetic nanoconstruct, we conjugated 1,4,7,10-tetraazacyclododecane-1,4,7,10-tetraacetic acid (DOTA)-a cyclic gadolinium macro-chelator to the hydrophilic head of phospholipid using carbodiimides follow by N-hydroxysuccinamide (EDC/NHS) crosslinking reaction (**Figure C.1**). The obtained modified lipid (DOTA-DSPE) was incubated with Gadolinium Acetate at pH 5 to entrap Gd^{3+} into DOTA chelator yielding gadolinium lipid or GdL. Owing to the amphiphilicity, nanoprecipitation of PLGA polymer in GdL suspension spontaneously form a lipid-polymer paramagnetic nanoparticle core. To further enhance the biological functionality and stability, we conceal the surface of lipid-polymer hybrid nanoparticle with RBC-M using sonication technique. The amount of RBC-M used to coat paramagnetic nanoparticle was optimized by varying the amount of RBC-

M protein input. The optimal concentration of 750 µg protein/ 1mg particle core was chosen due to the excellent stability in physiological pH 7.4 over a long incubation time (**Figure C.2** and **C.3**). Upon coating RBC-M, a core-shell structure was obtained as evidence in TEM image **(Figure 5.1B)** with a core diameter of 48 ± 10 nm and the shell thickness of 9 ± 2 nm (**Figure C.4**). Both Gd-PLGA and RBC-Gd-PLGA exhibited similar hydrodynamic diameter around 120 ± 5 nm **(Figure 5.1C)**. The significant different between TEM and hydrodynamic size is presumably due to the presence of hydrated glycan moieties of protein on the surface of the RBC membrane.[188] In naïve RBC, the glycan is responsible for maintaining negatively charged property and avoid the attachment with other cells while circulating.[189] While translocation onto the engineered nanoconstruct, besides the biological designated properties, the polysaccharide moieties on the cell membrane is capable of forming hydrogen bonding with a water molecule, hence forming a thick hydrating layer which contributes to the stability of nanosystems. The successful insertion of the RBC membrane on the surface of the paramagnetic polymeric core was further confirmed by surface zeta potential. The highly negative charge of Gd-PLGA core (-40mV) was shifted toward more positive number (-26 mV), equivalent to that of RBC, displaying a median charge value between Gd-PLGA core and RBC-M surface upon fusion of RBC-M **(Figure 5.1D).** With the presence of RBC-M, RBC-Gd-PLGA became highly stable under serum condition in a similar manner to that of RBC-PLGA, whereas uncoated PLGA and Gd-PLGA were immediately aggregated as indicated by the increase in absorbance at 560 nm **(Figure 5.1E)**.

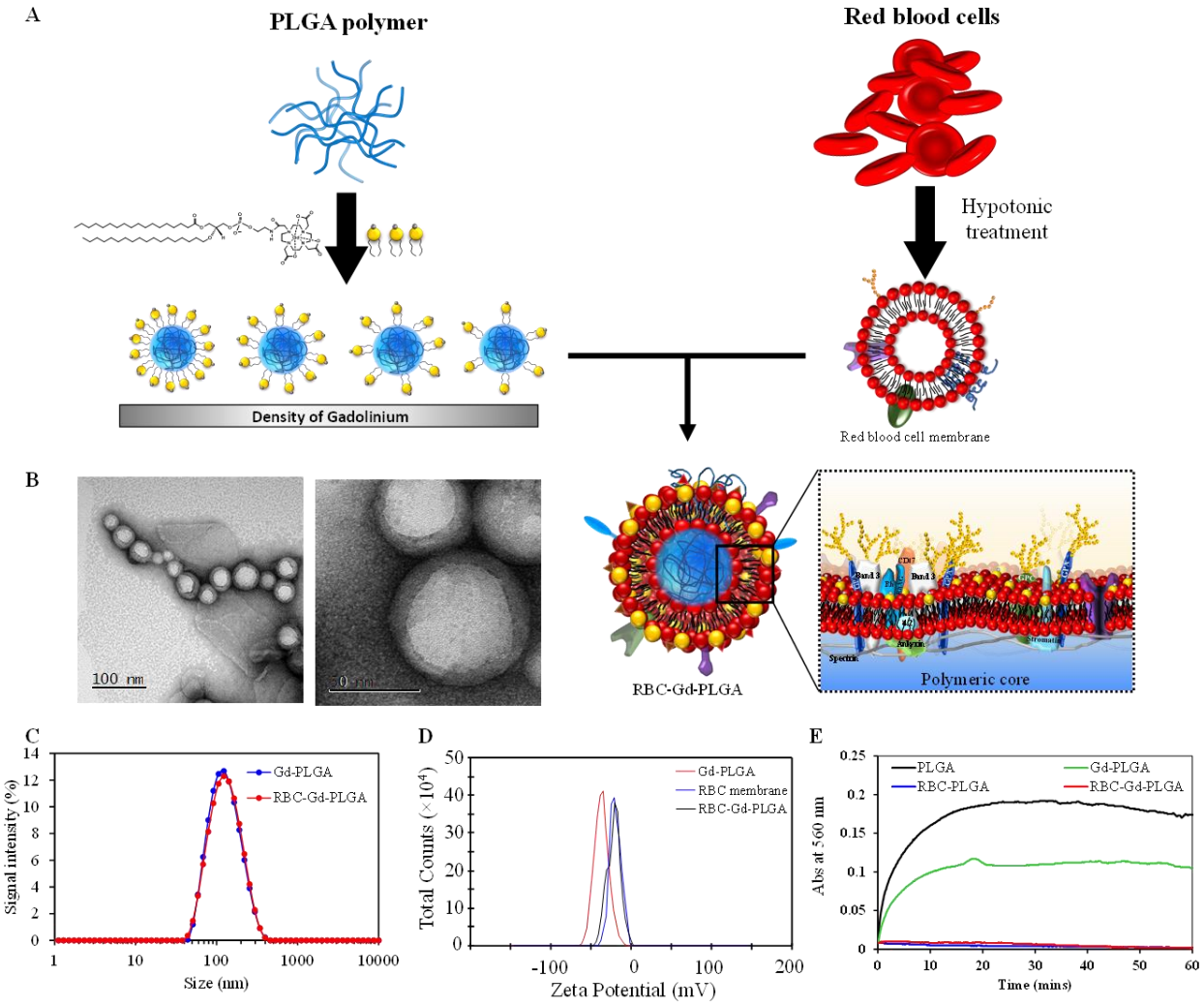

Figure 5.1 Design and characterization of RBC-Gd-PLGA. (A) Schematic illustration of the preparation of biomimetic paramagnetic nanoconstruct made up of the red blood cell membrane, Gd-Lipid, and PLGA using lipid insertion process. (B) Transmission electron microscopy (TEM) image of RBC-Gd-PLGA NPs negatively stained with uranyl acetate. (C) Hydrodynamic size of bare Gd-PLGA cores, RBC membrane-coated Gd-PLGA measured by dynamic light scattering (DLS). (D) The surface zeta potential of bare Gd-PLGA, RBC membrane vesicles, and RBC-Gd-PLGA showing the shift of surface charge upon the insertion of RBC membrane onto the Gd-PLGA NPs. (E) Serum stability test measured dynamic aggregation of nanoparticles using 90% serum environment, here we look at the rapid increase in optical density of 560 nm due to NPs aggregation in serum protein.

When nanoparticle travel in the bloodstream, the surface of nanoparticle serve as the first point of cell recognition which directly determines the effectiveness of nanoparticle's performance

in biological condition. In many cases, under physiological condition, the binding of endogenous materials such as proteins can form the protein corona on the surface of nanoparticle which further alters the physiological properties and the *in vivo* fate of nanoparticle. To prevent this scenario, we utilized the RBC membrane as a concealment layer to (1) limit the absorption of protein on the surface of nanoparticles and (2) protecting Gd complex from other endogenous ions. The insertion of RBC-M onto paramagnetic nanoparticle was monitored by fluorescence resonance energy transfer (FRET) in which the distance of fluorophores can be monitored based on the energy transfer phenomenon between electron donor and acceptor. The NBD-PE (electron donor) lipid was used to labeled RBC membrane by sonication while RhB-Egg PC (electron acceptor) labeled paramagnetic polymeric core was prepared during nanoprecipitation. As the distance between NBD labeled RBC-M and RhB-labelled became shorter, the NBD fluorophore can be more efficient in donating an electron to the RhB fluorophore. As a result, the fluorescent intensity of NBD peak at 525 nm would be diminished while the fluorescent signal of RhB at 600 nm would be enhanced, which we observed in our experiment as depicted in **Figure 5.2B and 5.2C**. The FRET phenomenon took place in a time-dependent manner in which FRET efficiency increased up to 45% (RBC-M and PLGA) and 54% (RBC-M and Gd-PLGA) over 60 minutes of incubation **(Figure C.5)**. The translocation process of cell membrane onto paramagnetic nanoparticle core can be facilitated by brief sonication (~ 30 sec) follow by incubation leading to the improvement of FRET efficiency up to 60% (RBC-M and PLGA) and 71% (RBC-M and Gd-PLGA). In all cases, the %FRET efficiency of RBC-M with Gd-PLGA is higher than that of RBC-M with PLGA, indicating that the RBC-M is more effective in infusing onto the surface of paramagnetic nanoparticle core than that of bare PLGA. This observation indicated that synthetic Gd complex (Gd-lipid) might provide the additional driving force for the rearrangement of RBC-M on the polymeric core.

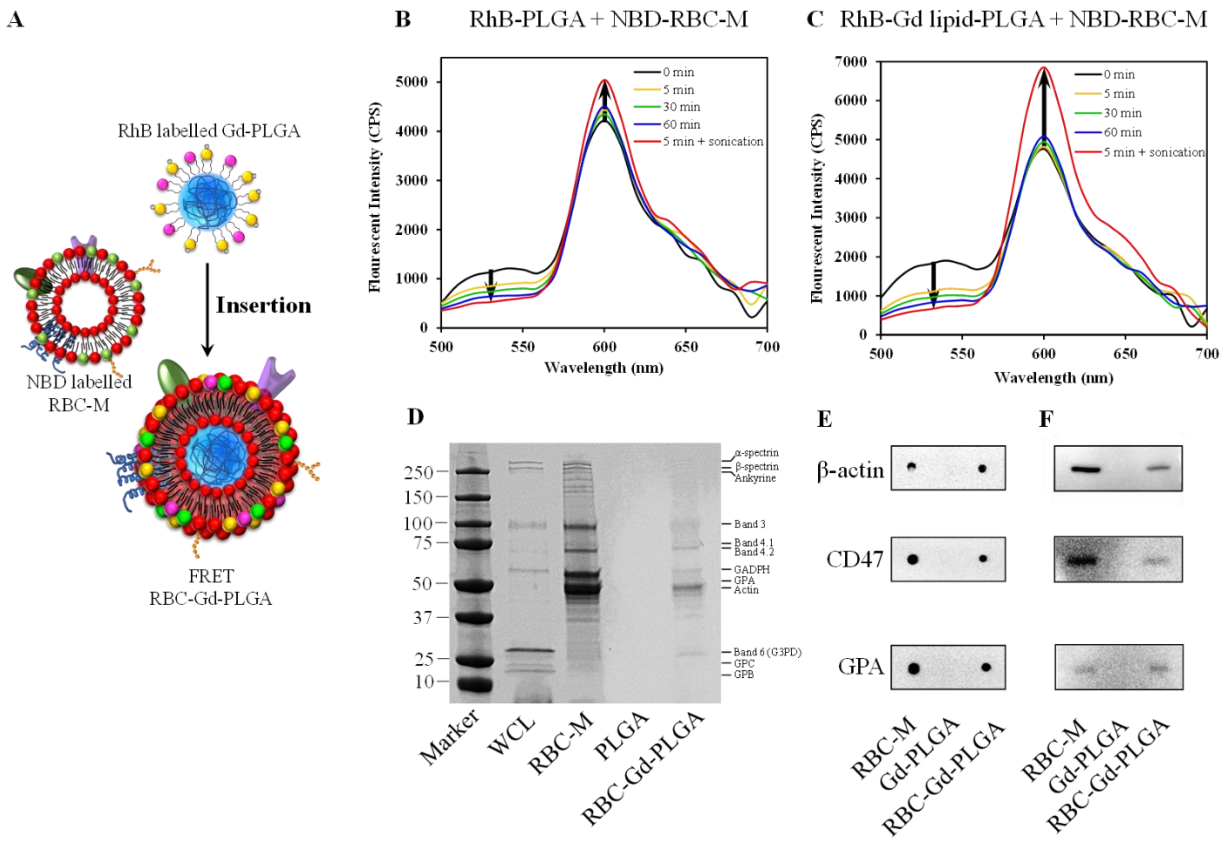

Figure 5.2. Protein characterization of RBC-Gd-PLGA. (A) Schematic representation of the re-arrangement of the cell membrane and synthetic lipid and typical characteristic proteins presence on RBC membrane. (B) and (C) FRET study showing the insertion of RBC-M onto the Gd-PLGA in the manner similar to that of bare PLGA. (D) The SDS-PAGE analysis of protein bands in a whole cell lysate, isolated RBC-M, PLGA, and RBC-Gd-PLGA. (E) and (F) Dot blot and western blot analysis, respectively, of RBC-Gd-PLGA depicting the presence of characteristic proteins, β-actin, CD47, and Glycophorin A.

To further confirm the successful translocation of RBC-M onto proposed nanoconstruct, we conducted SDS-PAGE and western blot analysis. The total proteins profile of RBC-M and RBC-Gd-PLGA were well-resolved on SDS-PAGE gel with the typical bands of spectrin, band 3, band 4, GAPDH, Glycophorin A, and Actin (**Figure 5.2D**). More specifically, CD 47 - a major "don't-eat-me" protein responsible for the survival of RBC *in vivo* was observed in dot blot and western blot for both RBC-M and RBC-Gd-PLGA (**Figure 5.2E and F**). In addition, the presence

of Glycophorin A (GPA), one of the most abundant transmembrane protein of RBC was also confirmed (**Figure 5.2E and F**). Glycophorins are densely glycosylated and contain a sialic acid molecule that was proven to give the cell structural integrity and mechanical properties.[189] The removal of glycoprotein causes the collapse of RBC-PLGA NPs as indicated in a previous publication.[188] Hence the presence of both CD 47 and GPA in our nanoconstruct help us to ensure the stability and immune evasion of RBC-Gd-PLGA when used in *in vivo* environment.

After getting the confirmation of the structural arrangement of nanoconstruct, the retention efficiency of GdL on the surface of biomimetic nanoparticle was investigated by inductively coupled plasma mass spectroscopy (ICP-MS). The amount of Gd^{3+} in RBC-Gd-PLGA was varied by changing the feed amount of GdL (50, 100, 200, and 400) while keeping the polymer weigh constant in the polymeric core preparation step. As a result, five different cores were obtained and underwent RBC-M coating (the same amount of protein membrane was used in all cases) using the same protocol as describe above. As shown in **Figure 5.3A**, the retention efficiency of GdL increased from 75% to 90% as the initial input of GdL increased from 50 to 400 μg per 1 mg of PLGA polymer. Note that when the concentration of initial GdL input fell below 25μg, the bare paramagnetic polymeric core became unstable and aggregated. This phenomenon together with the increase of GdL retention efficiency indicates that the PLGA core surface is partially stabilized and capable of holding a different density of GdL. Furthermore, the Gd^{3+} release under various physiological condition was examined. As we anticipated that the RBC-Gd-PLGA nanoconstruct could be served as a blood pool contrast agent, the phenomenon such as transmetalation with endogenous scavenger cations (Zinc, Iron, and Copper ion) while traveling in the bloodstream should be minimized in order to achieve a better safety profile. Therefore, the RBC-Gd-PLGA was challenged with different ion media in simulated body fluid. The Gd^{3+} release characteristics of

RBC-Gd-PLGA was mapped in term of cumulative Gd^{3+} release from a 500 Da dialysis bag. This selected molecular weight cutoff gives a free passage of all ion presence in the media. As a result, in simulated body fluid (pH 7.4), RBC-Gd-PLGA appeared to be highly stable with just 1% cumulative release over 72 hours of incubation (**Figure 5.3B**). On the other hand, the amount of Gd^{3+} released from Magnevist (a clinical contrast agent) under the same condition increase significantly as the incubation time increase leading to the cumulative release of 10% at 72hr of incubation **(Figure 5.3B)**. All of this information together confirms the stability of Gd^{3+} in the nanoconstruct.

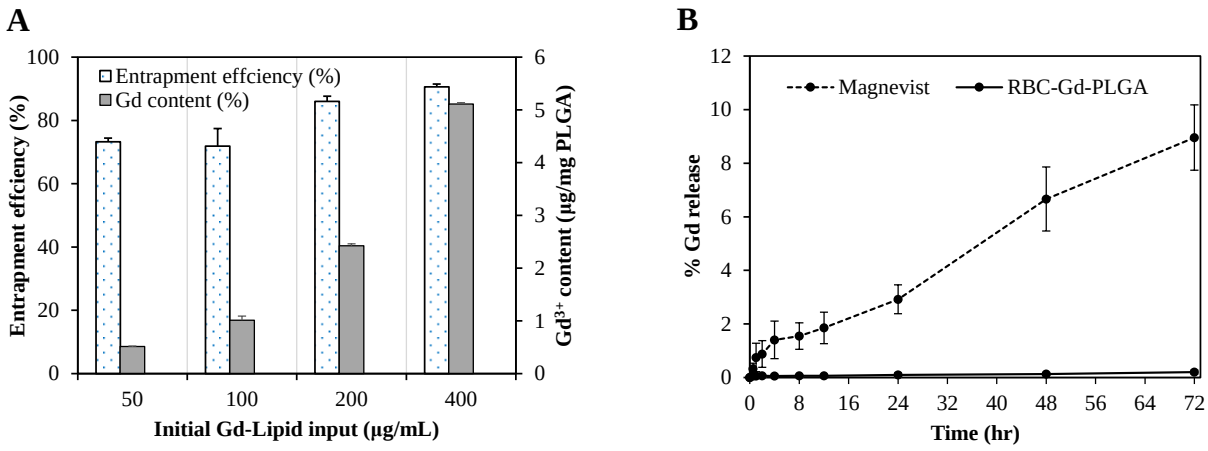

Figure 5.3 Gadolinium loading and release study. (A) Gd^{3+} loading efficiency of RBC-Gd-PLGA with different initial input concentrations of Gd-lipid. (B) Gd^{3+} release characteristics of RBC-Gd-PLGA in simulated body fluid at 37°C.

To investigate the MRI contrast of the RBC-Gd-PLGA, we first looked into the effect of cell membrane coating on the magnetic relaxivity of the nanoconstruct. Two sets of samples in the presence and absence of RBC coating with different GdL input concentrations were fabricated. The phantom image revealed that the contrast is slightly enhanced when paramagnetic core coated with RBC-M (RBC-Gd-PLGA) as compared to that of non-coated counterpart (**Figure 5.4A**).

Specifically, the contrast was enhanced by 10 % upon cell membrane coating. This type of slight contrast enhancement can be explained on the basis of two possible reasons (1) the proteins presence in the cell membrane outer layer introduce mass and steric hindrance surrounding paramagnetic Gd^{3+} ion, leading to the restriction in rotation and retardation in molecular tumbling time and (2) the carbohydrate moieties on the outer layer trap water molecules via hydrogen bonding, creating a water proton in close proximity with paramagnetic Gd^{3+} ion, accelerating water exchange phenomenon. Both mechanisms are well known to enhance the longitudinal relaxivity of gadolinium-based contrast agents and have been successfully adapted into the design of commercially used albumin-targeted contrast agent (MS-325).[190] Within the cellular construct, a similar effect also can be seen when GdL is inserted into the lipid bilayer of naïve RBC as reported by Aryal et al.[154] The immobilization Gd^{3+} ions on cell membranes boosts the r_1 relaxivity up to 19.0 mM^{-1} s^{-1} (3T MRI scanner).

To further optimize the contrast enhancement, the packing density of GdL per nanoparticle was varied by changing the amount of GdL input (50, 100, 200, and 400 µg GdL per 1 mg PLGA) during the paramagnetic polymeric core preparing step. Samples obtained from each formulation were concentrated or diluted to achieve the same final Gd^{3+} concentration ranging from 1.75, 3.5, 7, and 14 µg/mL. The magnetic properties of these different formulations of RBC-Gd-PLGA were investigated at a constant echo time of 10 ms while repetition time (TR) varying from 200 to 6000 ms. The T_1 relaxation times (**Table C.2**) were obtained and used to calculate r_1 relaxivity by plotting $1/T_1$ (s^{-1}) *vs* Gd^{3+} (mM) concentration (**Figure 5.4B**). As shown in **Figure 5.4C**, the r_1 relaxivity increased with the increasing of GdL per nanoparticle until it reached maximum r_1 value and then significantly dropped down when the amount of GdL per nanoparticle further increased.

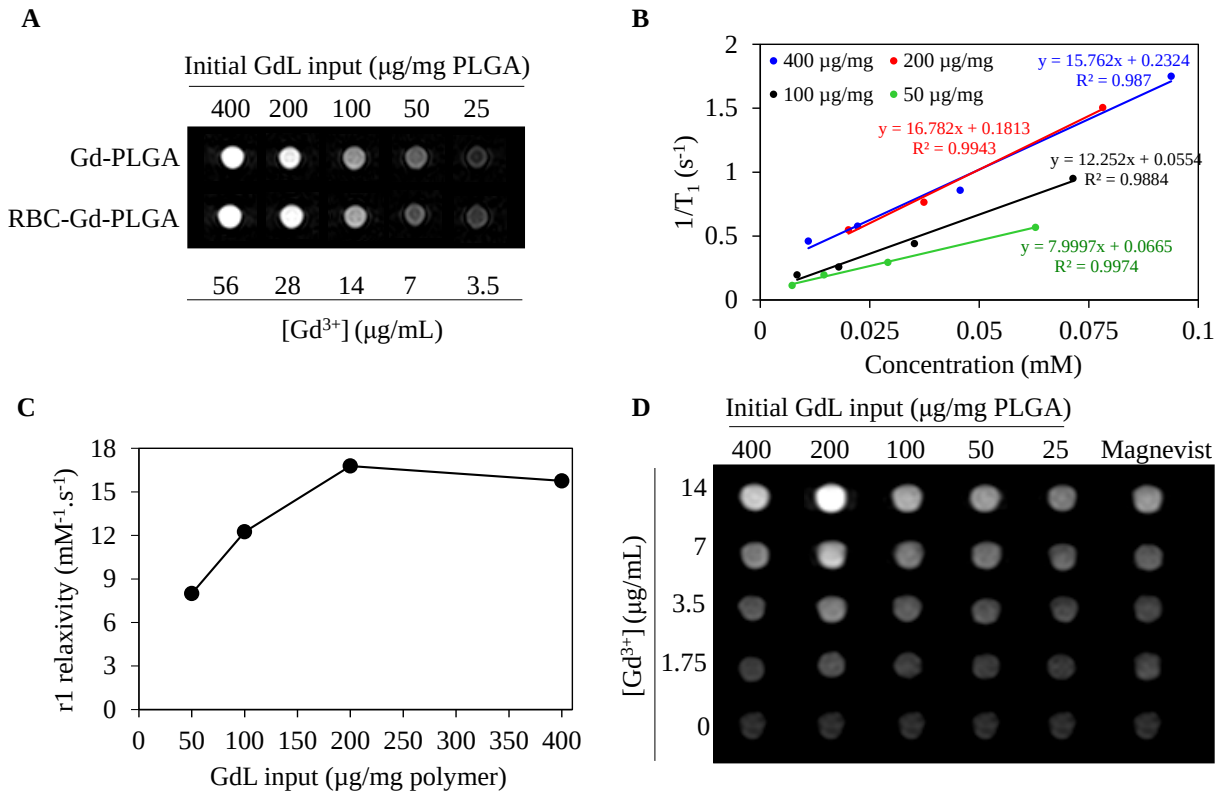

Figure 5.4 Magnetic properties of RBC-Gd-PLGA at 3T. (A) The phantom image represents the effect of RBC coating to the magnetic contrast enhancement of paramagnetic polymeric core. (B) T_1 longitudinal relaxation rate vs. Gd^{3+} concentration measured in a 3 T MRI system at 25 °C. (C) r_1 relaxation rate ($s^{-1}.mM^{-1}$) with different GdL packing density as a function of Gd^{3+} concentration. (D) T_1-Weighted MR images of RBC-Gd-PLGA aqueous suspensions with different concentrations and packing densities. The T_1-weighted MRI phantoms were taken using Fast Spin Echo Sequence at 3 T with TR = 400 ms, TE = 10 ms, FA = 90, FOV 256 × 256, and slice thickness = 2 mm.

Specifically, r_1 relaxivity increased from 7.9 $mM^{-1}.s^{-1}$ to 16.7 $mM^{-1}.s^{-1}$ when the amount of GdL per 1 mg PLGA increased from 50 µg to 200 µg. When the amount of GdL per 1 mg PLGA increased further to 400µg, the r_1 relaxivity dropped down to 15.7 $mM^{-1}.s^{-1}$. This phenomenon was also depicted by T_1-weighted images of different RBC-Gd-PLGA samples with equivalent Gd^{3+} concentrations as shown in **Figure 5.4D**; water and Magnevist were used as a control. The

increasing of r_1 at lower GdL density range (from 50 to 200 μg/mL) can be attributed to the distance-dependent enhancer between two GBCAs. When the distance between two GdLs gets closer, the flexibility of individual GdL reduces, hindering the local rotation of GBCA, as a consequent, the r_1 relaxivity increase. However, with the increasing of GdL input (beyond 200 μg GdL per 1 mg polymer), the GdL packing density on the surface of PNP are possibly jammed, limiting the access of H_2O molecules to the inner coordination sphere of Gd^{3+}. At this point, the contribution of local rotation is no longer a predominant factor instead of the number of inner coordination sphere H_2O molecules take over the mechanism of proton spin relaxivity. As a result, a significant reduction (or quenching effect) was observed when the amount of GdL per 1 mg polymer increase up to 400 μg. A similar relaxivity pattern was reported in a previous publication conducted by Marangoni et al, in which the Gd^{3+} ions were embedded in the silica layer of gold nanoshell particles.[156] Even though the GBCA in previous study is located in different compartments of the nanoconstruct compared to that of our study, the magnetic properties exhibited similar pattern in which the r_1 relaxivity increased from 8 to 14.6 $mM^{-1}.s^{-1}$, and then decrease to 5.3 $mM^{-1}.s^{-1}$ when the Gd(III) ion per nanoparticle varies from 0.7×10^5 to 2.5×10^5 and further increase to 8.2×10^5.[156]

Unlike other imaging modality, the contrast agent used in MRI does not directly emit a signal for detection but rather influencing the microenvironment surrounding it to shorten the relaxation time of proton spin. The magnitude of this effect strongly depends on chemical properties and structural complexity when the contrast agent is incorporated into a nanoparticulate system.[157,159,191] In the case of GBCA, the presence of paramagnetic ion will mainly increase the longitudinal relaxation rate ($1/T_1$) of water. According to Solomon-Bloembergen-Morgan (SBM) and outer sphere quantum mechanical theory, this enhancement of relaxivity is governed by

rotational correlation time, the distance between metal-water hydrogen, number of coordinated water molecules, the exchange rate of a water molecule from inner sphere to outer sphere, and water residence time. Therefore, by infusing GdL onto the surface of cell membrane coated PNP, we could simultaneously slow down rotational correlation time, shorten the distance between the paramagnetic ion and water hydrogen, prolong water residence time, and enrich the number of water molecules nearby metal ion. The combination of these effects together with an optimal packing density of Gd^{3+} generated by our nanoconstruct leads to the significant increase in observed r_1 relaxivity.

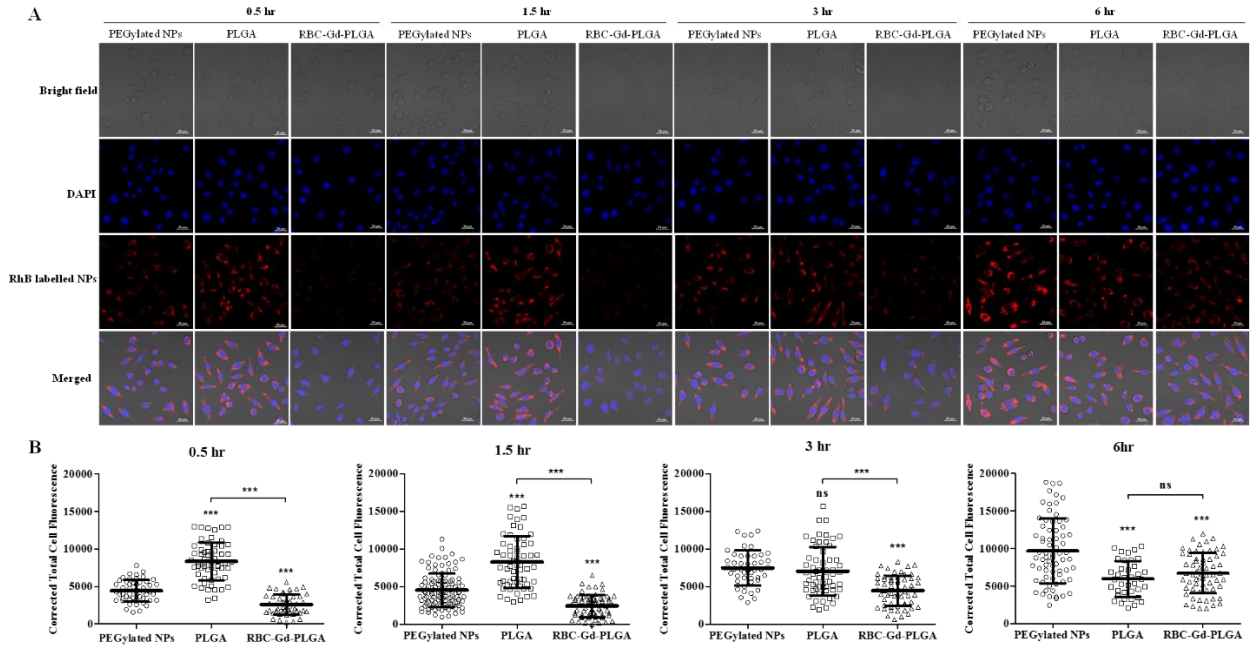

Figure 5.5. *In vitro* macrophage uptake study. (A) Representative confocal images showing comparative macrophages uptake of PEGylated, PLGA, and RBC-Gd-PLGA NPs after 0.5, 1.5, 3, and 6hr incubations. (B) Fluorescent quantification of cellular uptake by measuring corrected total cell fluorescent intensity of the cell population for each treatment and group. The data were statistically analyzed using one-way ANOVA with Turkey's multiple comparison post-test. (n = ~50 cells, mean ± sd). ns = not significant, *p < 0.05, ** p < 0.01, *** p < 0.001)

After getting the confirmation of magnetic relaxivity, we moved forward to study the interaction of RBC-Gd-PLGA with an immune cell. The capability of preserving CD47 from RBC, as evident in western blot, signifies the RBC-Gd-PLGA's ability for immune evasion by inhibiting phagocytosis via signal regulatory protein alpha (SIRPα) expressed by macrophages.[187,192,193] To confirm the ability to escape from macrophage phagocytosis of RBC-Gd-PLGA, we labeled the nanoparticle with RhB fluorescent dye and incubate with macrophage cell (J774.A1) over a period. We included RhB labeled PEGylated PLGA NPs, bare PLGA, and cell without treatment as positive and negative controls. After each incubation time, an excess amount of nanoparticles were washed out; cells were fixed and imaged under a confocal microscope. As can be seen in **Figure 5.5A**, PLGA NPs were immediately taken up by cells indicated by the high fluorescent signal at 30 min of incubation, whereas the PEGylated NPs and RBC-Gd-PLGA NPs showed minimal cellular uptake. The corrected total cell fluorescence revealed that at 30 min of incubation, the fluorescence intensity of cell treated with PLGA was two and four times higher than that of PEGylated NPs and RBC-Gd-PLGA NPs, respectively (**Figure 5.5B**). The high cell fluorescent signal at the early incubation time point of PLGA NPs is due to the lack of stability in serum condition (**Figure 5.1E**), whereby they immediately aggregate and trigger macrophage uptake. We also observed the decrease in fluorescent signal of cell treated PLGA NPs at a later time point which probably attributed to the degradation of PLGA NPs intracellularly (**Figure 5.5B**). Similarly, as the incubation time increase, PEGylated NPs started to lose its immune evasion ability leading to the significant increase in cellular uptake. At 6 hour time point, cell treated with PEGylated NPs exhibited the highest fluorescent signal intensity indicating the acceleration in macrophage phagocytosis. PEGylation has been routinely used to provide the stealth effect for nanoparticle in biological condition by reducing protein adsorption on nanocarrier surfaces. However, after a long time being

exposed to the biological condition, polyethylene glycol shield fails to prevent the adherent of proteins, making nanoparticle become visible to phagocytic cells and leading to the increase in cellular uptake over time as found in our result. A similar phenomenon was also observed *in vitro*, *in vivo* and even clinical trials.[194–196] On the other hand, the macrophage treated with RBC-Gd-PLGA showed the lowest fluorescent intensity with minimal change throughout the incubation time course, suggesting the superior stability and successful immune evasion of our nanomaterial.

When endogenous-derived materials such as cell membranes are used in *in vivo*, questions about the effect of these materials on the immune system are always of major concern. Among different immunogenicity stimulated by NPs, the release of pro-inflammatory cytokines play an important role owing to their ability to mediating the innate immune system to promote inflammation.[197] As RBC-Gd-PLGA was designed to serve as a blood pool contrast agent that can circulate for a long time in the body, the probability of RBC-Gd-PLGA to be in contact with blood pool cell is also increasing. Therefore, we carefully evaluated the immunomodulatory potential of our RBC-Gd-PLGA NPs by incubating with human peripheral blood monocyte cells, THP-1. The cytokines released in the cell culture supernatant were analyzed by magnetic human cytokine multiplex assays kit to quantify the amount of IL-1b, IL-6, and TNF-a cytokines **(Figure 5.6)**. These cytokines are often used to predict the immunomodulatory effects of nanomaterials and the possibility of inflammation-mediated toxicity.[197] After 24 hour of incubation, the detected amount of IL-1b, IL-6, and TNF-a cytokines released by THP-1 cell treated with RBC-Gd-PLGA were in the same level with control cell (without treatment) and control materials (RBC-M, PLGA, and GdL). On the other hand, there was a significantly high amount of cytokines released when the cell was treated with 5μg/mL lipopolysaccharides (LPS, positive control). The data indicate that the RBC-Gd-PLGA NPs does not interfere with the regular function of monocytes.

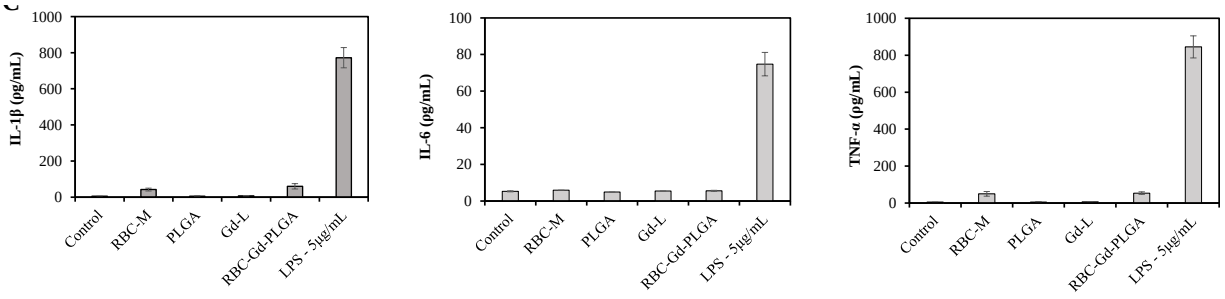

Figure 5.6. *In vitro* biocompatibility studies. Immunogenicity assessment of RBC-Gd-PLGA in THP-1 cells after 24 h incubation. The immunostimulant effect of RBC-Gd-PLGA was monitored by quantitative determination of pro-inflammatory cytokines (IL-1β, IL-6, and TNF-α) in THP-1 cells. Lipopolysaccharides (5μg/mL) were used as a positive control.

After validating the *in vitro* biocompatibility, the potential of NPs for *in vivo* imaging was assessed. We first started with pharmacokinetic and biodistribution using NU/NU mice to gain an understanding how RBC-Gd-PLGA moved and distributed throughout the body. Magnevist, a widely used gadolinium-based contrast agent, was used as a control. Taking the advantages of the natural absence of Gadolinium, we used Gd^{3+} in RBC-Gd-PLGA as a handle for analysis. As shown in **Figure 5.7A**, Magnevist was rapidly clear out from the blood with just 2% injected dose remained in the plasma after 2 hr post-injection. In contrast, with the biomimicry design, RBC-Gd-PLGA displayed a much longer circulation time. A two-compartmental model was applied to assess the pharmacokinetic parameters (**Table C.3**. RBC-Gd-PLGA exhibited a circulation half-life of 11.6 hr, which is much longer than that of commercially available contrast agents (**Table C.3**). The natural logarithmic scale with linear components for RBC-Gd-PLGA plasma concentration depicted by 2 main phases, a short distribution phase with $t_{1/2\alpha}$=3.12 h and a long elimination $t_{1/2\beta}$=11.6 h (**Figure 5.7A inset and Table C.3**). The volume distribution of RBC-Gd-PLGA at steady state (V_{dss}) was found to be 2.78 mL which is similar to the volume of blood in a mouse (2-3 mL). The similarity between V_{dss} and plasma volume suggest that the RBC-Gd-PLGA

mainly stays in the circulation system and poorly distributed in the tissue compartment. After 12 hr of circulation, RBC-Gd-PLGA gradually cleared out from the body with the clearance rate (Cl_{total}) of 0.21 mL per hour. With the extension in circulation time, the RBC-Gd-PLGA was still a presence in tissues after 24hr of injection (**Figure 5.7B**). RBC-Gd-PLGA mainly resided in liver and spleen along with minimal accumulation in lungs, bone and kidneys. Considering that liver and spleen are highly vascularized organs and the blood perfusion was not performed due to the restriction of IACUC protocol, the high amount of RBC-Gd-PLGA in liver and spleen is attributed for nanoparticle concentration presence in both tissue and blood vessels within the organ. In contrast to RBC-Gd-PLGA, Magnevist was completely cleared out from the body after 24 hours with less than 0.1% injected dose was found in most organs. The significant small amount of Magnevist in all tissue is also in agreement with our circulation half-life data in which the amount of Magnevist in blood was just 0.7% injected dose at 24 hrs time point. Importantly, the distribution data revealed that the kidney was the main organ for Magnevist to accumulate and eliminate whereas accumulation of RBC-Gd-PLGA in the kidney was significantly smaller than that of other organs. The high accumulation of Magnevist in kidney increases the risk of nephrogenic systemic fibrosis as it has been well documented when Gadolinium-based contrast agents are used in the clinic. Therefore, by constructing the gadolinium in a macrocyclic chelator and tuning the route of elimination from kidney to another excretion organ such as liver and spleen, we could avoid the side effect caused by the release of free Gd^{3+} in renal impaired patient thereby enhancing *in vivo* safety profile of RBC-Gd-PLGA.

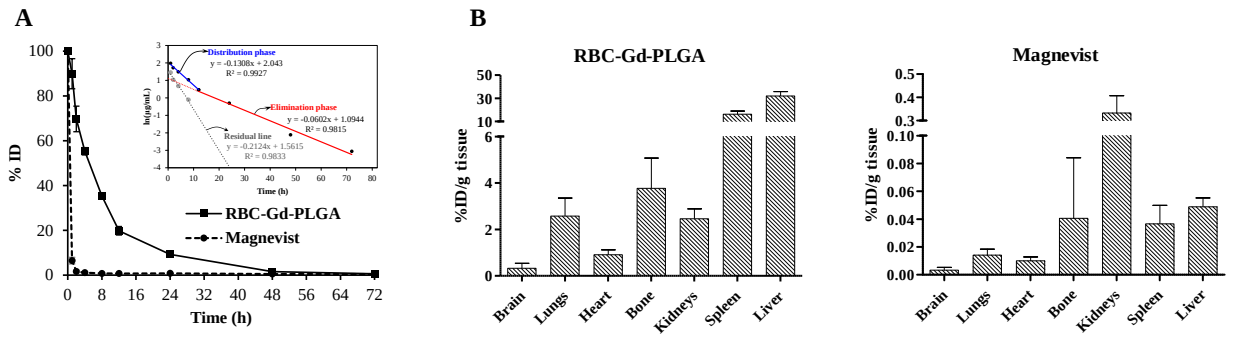

Figure 5.7 ***In vivo*** **pharmacokinetics and magnetic resonance imaging studies**. (A) Circulation half-life of RBC-Gd-PLGA and Magnevist in NU/NU mice over 72 h time (n=5). (B) Biodistribution profile of RBC-Gd-PLGA and Magnevist after single intravenous tail-vein injection in mice (n=4).

Finally, we conducted *in vivo* vascular imaging with RBC-Gd-PLGA using mice. RBC-Gd-PLGA 0.01 mmol Gd^{3+}/kg was injected intravenously via tail vein. Images were acquired precontrast and immediately at injection, 15 mins, and 30 mins post injection under a 3T clinical scanner. Similarly, another set of the mouse was dedicated for Magnevist contrast agent as control using the same experimental parameters. A side by side comparison of 3D reconstruction of images acquired at injection using maximum intensity projection with pre and post contrast subtraction is presented in **Figure 5.8A**. In the case of clinical contrast agent, Magnevist was quickly extravasate into surrounding tissue with most of the MR enhanced signal was localized throughout the kidney. Meanwhile, the RBC-GD-PLGA treated mouse exhibit the MR signal enhancement confined within abdominal aorta with the ability to delineate carotid arteries and superficial blood vessels of the head including anterior facial, posterior facial, transverse facial, and superficial temporal veins. Most importantly, the mouse treated RBC-Gd-PLGA exhibit a significantly higher contrast in heart and blood vessels when compared to that of Magnevist treated mouse while the Gd^{3+} injected a dose of RBC-Gd-PLGA is 2 times smaller than that of Magnevist. After 15 mins post injection, the MR signal of Magnevist at heart cannot be visualized anymore while MR signal at

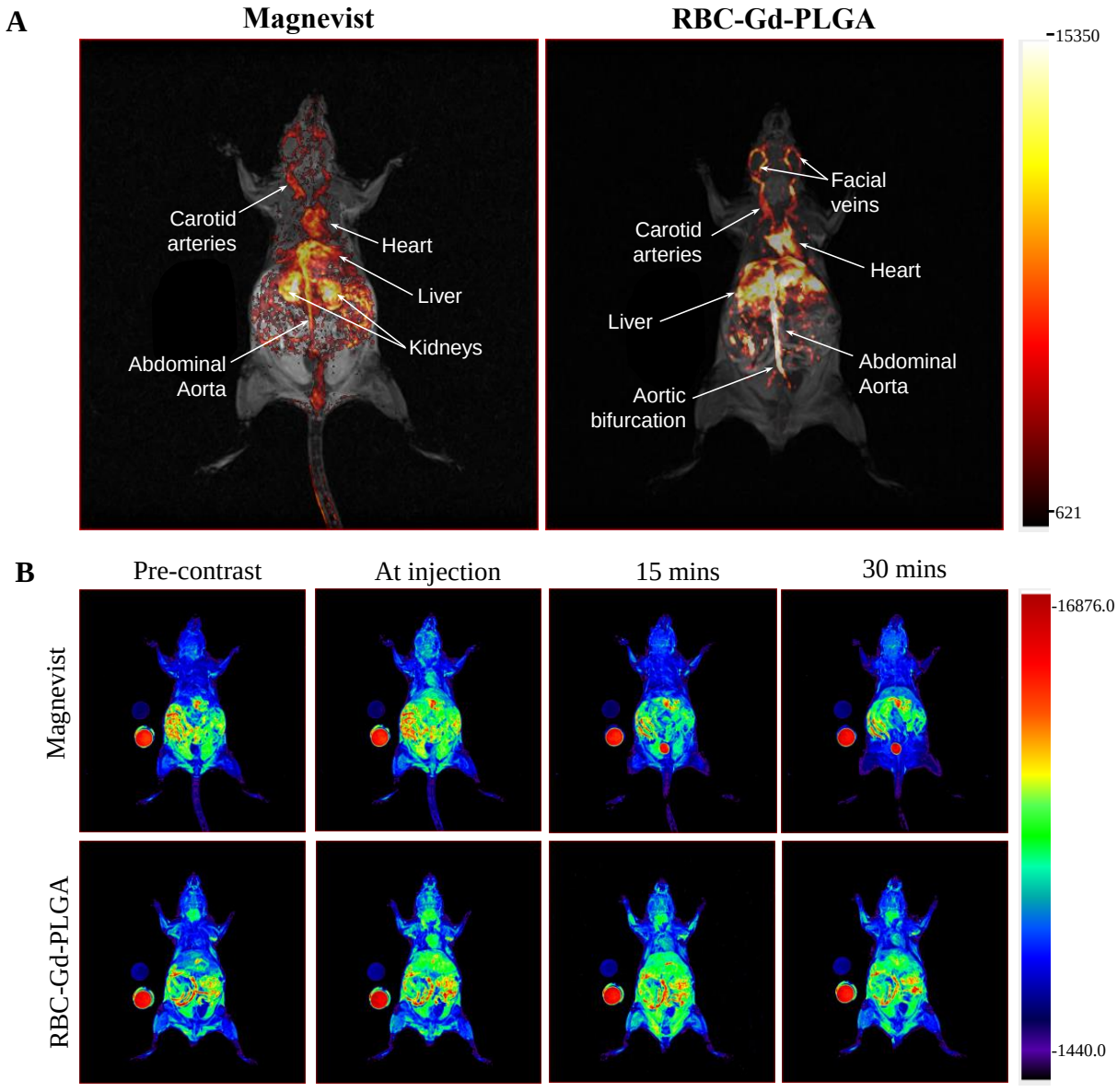

Figure 5.8 *In vivo* time-dependent T_1 weighted magnetic resonance image of mice after contrast agent injection. (A) 3D reconstruction of images acquired at injection using maximum intensity projection with pre and post contrast subtraction. (B) Time-dependent 3D reconstruction using maximum intensity projection without post contrast subtraction.

bladder significantly increases as evident in time-dependent 3D reconstruction using maximum intensity projection without post contrast subtraction presented in **Figure 5.8B**. As the circulating

time increase, the MR signal at the bladder of a mouse treated with Magnevist continues to increase while the MRI signal of the abdominal area completely disappeared. The time-dependent MR images obtained from a mouse injected with Magnevist further confirms the rapid renal accumulation and elimination of Magnevist. On the other hand, due to the ability to stay within the vasculature system, RBC-Gd-PLGA gives a distinguishable contrast between the blood vessel and surrounding tissue with the superior long-lasting contrast enhancement observed at heart.

5.4 Conclusion

In conclusion, a biomimetic gadolinium-based contrast agent nanoplatform was designed and fabricated to provide an excellent T_1 contrast enhancement by harnessing biocompatibility and *in vivo* longevity properties of red blood cell. The optimal packing density of GdL on the surface of nanoconstruct facilitate the relaxivity enhancement due to the confinement effect leading to the increase in local magnetization that water proton experience while maintaining available space for water assessment. Meanwhile, the proteins on the RBC membrane serve as water attraction points and provide a biological identity to ensure the survival of nanoplatforms in biological condition. Given the outstanding MRI performance, stability, biocompatibility, and prolong resident time, the use of RBC-Gd-PLGA allow particle tracking *in vivo* with a significant reduction in Gd^{3+} concentration, thereby providing a safer and more effective way for medical imaging. In addition, with the facile chemistry of polymer core could offer new opportunities for additional functionalization and drug loading, RBC-Gd-PLGA has potential applications as multifunctional agents for both diagnosis and treatment.

Chapter 6 - Summary and Future Outlook

Nanoparticle (NP)-based therapeutics involve the ability to engineer novel nanoscale platforms that can combine different functionalities in a single setting such as targeting, therapy, and diagnosis. In this dissertation, two approaches have been put forth, viz. chemistry and biology, to engineer different nanoconstructs with an ability to deliver drug and/or contrast agent to cancer.

In the chemistry, various conjugations including small molecules, ligand binding, and isolation and detection were used to assemble the component of the nanoparticulate system. Similarly, in the biological approach, characteristic properties of cell membranes such as signature protein markers were isolated and hybridized with synthetic components to engineer biomimetic nanoconstructs. Engineered biomimetic nanoconstructs were extensively studied and evaluated for their biological functions.

While the extensively researched synthetic nanoparticles in literature offer the opportunity for targeted drug delivery to cancer, the major challenges include rapid systemic elimination, protein opsonization, cellular degradation, toxicity, and non-specific uptake, limit the therapeutic effectiveness. Similarly, cell-based drug delivery systems, where the cell is used as a delivery vehicle, have also been studied widely with the hope that natural properties of the cell could be utilized for targeted drug delivery. However, the stress due to the payload in the vehicle cell and its survival due to toxic payloads remain major concerns. The aim of this dissertation is to take advantages of synthetic and biological systems to overcome their respective shortcomings to study the nanoparticle design parameters and drug delivery potentials.

The major advantage of the nanoconstructs presented herein are their abilities to stealth (nanoconstructs present in Chapter 2 to 5) and communicate with endogenous cells

(nanoconstructs present in Chapter 4 and 5). Due to the unique surface properties acquired from cells, for example, immune cells, diseased sites are recognized while preventing rapid elimination and nonspecific distribution of the active agent to a wide range of tissues and organs. While promising data were obtained indicating the opportunities of these nanoconstructs, challenges from design consideration to the practical application still require further investigations such as organ-specific toxicity, immunogenicity, and therapeutic effectiveness, which are out of the scope of this dissertation. Finally, broad vision contributing to the process of transforming the nanocarriers from "bench to bedside" should be taken into account from the beginning stage of the development, these include feasible manufacture processes, large-scale synthesis, and fulfillment of the clinical requirements.

References

1. Wagner, V., Dullaart, A., Bock, A.-K. & Zweck, A. The emerging nanomedicine landscape. *Nat. Biotechnol.* **24**, 1211–1217 (2006).
2. Ventola, C. L. Progress in Nanomedicine: Approved and Investigational Nanodrugs. *P T Peer-Rev. J. Formul. Manag.* **42**, 742–755 (2017).
3. Weissig, V., Pettinger, T. K. & Murdock, N. Nanopharmaceuticals (part 1): products on the market. *Int. J. Nanomedicine* **9**, 4357–4373 (2014).
4. Dilnawaz, F., Acharya, S. & Sahoo, S. K. Recent trends of nanomedicinal approaches in clinics. *Int. J. Pharm.* **538**, 263–278 (2018).
5. Shi, J., Kantoff, P. W., Wooster, R. & Farokhzad, O. C. Cancer nanomedicine: progress, challenges and opportunities. *Nat. Rev. Cancer* **17**, 20–37 (2017).
6. Gabizon, A. *et al.* Prolonged Circulation Time and Enhanced Accumulation in Malignant Exudates of Doxorubicin Encapsulated in Polyethylene-glycol Coated Liposomes. *Cancer Res.* **54**, 987–992 (1994).
7. Fang, J., Nakamura, H. & Maeda, H. The EPR effect: Unique features of tumor blood vessels for drug delivery, factors involved, and limitations and augmentation of the effect. *Adv. Drug Deliv. Rev.* **63**, 136–151 (2011).
8. Matsumura, Y. & Maeda, H. A new concept for macromolecular therapeutics in cancer chemotherapy: mechanism of tumoritropic accumulation of proteins and the antitumor agent smancs. *Cancer Res.* **46**, 6387–6392 (1986).
9. Smith-Bindman, R., Miglioretti, D. L. & Larson, E. B. Rising Use Of Diagnostic Medical Imaging In A Large Integrated Health System. *Health Aff. Proj. Hope* **27**, 1491–1502 (2008).
10. Medical Imaging Types and Modalities - Ultrasound, X-ray, CT, MRI. *Ausmed* (2018).

11. Nam, D., Barrack, R. L. & Potter, H. G. What Are the Advantages and Disadvantages of Imaging Modalities to Diagnose Wear-related Corrosion Problems? *Clin. Orthop.* **472**, 3665–3673 (2014).

12. Satterlee, A. B. & Huang, L. Current and Future Theranostic Applications of the Lipid-Calcium-Phosphate Nanoparticle Platform. *Theranostics* **6**, 918–929 (2016).

13. McMahon, S. E., Smith, T. O. & Hing, C. B. A systematic review of imaging modalities in the diagnosis of greater trochanteric pain syndrome. *Musculoskeletal Care* **10**, 232–239 (2012).

14. Thanh Nguyen, T. D., Pitchaimani, A., Ferrel, C., Thakkar, R. & Aryal, S. Nano-confinement-driven enhanced magnetic relaxivity of SPIONs for targeted tumor bioimaging. *Nanoscale* **10**, 284–294 (2018).

15. Khemtong, C. *et al.* In vivo off-resonance saturation magnetic resonance imaging of alphavbeta3-targeted superparamagnetic nanoparticles. *Cancer Res.* **69**, 1651–1658 (2009).

16. Sethi, R. *et al.* Enhanced MRI relaxivity of Gd3+-based contrast agents geometrically confined within porous nanoconstructs. *Contrast Media Mol. Imaging* **7**, 501–508 (2012).

17. Pitchaimani, A., Nguyen, T. D. T., Wang, H., Bossmann, S. H. & Aryal, S. Design and characterization of gadolinium infused theranostic liposomes. *RSC Adv.* **6**, 36898–36905 (2016).

18. Serda, R. E., Godin, B., Blanco, E., Chiappini, C. & Ferrari, M. MULTI-STAGE DELIVERY NANO-PARTICLE SYSTEMS FOR THERAPEUTIC APPLICATIONS. *Biochim. Biophys. Acta* **1810**, 317–329 (2011).

19. Blanco, E., Shen, H. & Ferrari, M. Principles of nanoparticle design for overcoming biological barriers to drug delivery. *Nat. Biotechnol.* **33**, 941–951 (2015).

20. Tenzer, S. *et al.* Rapid formation of plasma protein corona critically affects nanoparticle pathophysiology. *Nat. Nanotechnol.* **8**, 772–781 (2013).

21. Salvati, A. *et al.* Transferrin-functionalized nanoparticles lose their targeting capabilities when a biomolecule corona adsorbs on the surface. *Nat. Nanotechnol.* **8**, 137–143 (2013).

22. Kosaka, N., Ogawa, M., Choyke, P. L. & Kobayashi, H. Clinical implications of near-infrared fluorescence imaging in cancer. *Future Oncol. Lond. Engl.* **5**, 1501–1511 (2009).

23. Zhao, J. *et al.* Recent developments in multimodality fluorescence imaging probes. *Acta Pharm. Sin. B* **8**, 320–338 (2018).

24. Pan, D., Schmieder, A. H., Wickline, S. A. & Lanza, G. M. Manganese-based MRI contrast agents: past, present and future. *Tetrahedron* **67**, 8431–8444 (2011).

25. Ersoy, H. & Rybicki, F. J. Biochemical Safety Profiles of Gadolinium-Based Extracellular Contrast Agents and Nephrogenic Systemic Fibrosis. *J. Magn. Reson. Imaging JMRI* **26**, 1190–1197 (2007).

26. Vaquero, J. J. & Kinahan, P. Positron Emission Tomography: Current Challenges and Opportunities for Technological Advances in Clinical and Preclinical Imaging Systems. *Annu. Rev. Biomed. Eng.* **17**, 385–414 (2015).

27. Dai, Q. *et al.* Quantifying the Ligand-Coated Nanoparticle Delivery to Cancer Cells in Solid Tumors. *ACS Nano* **12**, 8423–8435 (2018).

28. Wilhelm, S. *et al.* Analysis of nanoparticle delivery to tumours. *Nat. Rev. Mater.* **1**, 16014 (2016).

29. Fukumura, D. & Jain, R. K. Tumor microenvironment abnormalities: Causes, consequences, and strategies to normalize. *J. Cell. Biochem.* **101**, 937–949 (2007).

30. Kamisawa, T., Wood, L. D., Itoi, T. & Takaori, K. Pancreatic cancer. *The Lancet* **388**, 73–85 (2016).

31. Kano, M. R. *et al.* Improvement of cancer-targeting therapy, using nanocarriers for intractable solid tumors by inhibition of TGF-β signaling. *Proc. Natl. Acad. Sci.* **104**, 3460–3465 (2007).

32. Cabral, H. *et al.* Accumulation of sub-100 nm polymeric micelles in poorly permeable tumours depends on size. *Nat. Nanotechnol.* **6**, 815–823 (2011).

33. Cairns, R., Papandreou, I. & Denko, N. Overcoming Physiologic Barriers to Cancer Treatment by Molecularly Targeting the Tumor Microenvironment. *Mol. Cancer Res.* **4**, 61–70 (2006).

34. Vander Heiden, M. G., Cantley, L. C. & Thompson, C. B. Understanding the Warburg Effect: The Metabolic Requirements of Cell Proliferation. *Science* **324**, 1029–1033 (2009).

35. Liberti, M. V. & Locasale, J. W. The Warburg Effect: How Does it Benefit Cancer Cells? *Trends Biochem. Sci.* **41**, 211–218 (2016).

36. Harris, A. L. Hypoxia--a key regulatory factor in tumour growth. *Nat. Rev. Cancer* **2**, 38–47 (2002).

37. Brown, J. M. & Wilson, W. R. Exploiting tumour hypoxia in cancer treatment. *Nat. Rev. Cancer* **4**, 437–447 (2004).

38. Brown, J. M. & Giaccia, A. J. The unique physiology of solid tumors: opportunities (and problems) for cancer therapy. *Cancer Res.* **58**, 1408–1416 (1998).

39. Vaupel, P., Mayer, A. & Höckel, M. Tumor hypoxia and malignant progression. *Methods Enzymol.* **381**, 335–354 (2004).

40. Vaupel, P., Höckel, M. & Mayer, A. Detection and characterization of tumor hypoxia using pO2 histography. *Antioxid. Redox Signal.* **9**, 1221–1235 (2007).

41. Semenza, G. L. The hypoxic tumor microenvironment: A driving force for breast cancer progression. *Biochim. Biophys. Acta* **1863**, 382–391 (2016).

42. Gilkes, D. M. & Semenza, G. L. Role of hypoxia-inducible factors in breast cancer metastasis. *Future Oncol. Lond. Engl.* **9**, 1623–1636 (2013).

43. Adjei, I. M., Sharma, B. & Labhasetwar, V. Nanoparticles: Cellular Uptake and Cytotoxicity. in *Nanomaterial: Impacts on Cell Biology and Medicine* (eds. Capco, D. G. & Chen, Y.) 73–91 (Springer Netherlands, 2014). doi:10.1007/978-94-017-8739-0_5

44. Huotari, J. & Helenius, A. Endosome maturation. *EMBO J.* **30**, 3481–3500 (2011).

45. Siegel, R. L., Miller, K. D. & Jemal, A. Cancer statistics, 2016. *CA. Cancer J. Clin.* **66**, 7–30 (2016).

46. Coleman, R. E. Clinical Features of Metastatic Bone Disease and Risk of Skeletal Morbidity. *Am. Assoc. Cancer Res.* **12**, 6243s–6249s (2006).

47. Diel, I. J. Prognostic factors for skeletal relapse in breast cancer. *Cancer Treat. Rev.* **27**, 153–157; discussion 159-164 (2001).

48. Mathot, L. & Stenninger, J. Behavior of seeds and soil in the mechanism of metastasis: A deeper understanding. *Cancer Sci.* **103**, 626–631 (2012).

49. Paget, S. The distribution of secondary growths in cancer of the breast. 1889. *Cancer Metastasis Rev.* **8**, 98–101 (1989).

50. Weilbaecher, K. N., Guise, T. A. & McCauley, L. K. Cancer to bone: a fatal attraction. *Nat. Rev. Cancer* **11**, 411–425 (2011).

51. Mundy, G. R. Metastasis to bone: causes, consequences and therapeutic opportunities. *Nat. Rev. Cancer* **2**, 584–593 (2002).

52. Zheng, Y., Zhou, H., Dunstan, C. R., Sutherland, R. L. & Seibel, M. J. The role of the bone microenvironment in skeletal metastasis. *J. Bone Oncol.* **2**, 47–57 (2013).

53. Boulenc, X. *et al.* Importance of the paracellular pathway for the transport of a new bisphosphonate using the human CACO-2 monolayers model. *Biochem. Pharmacol.* **46**, 1591–1600 (1993).

54. Hirabayashi, H. & Fujisaki, J. Bone-specific drug delivery systems: approaches via chemical modification of bone-seeking agents. *Clin. Pharmacokinet.* **42**, 1319–1330 (2003).

55. Lin, J. H., Chen, I. W. & Duggan, D. E. Effects of dose, sex, and age on the disposition of alendronate, a potent antiosteolytic bisphosphonate, in rats. *Drug Metab. Dispos. Biol. Fate Chem.* **20**, 473–478 (1992).

56. Lin, J. H., Duggan, D. E., Chen, I. W. & Ellsworth, R. L. Physiological disposition of alendronate, a potent anti-osteolytic bisphosphonate, in laboratory animals. *Drug Metab. Dispos. Biol. Fate Chem.* **19**, 926–932 (1991).

57. Ebetino, F. H. *et al.* The relationship between the chemistry and biological activity of the bisphosphonates. *Bone* **49**, 20–33 (2011).

58. Chen, H. *et al.* Alendronate-Conjugated Amphiphilic Hyperbranched Polymer Based on Boltorn H40 and Poly(ethylene glycol) for Bone-Targeted Drug Delivery. *Bioconjug. Chem.* **23**, 1915–1924 (2012).

59. Uludag, H. Bisphosphonates as a foundation of drug delivery to bone. *Curr. Pharm. Des.* **8**, 1929–1944 (2002).

60. Clementi, C., Miller, K., Mero, A., Satchi-Fainaro, R. & Pasut, G. Dendritic poly(ethylene glycol) bearing paclitaxel and alendronate for targeting bone neoplasms. *Mol. Pharm.* **8**, 1063–1072 (2011).

61. Swami, A. *et al.* Engineered nanomedicine for myeloma and bone microenvironment targeting. *Proc. Natl. Acad. Sci. U. S. A.* **111**, 10287–10292 (2014).

62. Ye, W. *et al.* Doxorubicin-poly (ethylene glycol)-alendronate self-assembled micelles for targeted therapy of bone metastatic cancer. *Sci. Rep.* **5**, 14614 (2015).

63. Zhang, S., Gangal, G. & Uludağ, H. 'Magic bullets' for bone diseases: progress in rational design of bone-seeking medicinal agents. *Chem. Soc. Rev.* **36**, 507–531 (2007).

64. Verhoef, J. J. F., Carpenter, J. F., Anchordoquy, T. J. & Schellekens, H. Potential induction of anti-PEG antibodies and complement activation toward PEGylated therapeutics. *Drug Discov. Today* **19**, 1945–1952 (2014).

65. Henry, C. E. *et al.* Anti-PEG antibodies alter the mobility and biodistribution of densely PEGylated nanoparticles in mucus. *Acta Biomater.* **43**, 61–70 (2016).

66. Zhang, P., Sun, F., Liu, S. & Jiang, S. Anti-PEG antibodies in the clinic: Current issues and beyond PEGylation. *J. Control. Release Off. J. Control. Release Soc.* (2016). doi:10.1016/j.jconrel.2016.06.040

67. Yang, Q. & Lai, S. K. Anti-PEG immunity: emergence, characteristics, and unaddressed questions. *Wiley Interdiscip. Rev. Nanomed. Nanobiotechnol.* **7**, 655–677 (2015).

68. Garay, R. P., El-Gewely, R., Armstrong, J. K., Garratty, G. & Richette, P. Antibodies against polyethylene glycol in healthy subjects and in patients treated with PEG-conjugated agents. *Expert Opin. Drug Deliv.* **9**, 1319–1323 (2012).

69. Hu, C.-M. J. *et al.* Erythrocyte membrane-camouflaged polymeric nanoparticles as a biomimetic delivery platform. *Proc. Natl. Acad. Sci. U. S. A.* **108**, 10980–10985 (2011).

70. Aryal, S. *et al.* Erythrocyte membrane-cloaked polymeric nanoparticles for controlled drug loading and release. *Nanomed.* **8**, 1271–1280 (2013).

71. Nguyen, T. D. T., Pitchaimani, A., Koirala, M. B., Muhammad, F. & Aryal, S. Engineered biomimetic nanoabsorbent for cellular detoxification of chemotherapeutics. *RSC Adv.* **6**, 33003–33008 (2016).

72. Saari, A.-L. *et al.* Systematic study of the physicochemical properties of a homologous series of aminobisphosphonates. *Mol. Basel Switz.* **17**, 10928–10945 (2012).

73. Ryu, T.-K. *et al.* Bone-targeted delivery of nanodiamond-based drug carriers conjugated with alendronate for potential osteoporosis treatment. *J. Controlled Release* **232**, 152–160 (2016).

74. Morelli, S. *et al.* Protein phosphatases: possible bisphosphonate binding sites mediating stimulation of osteoblast proliferation. *Arch. Biochem. Biophys.* **507**, 248–253 (2011).

75. Yang, D., Okamura, H., Morimoto, H., Teramachi, J. & Haneji, T. Protein phosphatase 2A Cα regulates proliferation, migration, and metastasis of osteosarcoma cells. *Lab. Invest.* **96**, 1050–1062 (2016).

76. Toledo, S. R. C. *et al.* Bone deposition, bone resorption, and osteosarcoma. *J. Orthop. Res.* **28**, 1142–1148 (2010).

77. Akiyama, T., Dass, C. R. & Choong, P. F. M. Novel therapeutic strategy for osteosarcoma targeting osteoclast differentiation, bone-resorbing activity, and apoptosis pathway. *Mol. Cancer Ther.* **7**, 3461–3469 (2008).

78. Gizzatov, A. *et al.* Hierarchically Structured Magnetic Nanoconstructs with Enhanced Relaxivity and Cooperative Tumor Accumulation. *Adv. Funct. Mater.* **24**, 4584–4594 (2014).

79. Aryal, S. *et al.* Positron emitting magnetic nanoconstructs for PET/MR imaging. *Small* **10**, 2688–2696 (2014).

80. Cervadoro, A. *et al.* Synthesis of Multifunctional Magnetic NanoFlakes for Magnetic Resonance Imaging, Hyperthermia, and Targeting. *ACS Appl. Mater. Interfaces* **6**, 12939–12946 (2014).

81. Aryal, S. *et al.* Engineered magnetic hybrid nanoparticles with enhanced relaxivity for tumor imaging. *Biomaterials* **34**, 7725–7732 (2013).

82. Yan, G.-P., Robinson, L. & Hogg, P. Magnetic resonance imaging contrast agents: Overview and perspectives. *Radiography* **13**, e5–e19 (2007).

83. Imai, Y. *et al.* Superparamagnetic iron oxide–enhanced magnetic resonance images of hepatocellular carcinoma: Correlation with histological grading. *Hepatology* **32**, 205–212 (2000).

84. Harisinghani, M. G. & Weissleder, R. Sensitive, Noninvasive Detection of Lymph Node Metastases. *PLoS Med.* **1**, (2004).

85. Ichikawa, T. *et al.* Perfusion MR imaging with a superparamagnetic iron oxide using T2-weighted and susceptibility-sensitive echoplanar sequences: evaluation of tumor vascularity in hepatocellular carcinoma. *Am. J. Roentgenol.* **173**, 207–213 (1999).

86. Reimer, P. & Balzer, T. Ferucarbotran (Resovist): a new clinically approved RES-specific contrast agent for contrast-enhanced MRI of the liver: properties, clinical development, and applications. *Eur. Radiol.* **13**, 1266–1276 (2003).

87. Senéterre, E. *et al.* Detection of hepatic metastases: ferumoxides-enhanced MR imaging versus unenhanced MR imaging and CT during arterial portography. *Radiology* **200**, 785–792 (1996).

88. Imai, Y. *et al.* Hypervascular hepatocellular carcinoma: Combined dynamic MDCT and SPIO-enhanced MRI versus combined CTHA and CTAP. *Hepatol. Res.* **38**, 147–158 (2008).

89. Caravan, P., Ellison, J. J., McMurry, T. J. & Lauffer, R. B. Gadolinium(III) Chelates as MRI Contrast Agents: Structure, Dynamics, and Applications. *Chem. Rev.* **99**, 2293–2352 (1999).

90. Pitchaimani, A. *et al.* Gd3 + Tethered Gold Nanorods for Combined Magnetic Resonance Imaging and Photo-Thermal Therapy. *J. Biomed. Nanotechnol.* **13**, 417–426 (2017).

91. Kurtkoti, J., Snow, T. & Hiremagalur, B. Gadolinium and nephrogenic systemic fibrosis: Association or causation (Review Article). *Nephrology* **13**, 235–241 (2008).

92. Perazella, M. A. Nephrogenic Systemic Fibrosis, Kidney Disease, and Gadolinium: Is There a Link? *Clin. J. Am. Soc. Nephrol.* **2**, 200–202 (2007).

93. Kribben, A. *et al.* Nephrogenic Systemic Fibrosis. *J. Am. Coll. Cardiol.* **53**, 1621–1628 (2009).

94. Myrissa, A. *et al.* Gadolinium accumulation in organs of Sprague–Dawley® rats after implantation of a biodegradable magnesium-gadolinium alloy. *Acta Biomater.* **48**, 521–529 (2017).

95. Rogosnitzky, M. & Branch, S. Gadolinium-based contrast agent toxicity: a review of known and proposed mechanisms. *BioMetals* **29**, 365–376 (2016).

96. McDonald, R. J. *et al.* Intracranial Gadolinium Deposition after Contrast-enhanced MR Imaging. *Radiology* **275**, 772–782 (2015).

97. Research, C. for D. E. and. Drug Safety and Availability - FDA Drug Safety Communication: FDA evaluating the risk of brain deposits with repeated use of gadolinium-based contrast agents for magnetic resonance imaging (MRI). Available at: https://www.fda.gov/Drugs/DrugSafety/ucm455386. (Accessed: 16th August 2017)

98. Mürbe, J., Rechtenbach, A. & Töpfer, J. Synthesis and physical characterization of magnetite nanoparticles for biomedical applications. *Mater. Chem. Phys.* **110**, 426–433 (2008).

99. Lu, A.-H., Salabas, E. L. & Schüth, F. Magnetic Nanoparticles: Synthesis, Protection, Functionalization, and Application. *Angew. Chem. Int. Ed.* **46**, 1222–1244 (2007).

100. Cheng, F.-Y. *et al.* Characterization of aqueous dispersions of Fe3O4 nanoparticles and their biomedical applications. *Biomaterials* **26**, 729–738 (2005).

101. Drake, M. T., Clarke, B. L. & Khosla, S. Bisphosphonates: Mechanism of Action and Role in Clinical Practice. *Mayo Clin. Proc. Mayo Clin.* **83**, 1032–1045 (2008).

102. Boskey, A. L. Bone composition: relationship to bone fragility and antiosteoporotic drug effects. *BoneKEy Rep.* **2**, 447 (2013).

103. Rey, C., Combes, C., Drouet, C. & Glimcher, M. J. Bone mineral: update on chemical composition and structure. *Osteoporos. Int. J. Establ. Result Coop. Eur. Found. Osteoporos. Natl. Osteoporos. Found. USA* **20**, 1013–1021 (2009).

104. Burr, D. B. & Akkus, O. Chapter 1 - Bone Morphology and Organization. in *Basic and Applied Bone Biology* 3–25 (Academic Press, 2014). doi:10.1016/B978-0-12-416015-6.00001-0

105. Nguyen, T. D. T., Pitchaimani, A. & Aryal, S. Engineered Nanomedicine with Alendronic Acid Corona Improves Targeting to Osteosarcoma. *Sci. Rep.* **6**, (2016).

106. Meloun, M., Ferenčíková, Z., Netolická, L. & Pekárek, T. Thermodynamic Dissociation Constants of Alendronate and Ibandronate by Regression Analysis of Potentiometric Data. *J. Chem. Eng. Data* **56**, 3848–3854 (2011).

107. Israelachvili, J. & Wennerström, H. Role of hydration and water structure in biological and colloidal interactions. *Nature* **379**, 219–225 (1996).

108. Chen, Y.-C., Sosnoski, D. M. & Mastro, A. M. Breast cancer metastasis to the bone: mechanisms of bone loss. *Breast Cancer Res. BCR* **12**, 215 (2010).

109. Thamake, S. I., Raut, S. L., Gryczynski, Z., Ranjan, A. P. & Vishwanatha, J. K. Alendronate coated poly-lactic-co-glycolic acid (PLGA) nanoparticles for active targeting of metastatic breast cancer. *Biomaterials* **33**, 7164–7173 (2012).

110. Liu, P. *et al.* Development of Alendronate-conjugated Poly (lactic-co-glycolic acid)-Dextran Nanoparticles for Active Targeting of Cisplatin in Osteosarcoma. *Sci. Rep.* **5**, 17387 (2015).

111. Smith, C. E. *et al.* Hydrophilic packaging of iron oxide nanoclusters for highly sensitive imaging. *Biomaterials* **69**, 184–190 (2015).

112. Lin, Y. *et al.* Ultra-high relaxivity iron oxide nanoparticles confined in polymer nanospheres for tumor MR imaging. *J. Mater. Chem. B* **3**, 5702–5710 (2015).

113. Ragheb, R. R. T. *et al.* Induced clustered nanoconfinement of superparamagnetic iron oxide in biodegradable nanoparticles enhances transverse relaxivity for targeted theranostics. *Magn. Reson. Med.* **70**, 1748–1760 (2013).

114. Paquet, C. *et al.* Clusters of Superparamagnetic Iron Oxide Nanoparticles Encapsulated in a Hydrogel: A Particle Architecture Generating a Synergistic Enhancement of the T2 Relaxation. *ACS Nano* **5**, 3104–3112 (2011).

115. Ray, S. S. *et al.* Self-diffusion of water in thermoreversible gels near volume transition. *Chem. Eng. Sci.* **53**, 869–877 (1998).

116. Tong, S., Hou, S., Zheng, Z., Zhou, J. & Bao, G. Coating optimization of superparamagnetic iron oxide nanoparticles for high T2 relaxivity. *Nano Lett.* **10**, 4607–4613 (2010).

117. A. Keasberry, N. *et al.* Tuning the relaxation rates of dual-mode T 1 / T 2 nanoparticle contrast agents: a study into the ideal system. *Nanoscale* **7**, 16119–16128 (2015).

118. Lorenzato, C. *et al.* MRI contrast variation of thermosensitive magnetoliposomes triggered by focused ultrasound: a tool for image-guided local drug delivery. *Contrast Media Mol. Imaging* **8**, 185–192 (2013).

119. Mikhaylov, G. *et al.* Ferri-liposomes as an MRI-visible drug-delivery system for targeting tumours and their microenvironment. *Nat. Nanotechnol.* **6**, 594–602 (2011).

120. Choo, E. S. G., Tang, X., Sheng, Y., Shuter, B. & Xue, J. Controlled loading of superparamagnetic nanoparticles in fluorescent nanogels as effective T2-weighted MRI contrast agents. *J. Mater. Chem.* **21**, 2310–2319 (2011).

121. Wang, Y. X., Hussain, S. M. & Krestin, G. P. Superparamagnetic iron oxide contrast agents: physicochemical characteristics and applications in MR imaging. *Eur. Radiol.* **11**, 2319–2331 (2001).

122. Sugita, M. & Tenjin, Y. [The application of confocal laser scanning microscopy (CLSM) in cell biology]. *Nihon Rinsho Jpn. J. Clin. Med.* **51**, 1108–1113 (1993).

123. Feridex - FDA prescribing information, side effects and uses. *Drugs.com* Available at: https://www.drugs.com/pro/feridex.html. (Accessed: 4th September 2017)

124. Fang, R. H. *et al.* Cancer Cell Membrane-Coated Nanoparticles for Anticancer Vaccination and Drug Delivery. *Nano Lett.* **14**, 2181–2188 (2014).

125. Aryal, S. *et al.* Membrane Fusion-Mediated Gold Nanoplating of Red Blood Cell: A Bioengineered CT-Contrast Agent. *ACS Biomater. Sci. Eng.* **3**, 36–41 (2017).

126. Cao, H. *et al.* Liposomes Coated with Isolated Macrophage Membrane Can Target Lung Metastasis of Breast Cancer. *ACS Nano* **10**, 7738–7748 (2016).

127. Parodi, A. *et al.* Synthetic nanoparticles functionalized with biomimetic leukocyte membranes possess cell-like functions. *Nat. Nanotechnol.* **8**, 61–68 (2013).

128. Mitchell, M. J., Wayne, E., Rana, K., Schaffer, C. B. & King, M. R. TRAIL-coated leukocytes that kill cancer cells in the circulation. *Proc. Natl. Acad. Sci.* **111**, 930–935 (2014).

129. Kang, T. *et al.* Nanoparticles Coated with Neutrophil Membranes Can Effectively Treat Cancer Metastasis. *ACS Nano* **11**, 1397–1411 (2017).

130. Guo, Y. *et al.* Erythrocyte Membrane-Enveloped Polymeric Nanoparticles as Nanovaccine for Induction of Antitumor Immunity against Melanoma. *ACS Nano* **9**, 6918–6933 (2015).

131. Li, J. *et al.* Targeted drug delivery to circulating tumor cells via platelet membrane-functionalized particles. *Biomaterials* **76**, 52–65 (2016).

132. Suck, G., Linn, Y. C. & Tonn, T. Natural Killer Cells for Therapy of Leukemia. *Transfus. Med. Hemotherapy* **43**, 89–95 (2016).

133. Langers, I., Renoux, V. M., Thiry, M., Delvenne, P. & Jacobs, N. Natural killer cells: role in local tumor growth and metastasis. *Biol. Targets Ther.* **6**, 73–82 (2012).

134. Knorr, D. A., Bachanova, V., Verneris, M. R. & Miller, J. S. Clinical utility of natural killer cells in cancer therapy and transplantation. *Semin. Immunol.* **26**, 161–172 (2014).

135. Waldhauer, I. & Steinle, A. NK cells and cancer immunosurveillance. *Oncogene* **27**, 5932–5943 (2008).

136. Hanna, N. Role of natural killer cells in control of cancer metastasis. *Cancer Metastasis Rev.* **1**, 45–64 (1982).

137. Pitchaimani, A., Nguyen, T. D. T. & Aryal, S. Natural killer cell membrane infused biomimetic liposomes for targeted tumor therapy. *Biomaterials* **160**, 124–137 (2018).

138. Dahlberg, C. I. M., Sarhan, D., Chrobok, M., Duru, A. D. & Alici, E. Natural Killer Cell-Based Therapies Targeting Cancer: Possible Strategies to Gain and Sustain Anti-Tumor Activity. *Front. Immunol.* **6**, 605 (2015).

139. Tonn, T. *et al.* Treatment of patients with advanced cancer with the natural killer cell line NK-92. *Cytotherapy* **15**, 1563–1570 (2013).

140. Tsartsalis, D. *et al.* In Vitro Exposure of NK-92 Cells to Serum from Patients with Non-small Cell Lung Cancer Impairs Their Cytotoxicity. *Anticancer Res.* **35**, 1543–1548 (2015).

141. Suck, G. *et al.* NK-92: an 'off-the-shelf therapeutic' for adoptive natural killer cell-based cancer immunotherapy. *Cancer Immunol. Immunother. CII* **65**, 485–492 (2016).

142. Romanski, A. *et al.* CD19-CAR engineered NK-92 cells are sufficient to overcome NK cell resistance in B-cell malignancies. *J. Cell. Mol. Med.* **20**, 1287–1294 (2016).

143. Zhou, Z. & Lu, Z.-R. Gadolinium-based contrast agents for magnetic resonance cancer imaging. *Wiley Interdiscip. Rev. Nanomed. Nanobiotechnol.* **5**, 1–18 (2013).

144. Tagami, T. *et al.* MRI monitoring of intratumoral drug delivery and prediction of the therapeutic effect with a multifunctional thermosensitive liposome. *Biomaterials* **32**, 6570–6578 (2011).

145. Ghaghada, K., Hawley, C., Kawaji, K., Annapragada, A. & Mukundan, S. T1 relaxivity of core-encapsulated gadolinium liposomal contrast agents--effect of liposome size and internal gadolinium concentration. *Acad. Radiol.* **15**, 1259–1263 (2008).

146. de Smet, M., Heijman, E., Langereis, S., Hijnen, N. M. & Grüll, H. Magnetic resonance imaging of high intensity focused ultrasound mediated drug delivery from temperature-sensitive liposomes: an in vivo proof-of-concept study. *J. Control. Release Off. J. Control. Release Soc.* **150**, 102–110 (2011).

147. Nguyen, T. D. T., Pitchaimani, A. & Aryal, S. Engineered Nanomedicine with Alendronic Acid Corona Improves Targeting to Osteosarcoma. *Sci. Rep.* **6**, srep36707 (2016).

148. Pitchaimani, A. *et al.* Gd^{3+} Tethered Gold Nanorods for Combined Magnetic Resonance Imaging and Photo-Thermal Therapy. *J. Biomed. Nanotechnol.* **13**, 417–426 (2017).

149. Pitchaimani, A., Nguyen, T. D. T., Koirala, M., Zhang, Y. & Aryal, S. Impact of cell adhesion and migration on nanoparticle uptake and cellular toxicity. *Toxicol. In Vitro* **43**, 29–39 (2017).

150. Riviere, J. E. *et al.* Modeling gold nanoparticle biodistribution after arterial infusion into perfused tissue: effects of surface coating, size and protein corona. *Nanotoxicology* 1–20 (2018). doi:10.1080/17435390.2018.1476986

151. Moghadas, S. M. & Jaberi-Douraki, M. *Mathematical Modelling: A Graduate Textbook*. (John Wiley & Sons, 2018).

152. Sidhu, P. K. *et al.* Comparative pharmacokinetics of oxytetracycline in tilapia (Oreochromis spp.) maintained at three different salinities. *Aquaculture* **495**, 675–681 (2018).

153. Soraya Dhillon, A. K. *Clinical Pharmacokinetics*.

154. Aryal, S. *et al.* Paramagnetic Gd3+ labeled red blood cells for magnetic resonance angiography. *Biomaterials* **98**, 163–170 (2016).

155. Maki, G., Klingemann, H. G., Martinson, J. A. & Tam, Y. K. Factors regulating the cytotoxic activity of the human natural killer cell line, NK-92. *J. Hematother. Stem Cell Res.* **10**, 369–383 (2001).

156. Marangoni, V. S. *et al.* Enhancing T1 magnetic resonance imaging contrast with internalized gadolinium(III) in a multilayer nanoparticle. *Proc. Natl. Acad. Sci. U. S. A.* **114**, 6960–6965 (2017).

157. Wahsner, J., Gale, E. M., Rodríguez-Rodríguez, A. & Caravan, P. Chemistry of MRI Contrast Agents: Current Challenges and New Frontiers. *Chem. Rev.* (2018). doi:10.1021/acs.chemrev.8b00363

158. Magnetic resonance imaging (MRI) exams. Available at: https://www.oecd-ilibrary.org/social-issues-migration-health/magnetic-resonance-imaging-mri-exams/indicator/english_1d89353f-en. (Accessed: 21st January 2019)

159. Zhou, Z., Yang, L., Gao, J. & Chen, X. Structure–Relaxivity Relationships of Magnetic Nanoparticles for Magnetic Resonance Imaging. *Adv. Mater.* **0**, 1804567

160. Edelman, R. R., Hesselink, J. & Zlatkin, M. *Clinical Magnetic Resonance Imaging: 3-Volume Set*. (Saunders, 2005).

161. Lauffer, R. B. Paramagnetic metal complexes as water proton relaxation agents for NMR imaging: theory and design. *Chem. Rev.* **87**, 901–927 (1987).

162. Botta, M. & Tei, L. Relaxivity Enhancement in Macromolecular and Nanosized GdIII-Based MRI Contrast Agents. *Eur. J. Inorg. Chem.* **2012**, 1945–1960 (2012).

163. Greenberg, S. A. Zinc transmetallation and gadolinium retention after MR imaging: case report. *Radiology* **257**, 670–673 (2010).

164. Penfield, J. G. & Reilly, R. F. What nephrologists need to know about gadolinium. *Nat. Rev. Nephrol.* **3**, 654–668 (2007).

165. Morcos, S. K. Extracellular gadolinium contrast agents: differences in stability. *Eur. J. Radiol.* **66**, 175–179 (2008).

166. Wu, B. *et al.* Gadolinium-chelate functionalized bismuth nanotheranostic agent for in vivo MRI/CT/PAI imaging-guided photothermal cancer therapy. *Biomaterials* **159**, 37–47 (2018).

167. Yoo, S. P. *et al.* Gadolinium-Functionalized Peptide Amphiphile Micelles for Multimodal Imaging of Atherosclerotic Lesions. *ACS Omega* **1**, 996–1003 (2016).

168. Ma, J. *et al.* Deposition of gadolinium onto the shell structure of micelles for integrated magnetic resonance imaging and robust drug delivery systems. *J. Mater. Chem. B* **4**, 6094–6102 (2016).

169. Babič, A. *et al.* MRI micelles self-assembled from synthetic gadolinium-based nano building blocks. *Chem. Commun.* **55**, 945–948 (2019).

170. Longmire, M., Choyke, P. L. & Kobayashi, H. Dendrimer-Based Contrast Agents for Molecular Imaging. *Curr. Top. Med. Chem.* **8**, 1180–1186 (2008).

171. Luo, K. *et al.* Gadolinium-labeled peptide dendrimers with controlled structures as potential magnetic resonance imaging contrast agents. *Biomaterials* **32**, 7951–7960 (2011).

172. Nwe, K., Bryant, L. H. & Brechbiel, M. W. Poly(amidoamine) Dendrimer Based MRI Contrast Agents Exhibiting Enhanced Relaxivities Derived via Metal Pre-ligation Techniques. *Bioconjug. Chem.* **21**, 1014–1017 (2010).

173. Rosenblum, D., Joshi, N., Tao, W., Karp, J. M. & Peer, D. Progress and challenges towards targeted delivery of cancer therapeutics. *Nat. Commun.* **9**, 1410 (2018).

174. Kroll, A. V. *et al.* Biomimetic Nanoparticle Vaccines for Cancer Therapy. *Adv. Biosyst.* **3**, 1800219 (2019).

175. Chen, Y. *et al.* Broad-Spectrum Neutralization of Pore-Forming Toxins with Human Erythrocyte Membrane-Coated Nanosponges. *Adv. Healthc. Mater.* **7**, 1701366 (2018).

176. Ávila, B. E.-F. de *et al.* Hybrid biomembrane–functionalized nanorobots for concurrent removal of pathogenic bacteria and toxins. *Sci. Robot.* **3**, eaat0485 (2018).

177. Ochyl, L. J. *et al.* PEGylated tumor cell membrane vesicles as a new vaccine platform for cancer immunotherapy. *Biomaterials* **182**, 157–166 (2018).

178. Deng, G. *et al.* Cell-Membrane Immunotherapy Based on Natural Killer Cell Membrane Coated Nanoparticles for the Effective Inhibition of Primary and Abscopal Tumor Growth. *ACS Nano* (2018). doi:10.1021/acsnano.8b05292

179. Pitchaimani, A. *et al.* Biomimetic Natural Killer Membrane Camouflaged Polymeric Nanoparticle for Targeted Bioimaging. *Adv. Funct. Mater.* **0**, 1806817

180. Nguyen, T. D. T. *et al.* Biomimetic surface modification of discoidal polymeric particles. *Nanomedicine Nanotechnol. Biol. Med.* **16**, 79–87 (2019).

181. Wei, X. *et al.* Nanoparticle Functionalization with Platelet Membrane Enables Multifactored Biological Targeting and Detection of Atherosclerosis. *ACS Nano* **12**, 109–116 (2018).

182. Rao, L. *et al.* Erythrocyte Membrane-Coated Upconversion Nanoparticles with Minimal Protein Adsorption for Enhanced Tumor Imaging. *ACS Appl. Mater. Interfaces* **9**, 2159–2168 (2017).

183. Rao, L. *et al.* Microfluidic Electroporation-Facilitated Synthesis of Erythrocyte Membrane-Coated Magnetic Nanoparticles for Enhanced Imaging-Guided Cancer Therapy. *ACS Nano* **11**, 3496–3505 (2017).

184. Lai, P.-Y., Huang, R.-Y., Lin, S.-Y., Lin, Y.-H. & Chang, C.-W. Biomimetic stem cell membrane-camouflaged iron oxide nanoparticles for theranostic applications. *RSC Adv.* **5**, 98222–98230 (2015).

185. Kanal, E., Maravilla, K. & Rowley, H. A. Gadolinium Contrast Agents for CNS Imaging: Current Concepts and Clinical Evidence. *Am. J. Neuroradiol.* **35**, 2215–2226 (2014).

186. Shao, J. *et al.* Erythrocyte Membrane Modified Janus Polymeric Motors for Thrombus Therapy. *ACS Nano* **12**, 4877–4885 (2018).

187. Hu, C.-M. J. *et al.* 'Marker-of-self' functionalization of nanoscale particles through a top-down cellular membrane coating approach. *Nanoscale* **5**, 2664–2668 (2013).

188. Luk, B. T. *et al.* Interfacial interactions between natural RBC membranes and synthetic polymeric nanoparticles. *Nanoscale* **6**, 2730–2737 (2014).

189. Aoki, T. A Comprehensive Review of Our Current Understanding of Red Blood Cell (RBC) Glycoproteins. *Membranes* **7**, (2017).

190. Lauffer, R. B. *et al.* MS-325: albumin-targeted contrast agent for MR angiography. *Radiology* **207**, 529–538 (1998).

191. Caravan, P., Ellison, J. J., McMurry, T. J. & Lauffer, R. B. Gadolinium(III) Chelates as MRI Contrast Agents: Structure, Dynamics, and Applications. *Chem. Rev.* **99**, 2293–2352 (1999).

192. Burger, P., Hilarius-Stokman, P., Korte, D. de, Berg, T. K. van den & Bruggen, R. van. CD47 functions as a molecular switch for erythrocyte phagocytosis. *Blood* **119**, 5512–5521 (2012).

193. Oldenborg, P.-A. *et al.* Role of CD47 as a Marker of Self on Red Blood Cells. *Science* **288**, 2051–2054 (2000).

194. Hadjidemetriou, M., Al-Ahmady, Z. & Kostarelos, K. Time-evolution of in vivo protein corona onto blood-circulating PEGylated liposomal doxorubicin (DOXIL) nanoparticles. *Nanoscale* **8**, 6948–6957 (2016).

195. Hadjidemetriou, M. *et al.* The Human In Vivo Biomolecule Corona onto PEGylated Liposomes: A Proof-of-Concept Clinical Study. *Adv. Mater.* **0**, 1803335

196. Palchetti, S. *et al.* The protein corona of circulating PEGylated liposomes. *Biochim. Biophys. Acta BBA - Biomembr.* **1858**, 189–196 (2016).

197. Elsabahy, M. & Wooley, K. L. Cytokines as biomarkers of nanoparticle immunotoxicity. *Chem. Soc. Rev.* **42**, 5552–5576 (2013).

Appendix A - Supporting information of Chapter 3

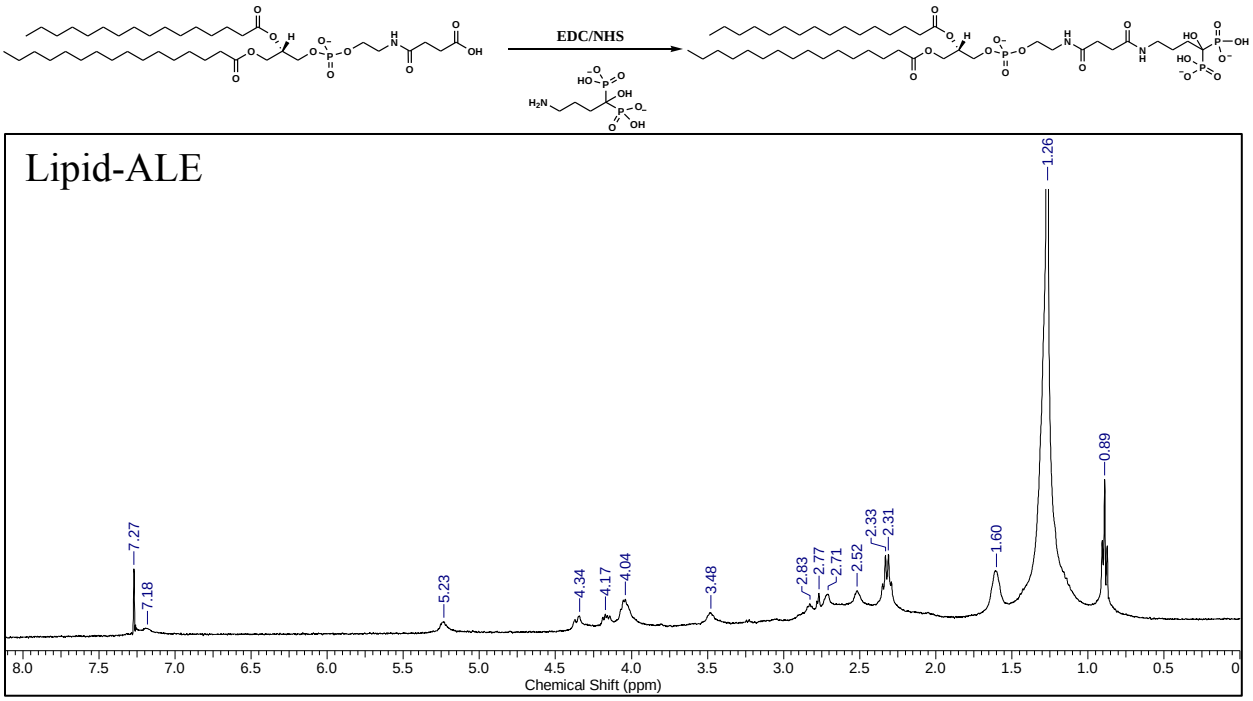

Figure A.1 Synthesis scheme of ALE conjugate lipid reaction along with ^{1}HNMR of ALE-Lipid

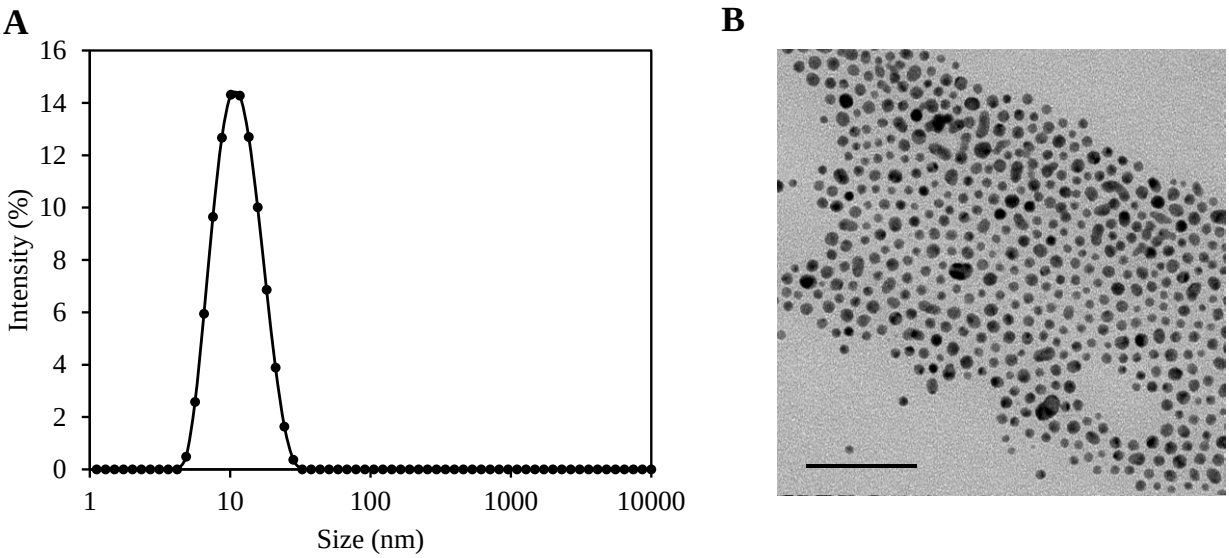

Figure A.2. Physicochemical properties of superparamagnetic iron oxide nanoparticles (SPIONs). (A) Dynamic light scattering showing size distribution of SPIONs. (B) Transmission electron micrograph showing morphology of SPIONs.

Table A.1 Physicochemical properties of HNCs with different SPIONs input (n=6) and SPIONs loaded control PEGylated NPs

Amount of SPIONs input (μg/mL)	10	25	50	100	150	SPION loaded PEGylated NPs
Hydrodynamic size (nm)	80.5 ± 6.1	82.8 ± 5.2	79.9 ± 4.5	82.5 ± 8	83.4 ± 3.2	86.8 ± 3.8
PDI	0.214 ± 0.122	0.266 ± 0.166	0.270 ± 0.071	0.214 ± 0.034	0.282 ± 0.101	0.146 ± 6
PDI width (nm)	33.7 ± 7.1	32.71 ± 4.3	40.5 ± 5	37.4 ± 2.3	39.5 ± 5.9	33.2 ± 6
Zeta potential (mV)	-35.3 ± 0.68	-36.4 ± 1.01	-34.6 ± 0.52	-33.4 ± 0.95	-34.9 ± 1.2	-49.9 ± 5.7

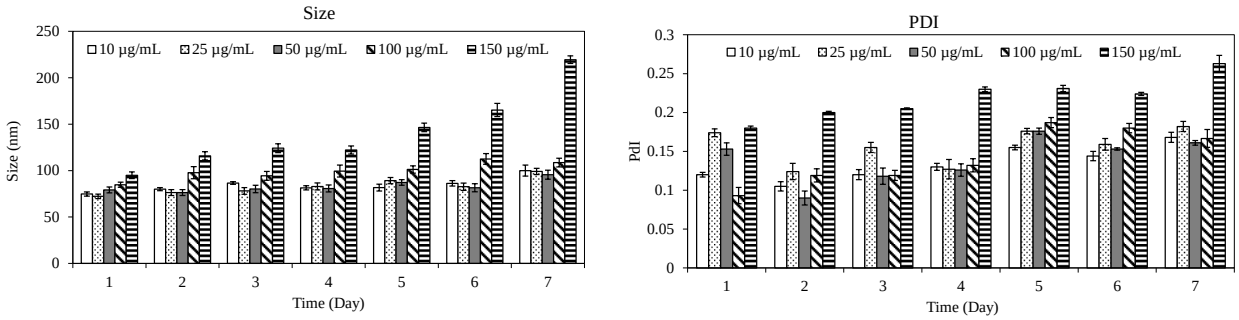

Figure A.3. Stability of different formulation of HNC in ionic condition (PBS)

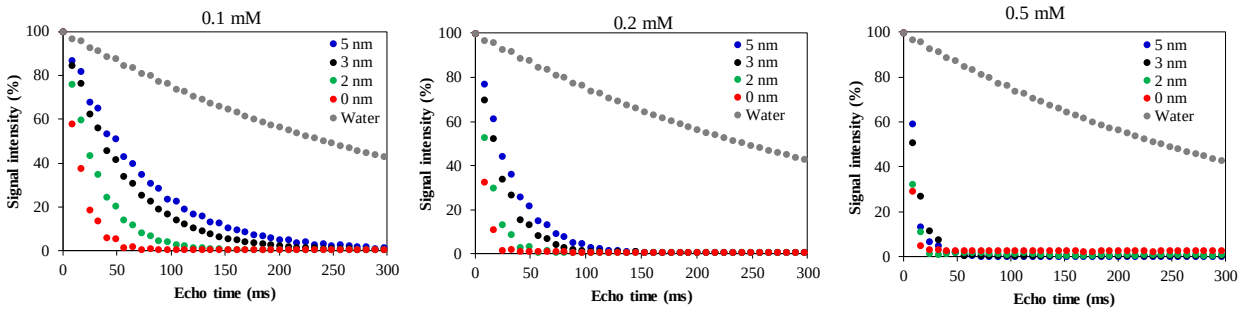

Figure A.4. MR decay curve of 4 different kinds of SPIOs nanocluster at 0.1, 2, and 0.5 mM measured at TR=1500 ms. Water was used as control

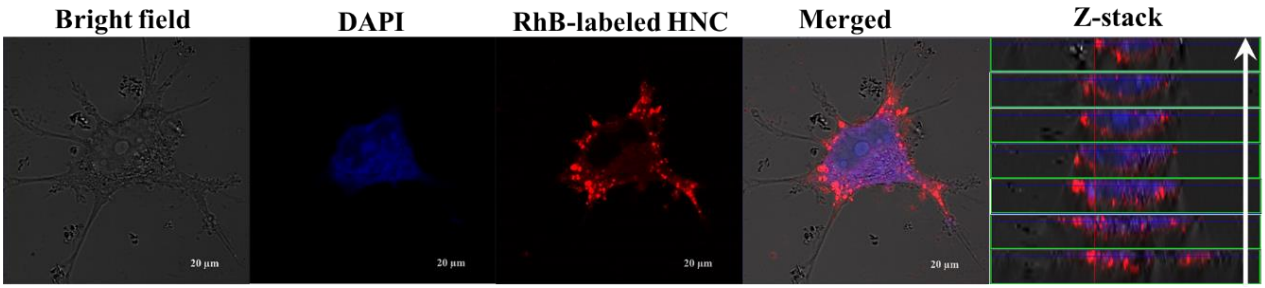

Figure A.5. Confocal images of K7M2 cells incubated with RhB labeled HNC for 3h, at 37ºC. The cell nuclei were stained by DAPI (blue).

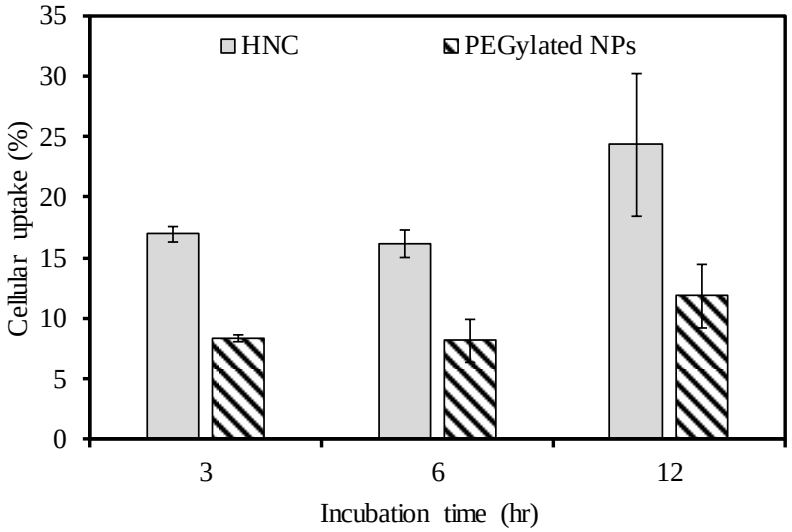

Figure A.6. Cellular uptake of HNC quantified by ICP-MS. PEGylated NPs were used as control

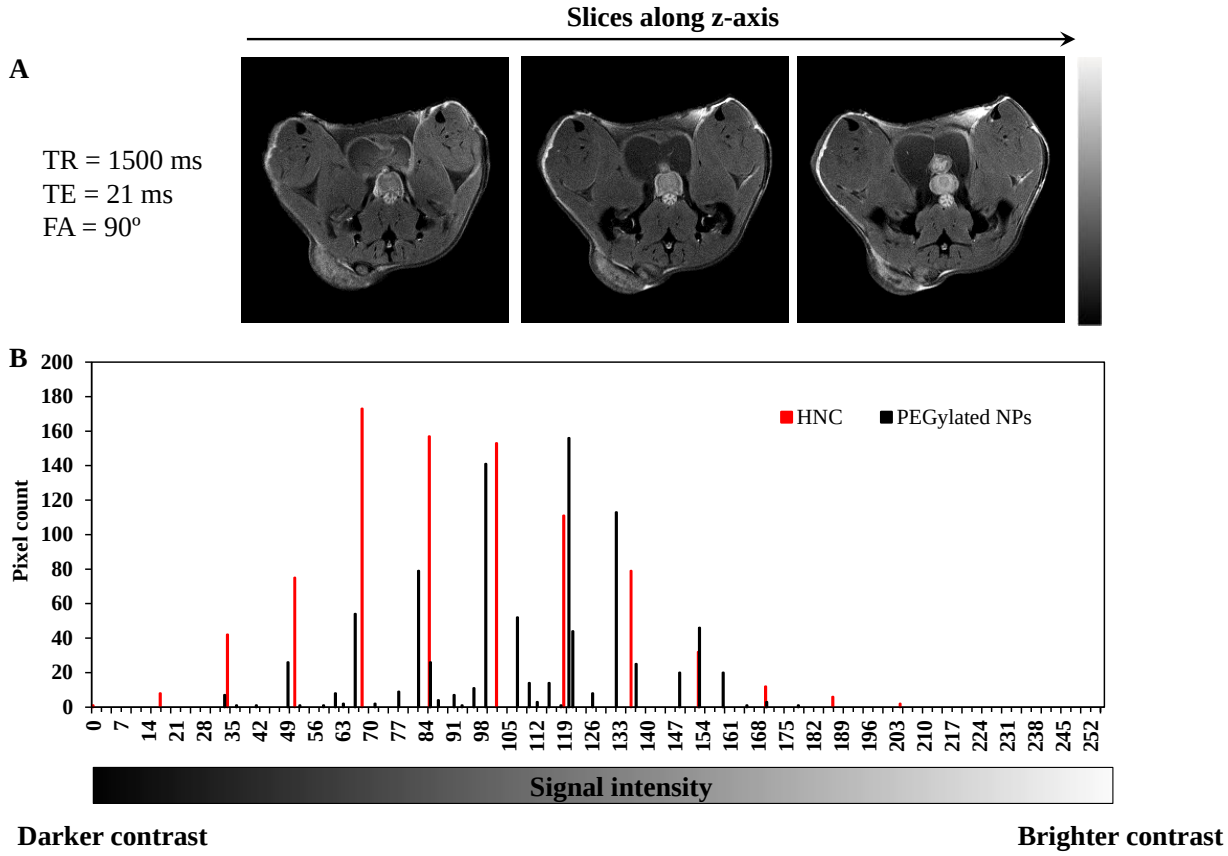

Figure A.7. (A) *Ex vivo* MR images of tumor bearing mouse at different z-plane after IV injection of SPIONs loaded PEGylated NPs (control NPs). (B) Histogram of signal intensity distribution obtained from ImageJ indicating that HNC produces darker contrast than SPIONs loaded PEGylated NPs.

Appendix B - Supporting information of Chapter 4

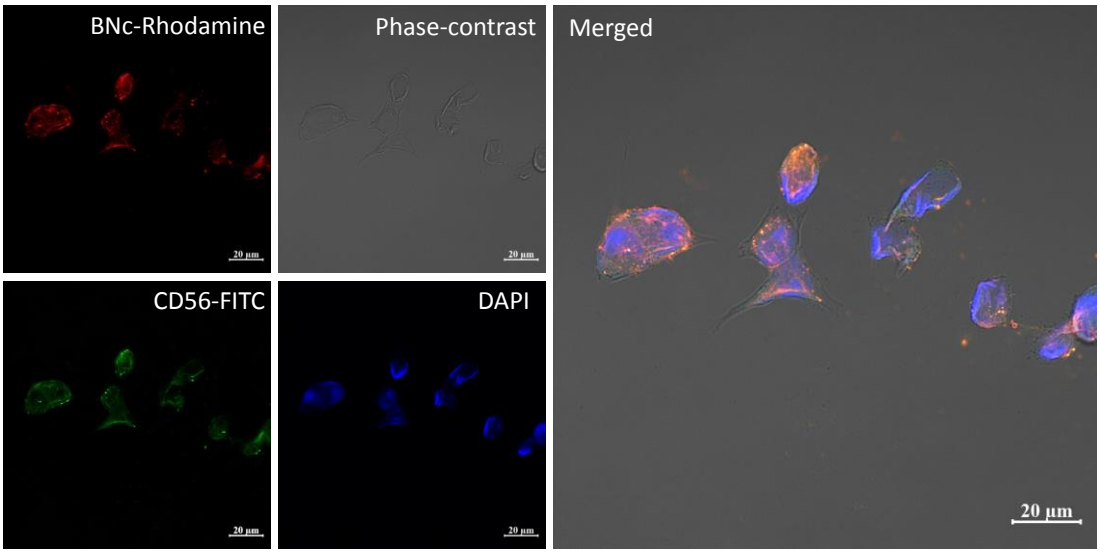

Figure B.1 Confocal laser scanning micrograph of cellular uptake of BNc in MCF-7 cells after 3h of incubation, immunostained with FITC-anti-CD 56.

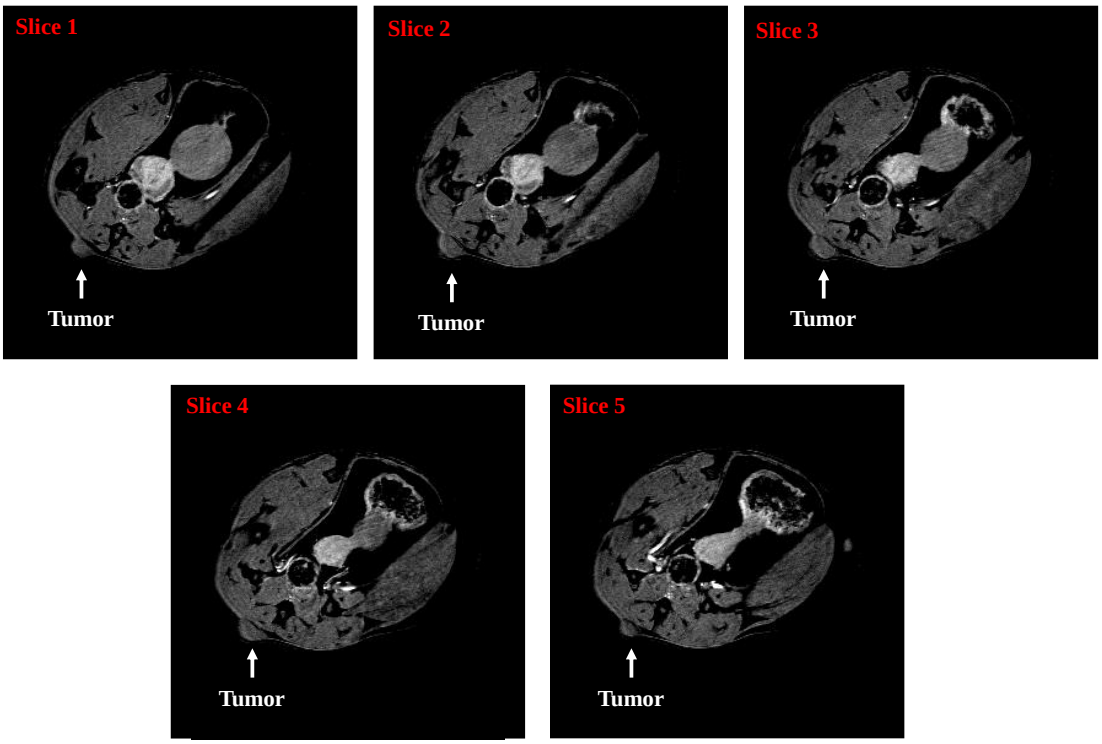

Figure B.2 *Ex vivo* MRI images of MCF-7 tumor bearing mouse.

Mathematical analysis and description of method

Here, transfer rate constants k_{23} and k_{32} illustrate the reversible transfer of nanodrug between two compartments. We can write the kinematic equations in the following form

$$\frac{1}{V_2}\frac{dC_2}{dt} = \frac{-k_{23}C_2}{V_2} + \frac{k_{32}C_3}{V_3} - \frac{k_{el}C_2}{V_2}$$
$$\frac{1}{V_3}\frac{dC_3}{dt} = \frac{-k_{32}C_3}{V_3} + \frac{k_{23}C_2}{V_2} \qquad (1)$$

where C_2 is the concentration of nanodrug in compartment 2 (blood compartment), C_3 is the concentration of nanodrug in compartment 3 (tissue), and V_2 and V_3 are the volumes of compartment two and three, respectively. At time $t = 0$, we have the following boundary conditions for the above equations

$$C_2 = \frac{Dose}{V_2} \qquad \text{and} \qquad C_3 = 0$$

After solving model (1), it follows that

$$C_2 = \frac{Dose}{V_2(B-A)}[(k_{32} - A)e^{-At} - (k_{32} - B)e^{-Bt}]$$

$$C_3 = \frac{Dose\ k_{23}}{V_2(A-B)}[e^{-Bt} - e^{-At}]$$

where

$$A = \frac{1}{2}\left[(k_{23} + k_{32} + k_{el}) - \left(\sqrt{(k_{23} + k_{32} - k_{el})^2 - 4k_{32}k_{el}}\right)\right]$$

$$B = \frac{1}{2}\left[(k_{23} + k_{32} + k_{el}) + \left(\sqrt{(k_{23} + k_{32} - k_{el})^2 - 4k_{32}k_{el}}\right)\right]$$

A and B are first-order constants for the rapid distribution phase and slow elimination phase, respectively, which depend upon constant rates k_{23}, k_{32} and k_{el} and $Dose$ defines i.v. bolus dose.

One may write the following mathematical relationships between the constants A and B and transfer rate constants k_{23} , k_{32} and k_{el},

$$A + B = k_{23} + k_{32} + k_{el}$$

$$AB = k_{32}k_{el}$$

To find the transfer rate constants for bicompartmental model (1), we suppose that the concentration of drug in second compartment follows the subsequent form

$$C_2 = \text{Distribution} + \text{Elimination}$$

As a result, we have

$$C_2 = \alpha e^{-At} + \beta e^{-Bt}$$

where, α and β are the constants for two exponential terms related to distribution and elimination, respectively. In this case, as the initial decline due to the distribution is faster than the final decline due to the elimination of drug, we set the first term to zero. We the have

$$C_2 = \beta e^{-Bt}$$

Transferring it into a natural logarithm format gives

$$\log C_2 = \log \beta - Bt$$

We can then estimate the pharmacokinetic parameters, k_{23} , k_{32} and k_{el}.

From above we can easily find the biological half-time for the slop of the terminal phase B

$$t_{\frac{1}{2}} = \frac{\log(2)}{B}$$

which is the duration of action of a drug losing half of its concentration for pharmacologic or physiologic activity. Plasma half-life of elimination or half-life of the terminal phase is presented as a pharmacokinetic parameter even more than other pharmacokinetic parameters [1]. Needless to say, defining half-life in units of time is of great advantage for this parameter. Based on different

studies, the clearance is the most important pharmacokinetic parameter while it has the units of flow, which is difficult to conceive [2].

We cannot use the half-life for the persistence of drug in body which is why it is required to estimate the mean residence time (MRT) [3]. The residence time of each drug molecule in body is different from another. Some molecules have longer residence time than others. MRT may be calculated by the integration of total residence time of molecules in the body divided by the number of molecules [4].

$$MRT = \frac{\sum Q_i * t_i}{\sum Q_i}$$

where, t_i is the residence time for molecules and Q_i is the number of molecules. As a result, MRT provides the average time for a molecule remaining in the body. As we can assume that each molecule that enters the body will eventually leave the body, we substitute the summation of molecules with the amount of dose and we then rewrite the denominator of the above formula with the following equality:

$$\sum Q_i = \int_0^{Dose} dA(t) = Dose$$

For a drug with a linear kinetic, we can find the average time that a drug molecule spends in the body by the following formula:

$$MRT = \frac{\int_0^\infty tC(t)dt}{\int_0^\infty C(t)dt} = \frac{AUMC}{AUC}$$

where $AUMC$ is the area under the moment curve and AUC is the area under the curve. In mathematical perspective, the following relations is used to find $AUMC$ and AUC:

$$AUMC = \int_0^\infty tC(t)dt \qquad \text{and} \qquad AUC = \int_0^\infty C(t)dt$$

In general, if we consider Bolus IV injection for drug administration we can write

$$C(t) = p_1 e^{-q_1 t} + p_2 e^{-q_2 t} + \cdots + p_n e^{-q_n t}$$

where $C(0) = p_1 + p_2 + \cdots + p_n$. According to the above formulas for area, it follows that:

$$AUMC = \int_0^\infty tC(t)dt = \frac{p_1}{{q_1}^2} + \cdots + \frac{p_n}{{q_n}^2}$$

$$AUC = \int_0^\infty C(t)dt = \frac{p_1}{q_1} + \cdots + \frac{p_n}{q_n}$$

As a result, the mean residence time is given bye

$$MRT = \frac{AUMC}{AUC} = \frac{\frac{p_1}{{q_1}^2} + \cdots + \frac{p_n}{{q_n}^2}}{\frac{p_1}{q_1} + \cdots + \frac{p_n}{q_n}}$$

Therefore, to calculate mean residence time, we should calculate the above ratio.

Clearance is another important concept that is required calculating [5]. The clearance is used to evaluation of the process of drug elimination by the all organs or by an individual organ. In general, liver metabolism and or excretion by kidney are two factors which have important roles in the drug elimination. The clearance is the most important pharmacokinetic parameter as it is the only way to understand the average drug concentration after IV injection of a given dose [6]. To find the plasma clearance, we used the following formula that is based on the relation between the rate of elimination and volume of distribution:

$$\text{Clearance} = Cl = V_d\, K_e$$

where V_d is the volume of distribution and K_e is the rate of elimination. To better illustration, V_d is a known pharmacokinetic parameter that relates the amount of drug in the body or organ for a given dose to the concentration of drug measured in the biological fluid [7]. As a result, V_d may be rewritten in terms of the administrated dose and concentration by the following form,

$$V_d = \frac{Dose}{C}$$

where $Dose$ is the given dose and C is the concentration of drug in the body or each organ. The rate of elimination, K_e, can be also defined based on the following formula

$$K_e = B = \frac{\ln(2)}{t_{\frac{1}{2}}}$$

Main results

Bicompartmental model (1) provides a useful *in vitro* model to study drug absorption, distribution and elimination in blood, tumor and tissue. We simulated the process of drug distribution and elimination from blood to tissue and conversely from tissue to circulation system. According to pharmacokinetics and biodistribution of PLG-NK and NKsomes, we calculated the half-life, AUC, V_d , Cl and MRT from 0 to 48h. **Table B.1** shows the 95% confidence interval with the mean for each parameter using the following quanitity

$$\bar{k} \pm k^* \times \frac{\text{SEM}}{\sqrt{n}}$$

where $\bar{k}$ represents the mean value, k^* denotes the multiplier number, SEM shows the standard error of the mean, and n is the sample size. AUC is calculated using the numerical integration technique called Newton-Cotes formula (Butt, 2009) applied to the Composite Simpson's rule of radioactivity concentrations (%ID/ml blood) versus time curve from 0 to 48h and extrapolation from 48h to infinity.

One-way analysis of variance (ANOVA) was used to assess statistically significant differences ($p<0.05$) between the tissue and tumor biodistributions. Using the ANOVA test, we compare the means of tissue and tumor biodistributions for the same drug distribution in each organ using the F- test.

Table B.1 Parameters of pharmacokinetics and biodistribution of PLG-NK NPs.

Formulation	$t_{\frac{1}{2}}(h)$	$AUC_{0-\infty}$(%ID.h/mL)	V_d	Cl(mL/h)	MRT(h)
PLG-NK	9.51	1068.8	3.85	0.28	13.61

We used a bicompartmental pharmacokinetic model to study drug disposition in each organ. According to the data collected at different time points with three replications, and via the equations governing on the concentration of second compartment (blood compartment), we fitted our experimental data to bicompartmental model (1) in **Supporting Figure B.3**. Experimental data was quantitatively analyzed using several Toolboxes in MATLAB® 2017a such as Statistics and Machine Learning Toolbox, Global Optimization and Curve Fitting. Using these Toolboxes, we were able to estimate the goodness-of-fit statistics in this structure with scale (Normalize) and robust fitting options. In **Supporting Figure B.3**, the red dots with error-bars represent the biodistribution of NPs over the course of distribution and blue solid curves show the model fit using equation (1).

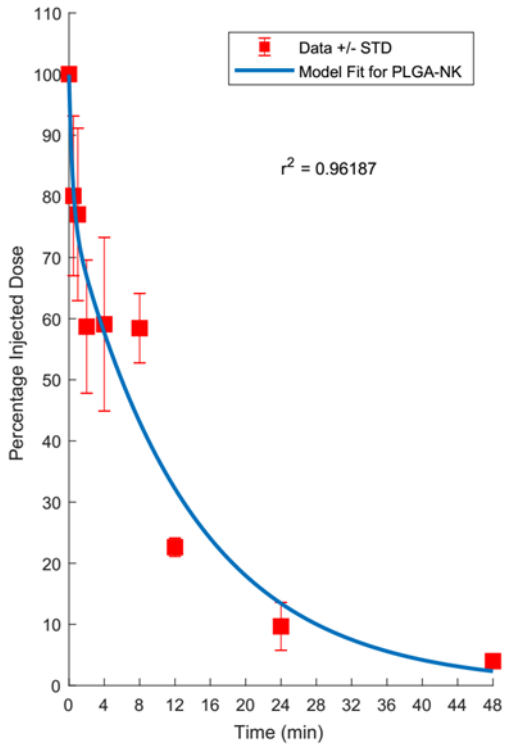

Figure B.3 Model fit to the percentage injected dose using two compartmental model for PLGA-NK.

References

1. Toutain, P.-L. and A. BOUSQUET-MÉLOU, *Plasma terminal half-life.* Journal of veterinary pharmacology and therapeutics, 2004. **27**(6): p. 427-439.
2. Toutain, P.L. and A. Bousquet-Melou, *Plasma terminal half-life.* Journal of Veterinary Pharmacology and Therapeutics, 2004. **27**(6): p. 427-439.
3. Sahin, S. and L.Z. Benet, *The operational multiple dosing half-life: a key to defining drug accumulation in patients and to designing extended release dosage forms.* Pharmaceutical research, 2008. **25**(12): p. 2869-2877.
4. Sobol, E. and M. Bialer, *The relationships between half-life (t1/2) and mean residence time (MRT) in the two-compartment open body model.* Biopharmaceutics & drug disposition, 2004. **25**(4): p. 157-162.
5. Toutain, P.-L. and A. BOUSQUET-MÉLOU, *Plasma clearance.* Journal of veterinary pharmacology and therapeutics, 2004. **27**(6): p. 415-425.
6. Mehta, A.C., *Pharmacokinetics and the analytical chemist.* Talanta, 1987. **34**(3): p. 355-360.
7. Toutain, P.-L. and A. BOUSQUET-MÉLOU, *Volumes of distribution.* Journal of veterinary pharmacology and therapeutics, 2004. **27**(6): p. 441-453.

Appendix C - Supporting information of Chapter 5

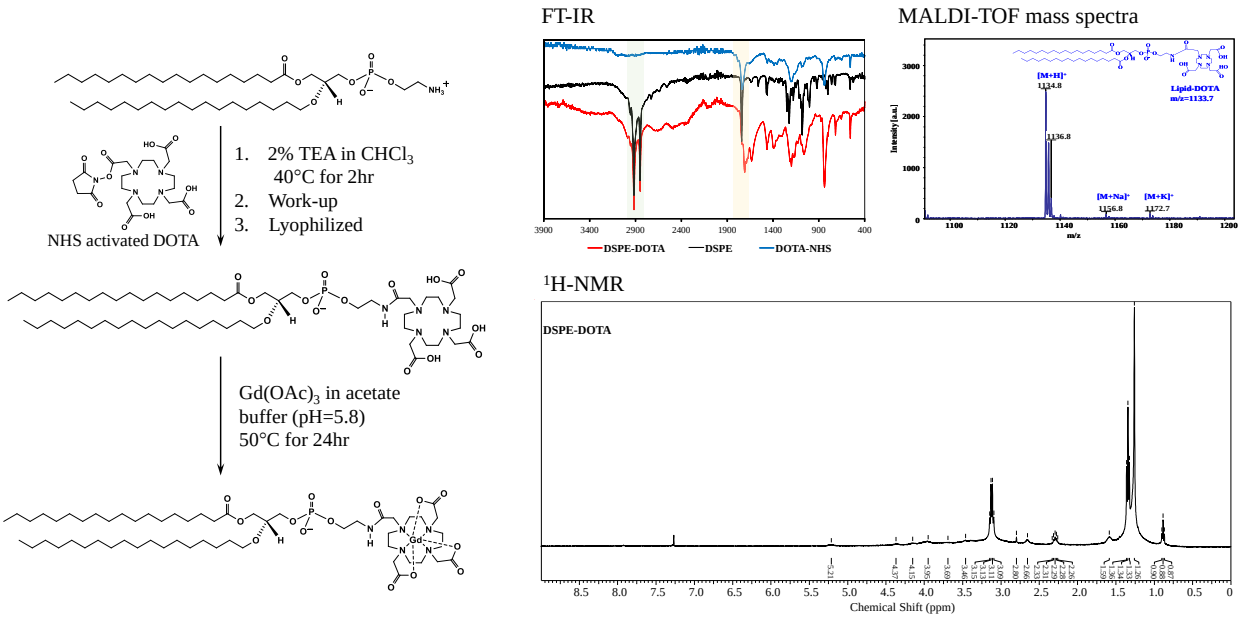

Figure C.1 Synthesis of DSPE-DOTA-Gd and its corresponding molecular analysis

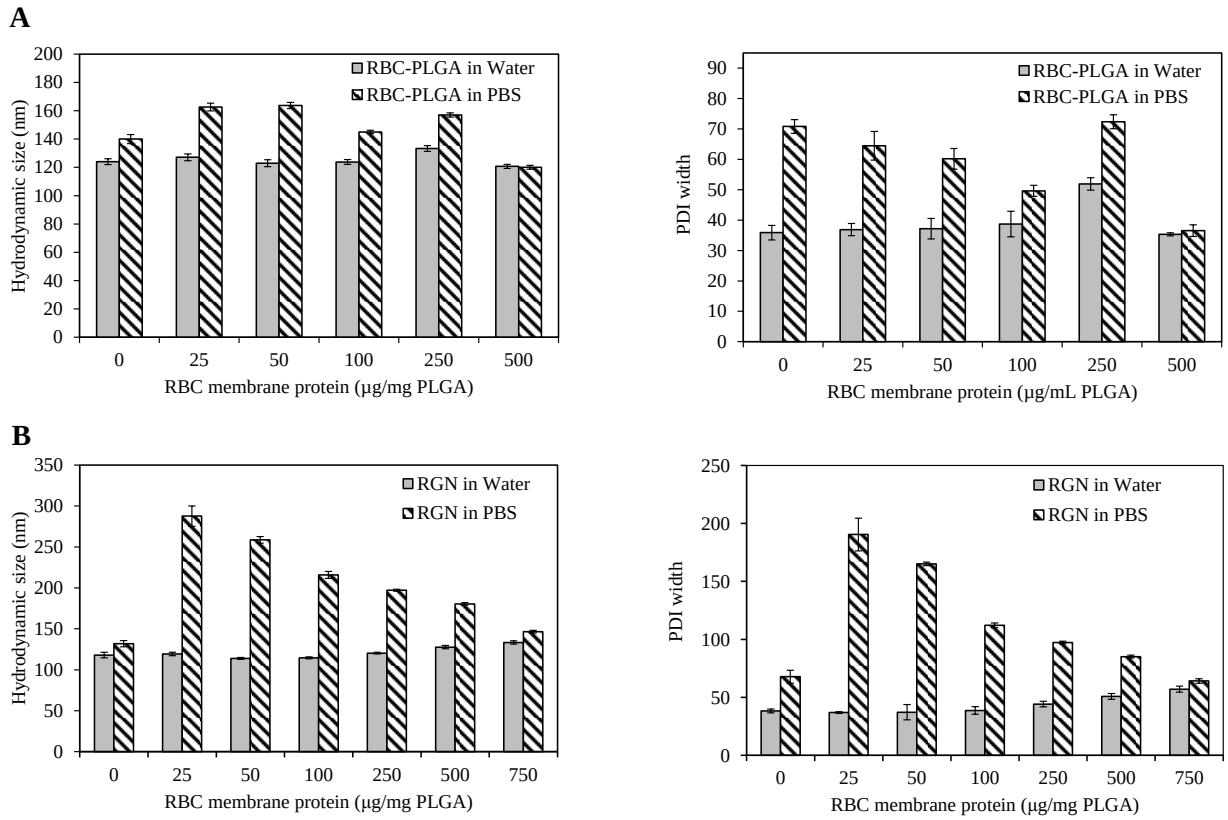

Figure C.2 Optimize coating RBC coating condition based on RBC membrane protein concentration

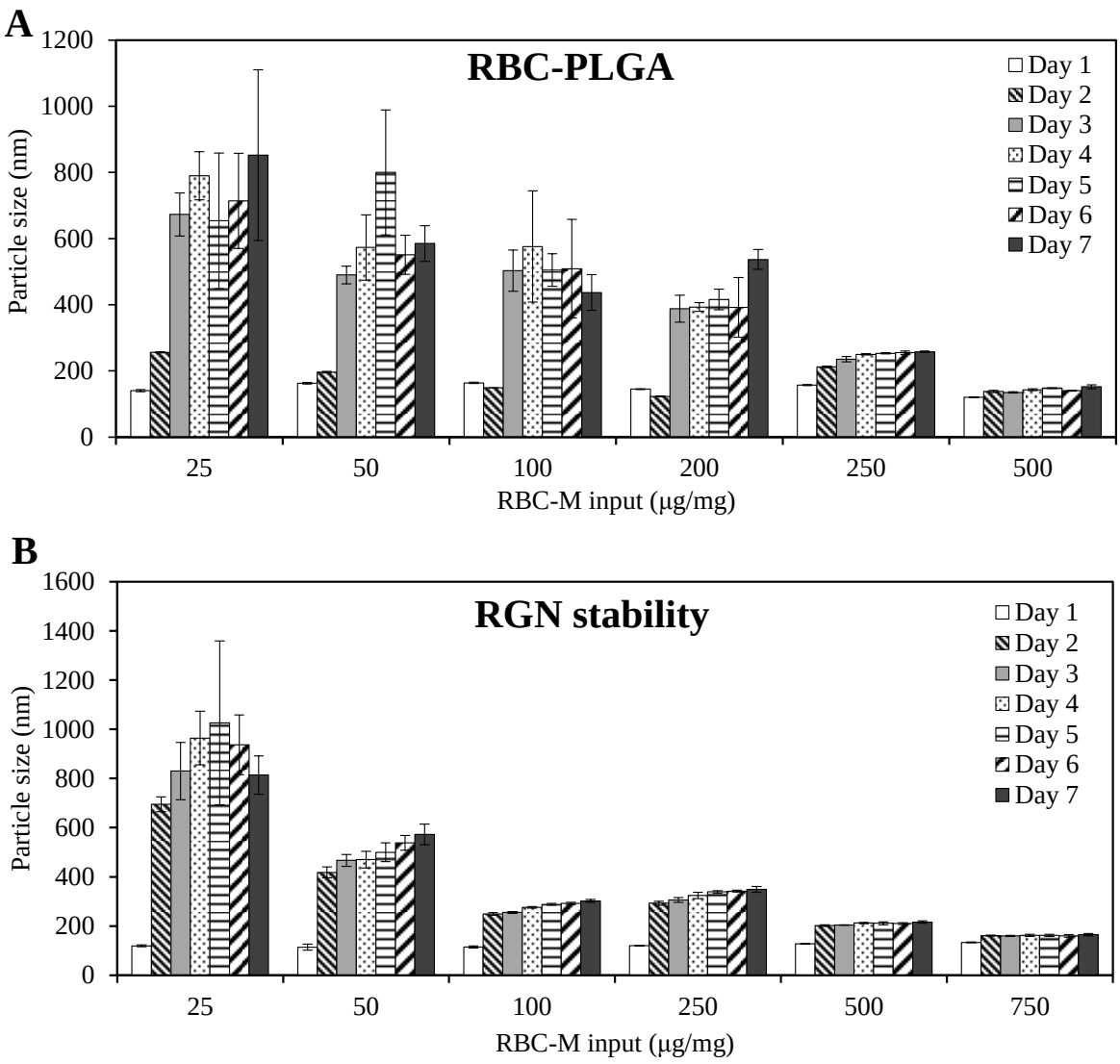

Figure C.3 Stability of RBC-PLGA and RBC-Gd-PLGA under physiological condition (pH 7.4)

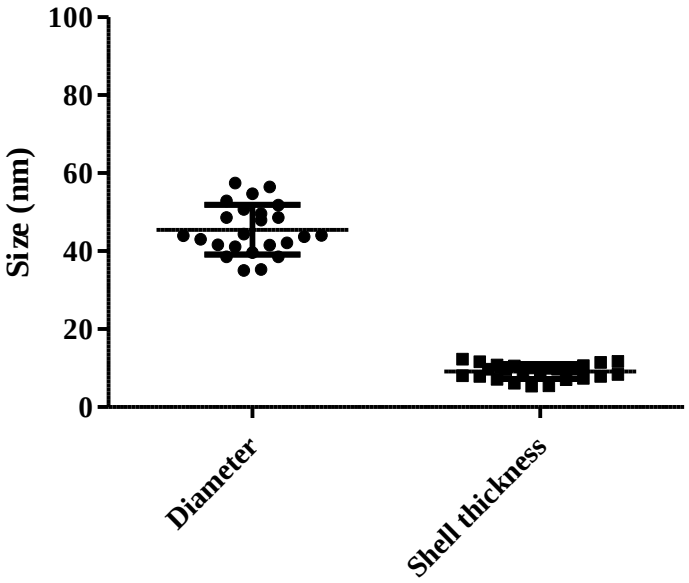

Figure C.4 TEM analysis for core diameter and shell thickness of RBC-Gd-PLGA

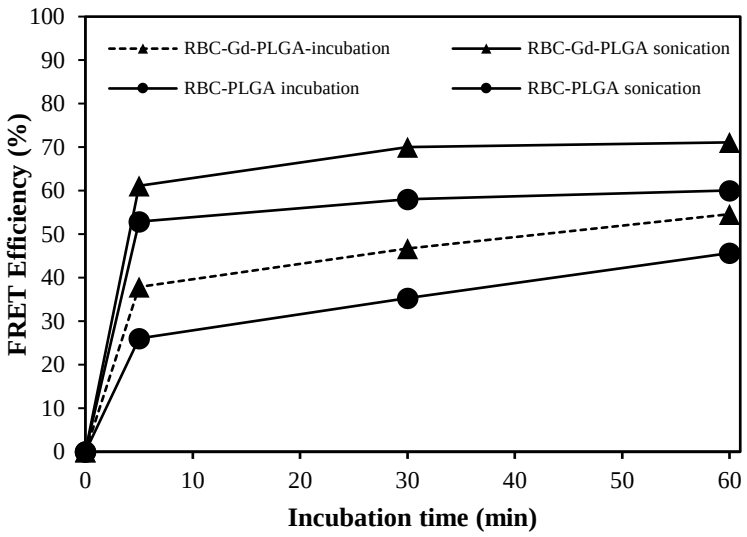

Figure C.5 Stability of RBC-PLGA and RBC-Gd-PLGA under physiological condition (pH 7.4)

Table C.1 *In vitro* macrophage uptake study of PEGylated, PLGA and RBC-Gd-PLGA NPs after 0.5, 1.5, 3, and 6hr incubations analyzed using one-way ANOVA with Turkey's multiple comparison post-test

Incubation time	Tukey's Multiple Comparison Test	Mean Diff.	q	Significant (P < 0.05)	95% CI of diff
0.5 hr	PEGylated NPs vs PLGA	-3916	15.07	Yes	-4789 to -3044
	PEGylated NPs vs RBC-Gd-PLGA	1832	6.632	Yes	905.3 to 2759
	PLGA vs RBC-Gd-PLGA	5749	21.61	Yes	4856 to 6641
1.5 hr	PEGylated NPs vs PLGA	-3732	13.50	Yes	-4660 to -2805
	PEGylated NPs vs RBC-Gd-PLGA	2093	7.841	Yes	1198 to 2989
	PLGA vs RBC-Gd-PLGA	5826	19.09	Yes	4802 to 6849
3 hr	PEGylated NPs vs PLGA	446.1	1.250	No	-751.5 to 1644
	PEGylated NPs vs RBC-Gd-PLGA	3014	8.475	Yes	1821 to 4208
	PLGA vs RBC-Gd-PLGA	2568	7.755	Yes	1457 to 3679
6 hr	PEGylated NPs vs PLGA	3721	7.707	Yes	2101 to 5340
	PEGylated NPs vs RBC-Gd-PLGA	2959	7.089	Yes	1559 to 4360
	PLGA vs RBC-Gd-PLGA	-761.2	1.538	No	-2421 to 899.0

Table C.2 T_1 relaxation time of RBC-Gd-PLGA

Concentration of GdL in sample	Amount of GdL input			
	400ug	**200ug**	**100 ug**	**50 ug**
Water	4083.12	4083.12	4083.12	4083.12
12.5 µg	2164.39	1820.79	5080.49	8681.91
25 µg	1727.13	1306.24	3851.96	5075.60
50 µg	1163.18	663.99	2257.88	3391.79
100 µg	571.43	200.62	1051.05	1757.09

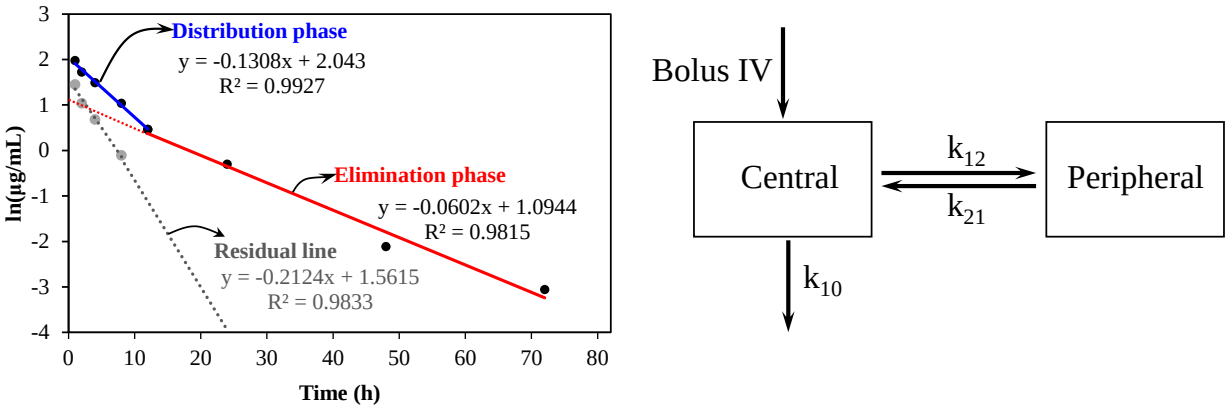

Figure C.6 Plasma RBC-Gd-PLGA concentrations in natural logarithmic scale with linear components of a two-compartment model after an intravenous bolus dose.

Table C.3 Pharmacokinetic parameters of RBC-Gd-PLGA calculated based on two compartment model using method of residuals**.**

Pharmacokinetic parameters	Two-compartment model	Equations
Elimination phase		
β (h^{-1})	0.06	Slope of red line
B_0 (µg/mL)	3.12	$B_0 = \frac{C_t}{e^{-\beta t}}$
$t_{1/2\beta}$ (h)	11.6	$t_{1/2\beta} = \frac{\ln(2)}{\beta} = \frac{0.693}{\beta}$
Distribution phase		
α (h^{-1})	0.21	Slope for C_p (residual)*
A_0 (µg/mL)	4.88	$A_0 = \frac{C_{p(residual)}}{e^{-\alpha t}}$
$t_{1/2\alpha}$ (h)	3.27	$t_{1/2\alpha} = \frac{\ln(2)}{\alpha} = \frac{0.693}{\alpha}$
Concentration at time zero		
C_0 (µg/mL)	8.00	$C_0 = A_0 + B_0$
Rate constant		
k_{21} (h^{-1})	0.12	$k_{21} = \frac{A \times \beta + B \times \alpha}{A + B}$
k_{10} (h^{-1})	0.11	$k_{10} = \frac{\alpha \times \beta}{k_{21}}$
k_{10} (h^{-1})	0.05	$k_{12} = (\alpha + \beta) - (k_{21} + k_{10})$
Volume of distribution		
V_c (mL)	2.00	$V_c = \frac{D}{C_0} = \frac{D}{A_0 + B_0}$
V_p (mL)	0.77	$V_p = \frac{V_c \times k_{12}}{k_{21}}$
V_{dss} (mL)	2.78	$V_{ssd} = V_p + V_c$
Area under the curve		
AUC (µg.h/mL)	75.02	$AUC = \frac{A}{\alpha} + \frac{B}{\beta}$
Clearance total		
Cl_{total} (mL/h)	0.21	$Cl_{total} = \frac{D}{AUC}$

Appendix D - List of Abbreviation

Name	Abbreviation
1,1'-Dioctadecyl-3,3,3',3'-Tetramethylindotricarbocyanine Iodide	DiR
1,2-dipalmitoyl-sn-glycero-3-phosphoethanolamine-N-(succinyl) (sodium salt)	16:0 Succinyl PE
1,2-distearoyl-sn-glycero-3-phosphoethanolamine	DSPE
1,2-distearoyl-sn-glycero-3-phosphoethanolamine-N-[carboxy(polyethylene glycol)-2000] (sodium salt)	DSPE-PEG-COOH
1-ethyl-3-(3-dimethylaminopropyl)carbodiimide hydrochloride	EDC
2-(*N*-morpholino)ethanesulfonic acid	MES
3-(4,5-dimethylthiazol-2-yl)-2,5-diphenyl tetrazolium bromide	MTT
4′,6-diamidino-2-phenylindole	DAPI
Alendronic acid	ALE
Alendronic acid conjugated lipid	ALE-lipid
Alpha Minimum Essential Medium	α-MEM
Analysis of variance	ANOVA
Area under the curve	AUC
Bicinchoninic acid assay	BCA
Biomimetic nanoconstruct	BNc
Carbon dioxide	CO_2
Chromium	Cr
Circulation half-life	$t_{1/2}$
Clearance	CLSM
Coefficient factor	R^2
Computed Tomography	CT
Confocal Laser Scanning Microscope	CLSM
Contrast-enhanced magnetic resonance imaging	ceMRI
Deterium oxide	D_2O
Deuterated chloroform	$CDCl_3$
Dimethyl sulfoxide	DMSO
Doxorubicin	DOX
Dulbecco's Modified Eagle Medium	DMEM
Dynamic Light Scattering	DLS
Echo time	TE
Elimination rate	K_{el}
Enhanced Permeability and Retention effect	EPR effect
Fast slow angle shot	FLASH
Fetal bovine serum	FBS
Field of view	FOV

Fluorescein isothiocyanate	FITC
Fluorescence resonance energy transfer	FRET
Fluorescence-activated cell sorting	FACS
Food and Drug Administration	FDA
Fourier-transform infrared spectroscopy	FT-IR
Gadobenate dimeglumine	Gd-BOPTA
Gadofosveset trisodium	MS325
Gadolinium	Gd
Gadolinium (III) acetate hydrate	$Gd(OAc)_3$
Gadolinium based contrast agent	GBCA
Gadolinium lipid	Gd-lipid or Gd-L
Gadopentetate dimeglumine	Gd-DTPA
Gadoxetic acid disodium	Gd-EOB-DTPA
Glyceraldehyde 3-phosphate dehydrogenase	GAPDH
Glycophorin A	GPA
Half maximal inhibitory concentration	IC_{50}
Hematoxylin and eosin	H&E
Horseradish peroxidase	HPR
Hybrid nanoconstruct	HNC
Hydrocloric acid	HCl
Hydroxyapatite	Hap
Immunoglobulin G	IgG
Inductively coupled plasma mass spectrometry	ICP-MS
Injected dose	ID
Institutional Animal Care and Use Committee	IACUC
Institutional Biosafety Committee	IBC
Interleukin	IL
Iron	Fe
Limit of detection	LOD
Lipopolysaccharides	LPS
Longitudinal relaxation time	T_1
Longitudinal relaxivity	r_1
L-α-Phosphatidylethanolamine-N-(lissamine rhodamine B sulfonyl) (Ammonium Salt) (Egg-Transphosphatidylated, Chicken)	Egg Liss Rhod PE
Magnetic Resonance	MR
Magnetic Resonance Imaging	MRI
Manganese	Mn
Mean resident time	MRT
Molecular weight	Mw
Molecular weight cut off	MWCO
Mononuclear phagocyte system	MPS

Nanoparticle	NP
Natural killer cell	NK cell
Natural killer cell membrane	NKM
Near-infrared	NIR
Nephrogenic systemic fibrosis	NSF
N-hydroxysuccinimide	NHS
N-Hydroxysuccinimidyl ester activated 1,4,7,10-tetraazacyclododecane-1,4,7,10-tetraacetic acid	DOTA-NHS
Nitric acid	HNO_3
Phosphate buffered saline	PBS
Poly(lactic-co-glycolic acid)	PLGA
Polydispersity index	PDI
Polyethylene glycol	PEG
Polyethylene glycolated	PEGylated
Positron Emission Tomography	PET
Pressure of oxygen	pO_2
Proton nuclear magnetic resonance	H-NMR
Receptor activator of nuclear factor κB	RANK
Receptor activator of nuclear factor κB ligand	RANKL
Red blood cell	RBC
Red blood cell membrane	RBC-M
Red blood cell membrane coated paramagnetic polymeric nanoparticles	RBC-Gd-PLGA NPs
Repetition time	TR
Reticuloendothelial system	RES
Rhodamine dye	RhB
Sodium Dodecyl Sulphate-Polyacrylamide Gel Electrophoresis	SDS-PAGE
Superparamagnetic iron oxide nanoparticle	SPION
Targeted nanoparticle	TNP
Transmission Electron Micrograph	TEM
Transverse relaxation time	T_2
Transverse relaxivity	r_2
Triethylamine	TEA
Tris-buffered saline with Tween 20	TBST
Tumor Necrosis Factor	TNF
Tumor to blood	T/B
Type I transforming growth factor (TGF)-β receptor	TβR-I
Ultraviolet–visible spectroscopy	UV-Vis
United State of America	USA
Volume of distribution	Vd

Appendix E - List of publications

1. Abello J, **Nguyen TDT**, Marasini R, Aryal S, Weiss ML. Biodistribution of Gadolinium- and Near Infrared-Labeled Human Umbilical Cord Mesenchymal Stromal Cell- Derived Exosomes in Tumor Bearing Mice. ***Theranostic.*** **In press.**
2. **Nguyen, T. D. T.,** Aryal, S., Pitchaimani, A., Park, S., Key, J., & Aryal, S. (2019). Biomimetic surface modification of discoidal polymeric particles. ***Nanomedicine: Nanotechnology, Biology and Medicine***, *16*, 79-87.
3. Pitchaimani, A., **Nguyen, T. D. T.**, Marasini, R., Eliyapura, A., Azizi, T., Jaberi-Douraki, M., & Aryal, S. (2019). Biomimetic Natural Killer Membrane Camouflaged Polymeric Nanoparticle for Targeted Bioimaging. ***Advanced Functional Materials***, 1806817. **(Equal Contribution first author)**
4. Marasini, R., Pitchaimani, A., **Nguyen, T. D.T**, Comer, J., & Aryal, S. (2018). Influence of Polyethylene Glycol Passivation on the Surface Plasmon Resonance Induced Photothermal Properties of Gold Nanorods. ***Nanoscale*****.**
5. Pitchaimani, A., **Nguyen, T. D. T.,** & Aryal, S. (2018). Natural killer cell membrane infused biomimetic liposomes for targeted tumor therapy. ***Biomaterials***, *160*, 124-137.
6. **Nguyen, T. D. T.,** Pitchaimani, A., Ferrel, C., Thakkar, R., & Aryal, S. (2018). Nano-confinement-driven enhanced magnetic relaxivity of SPIONs for targeted tumor bioimaging. ***Nanoscale,*** *10*(1), 284-294.
7. Eshete M, Bailey K, **Nguyen TDT**, Aryal S, Choi, SO. Interaction of Immune System Protein with PEGylated and Un-PEGylated Polymeric Nanoparticles. ***Advances in Nanoparticles*** (2017) *6*(03), 103.
8. Aryal S, **Nguyen TDT**, Pitchaimani A, Shrestha TB, Biller D, Troyer D. Membrane fusion-mediated gold nanoplating of red blood cell: a bioengineered CT-contrast agent. ***ACS Biomaterials Science & Engineering*** (2017) 3, 36-41.
9. Pitchaimani A, **Nguyen TDT**, M Koirala, Y Zhang, Aryal S. Impact of cell adhesion and migration on nanoparticle uptake and cellular toxicity. ***Toxicology in vitro*** (2017) 43, 29-39.
10. Ramani M, **Nguyen TDT**, Aryal S, Ghosh KC, DeLong RK. Elucidating the RNA Nano-bio Interface: Mechanisms of Anti-Cancer Poly I: C RNA and Zinc Oxide Nanoparticle Interaction. ***The Journal of Physical Chemistry C*** (2017) 129, 15702.
11. Pitchaimani A, **Nguyen TDT**, Maurmann L, Key J, Bossmann SH, Aryal S. Gd^{3+} Tethered Gold Nanorods for Combined Magnetic Resonance Imaging and Photo-Thermal Therapy. ***Journal of Biomedical Nanotechnology*** (2017) 13, 417-426.
12. Muhammad F, **Nguyen TDT**, Raza A, Akhtar B, Aryal S**.** A review on nanoparticle-based technologies for biodetoxification. ***Drug and Chemical Toxicology*** (2017) 1-9.
13. **Nguyen TDT**, Pitchaimani A, Aryal S. Engineered nanomedicine with alendronic acid corona improves targeting to osteosarcoma. ***Scientific Reports*** (2016) 6, 36707-36716.

14. **Nguyen TDT**, Pitchaimani A, Koirala MB, Muhammad F, Aryal S**.** Engineered biomimetic nanoabsorbent for cellular detoxification of chemotherapeutics. ***RSC Advances*** *(*2016) 6, 33003-33008.

15. Pitchaimani A, **Nguyen TDT**, Wang H, Bossmann SH, Aryal S**.** Design and characterization of gadolinium infused theranostic liposomes. ***RSC Advances*** (2016) 6, 36898-36905.

16. Koirala MB, **Nguyen TDT**, Pitchaimani A, Choi SO, Aryal S**.** Synthesis and characterization of biomimetic hydroxyapatite nanoconstruct using chemical gradient across lipid bilayer. ***ACS Applied Materials Interfaces*** (2015) 7, 27382–27390.

17. Lu J, Maezawa I, Weerasekara S, Erenler R, **Nguyen TDT**, Nguyen J, Swisher LZ, Li J, Jin, LW, Ranjan A, Srivastava SK, Hua DH. Syntheses, neural protective activities, and inhibition of glycogen synthase kinase-3β of substituted quinolines. ***Bioorganic & medicinal chemistry letters*** (2014), *24*(15), 3392-3397.

Appendix F - Copyright permissions

FW: Copy right permission to include in Ph.D. dissertation

RSC1 (shared)
<RSC1@rsc.org>
Tue 3/19/2019 3:30
To: Tuyen Nguyen <tuyennguyen@ksu.edu>

Dear Tuyen Nguyen

The Royal Society of Chemistry (RSC) hereby grants permission for the use of your paper(s) specified below in the printed and microfilm version of your thesis. You may also make available the PDF version of your paper(s) that the RSC sent to the corresponding author(s) of your paper(s) upon publication of the paper(s) in the following ways: in your thesis via any website that your university may have for the deposition of theses, via your university's Intranet or via your own personal website. We are however unable to grant you permission to include the PDF version of the paper(s) on its own in your institutional repository. The Royal Society of Chemistry is a signatory to the STM Guidelines on Permissions (available on request).

Please note that if the material specified below or any part of it appears with credit or acknowledgement to a third party then you must also secure permission from that third party before reproducing that material.

Please ensure that the thesis states the following:

Reproduced by permission of The Royal Society of Chemistry

and include a link to the paper on the Royal Society of Chemistry's website.

Please ensure that your co-authors are aware that you are including the paper in your thesis.

Kind regards,

Ruba Miah
Publishing Assistant,
Customer Services Royal
Society of Chemistry
Thomas Graham House
Science Park, Milton
Road Cambridge, CB4
0WF, UK

JOHN WILEY AND SONS LICENSE TERMS AND CONDITIONS

Apr 02, 2019

This Agreement between Kansas State University -- Tuyen Nguyen ("You") and John Wiley and Sons ("John Wiley and Sons") consists of your license details and the terms and conditions provided by John Wiley and Sons and Copyright Clearance Center.

License Number	4551950433546
License date	Mar 18, 2019
Licensed Content Publisher	John Wiley and Sons
Licensed Content Publication	Advanced Functional Materials
Licensed Content Title	Biomimetic Natural Killer Membrane Camouflaged Polymeric Nanoparticle for Targeted Bioimaging
Licensed Content Author	Arunkumar Pitchaimani, Tuyen Duong Thanh Nguyen, Ramesh Marasini, et al
Licensed Content Date	Dec 5, 2018
Licensed Content Volume	29
Licensed Content Issue	4
Licensed Content Pages	11
Type of use	Dissertation/Thesis
Requestor type	Author of this Wiley article
Format	Print and electronic
Portion	Full article
Will you be translating?	No
Title of your thesis / dissertation	engineering nanoparticles using chemical and biological approaches for tumor targeted delivery
Expected completion date	May 2019
Expected size (number of pages)	181
Requestor Location	Kansas State University 1800 Denison Avenue P218 Mosier Hall Manhattan, KS 66506 United States Attn: Kansas State University
Publisher Tax ID	EU826007151

Total 0.00 USD

Terms and Conditions

TERMS AND CONDITIONS

This copyrighted material is owned by or exclusively licensed to John Wiley & Sons, Inc. or one of its group companies (each a"Wiley Company") or handled on behalf of a society with which a Wiley Company has exclusive publishing rights in relation to a particular work (collectively "WILEY"). By clicking "accept" in connection with completing this licensing transaction, you agree that the following terms and conditions apply to this transaction (along with the billing and payment terms and conditions established by the Copyright Clearance Center Inc., ("CCC's Billing and Payment terms and conditions"), at the time that you opened your RightsLink account (these are available at any time at http://myaccount.copyright.com).

Terms and Conditions

- The materials you have requested permission to reproduce or reuse (the "Wiley Materials") are protected by copyright.
- You are hereby granted a personal, non-exclusive, non-sub licensable (on a stand-alone basis), non-transferable, worldwide, limited license to reproduce the Wiley Materials for the purpose specified in the licensing process. This license, **and any CONTENT (PDF or image file) purchased as part of your order,** is for a one-time use only and limited to any maximum distribution number specified in the license. The first instance of republication or reuse granted by this license must be completed within two years of the date of the grant of this license (although copies prepared before the end date may be distributed thereafter). The Wiley Materials shall not be used in any other manner or for any other purpose, beyond what is granted in the license. Permission is granted subject to an appropriate acknowledgement given to the author, title of the material/book/journal and the publisher. You shall also duplicate the copyright notice that appears in the Wiley publication in your use of the Wiley Material. Permission is also granted on the understanding that nowhere in the text is a previously published source acknowledged for all or part of this Wiley Material. Any third party content is expressly excluded from this permission.
- With respect to the Wiley Materials, all rights are reserved. Except as expressly granted by the terms of the license, no part of the Wiley Materials may be copied, modified, adapted (except for minor reformatting required by the new Publication), translated, reproduced, transferred or distributed, in any form or by any means, and no derivative works may be made based on the Wiley Materials without the prior

permission of the respective copyright owner.**For STM Signatory Publishers clearing permission under the terms of the STM Permissions Guidelines only, the terms of the license are extended to include subsequent editions and for editions in other languages, provided such editions are for the work as a whole in situ and does not involve the separate exploitation of the permitted figures or extracts,**You may not alter, remove or suppress in any manner any copyright, trademark or other notices displayed by the Wiley Materials. You may not license, rent, sell, loan, lease, pledge, offer as security, transfer or assign the Wiley Materials on a stand-alone basis, or any of the rights granted to you hereunder to any other person.

- The Wiley Materials and all of the intellectual property rights therein shall at all times remain the exclusive property of John Wiley & Sons Inc, the Wiley Companies, or their respective licensors, and your interest therein is only that of having possession of and the right to reproduce the Wiley Materials pursuant to Section 2 herein during the continuance of this Agreement. You agree that you own no right, title or interest in or to the Wiley Materials or any of the intellectual property rights therein. You shall have no rights hereunder other than the license as provided for above in Section 2. No right, license or interest to any trademark, trade name, service mark or other branding ("Marks") of WILEY or its licensors is granted hereunder, and you agree that you shall not assert any such right, license or interest with respect thereto

- NEITHER WILEY NOR ITS LICENSORS MAKES ANY WARRANTY OR REPRESENTATION OF ANY KIND TO YOU OR ANY THIRD PARTY, EXPRESS, IMPLIED OR STATUTORY, WITH RESPECT TO THE MATERIALS OR THE ACCURACY OF ANY INFORMATION CONTAINED IN THE MATERIALS, INCLUDING, WITHOUT LIMITATION, ANY IMPLIED WARRANTY OF MERCHANTABILITY, ACCURACY, SATISFACTORY QUALITY, FITNESS FOR A PARTICULAR PURPOSE, USABILITY, INTEGRATION OR NON-INFRINGEMENT AND ALL SUCH WARRANTIES ARE HEREBY EXCLUDED BY WILEY AND ITS LICENSORS AND WAIVED BY YOU.

- WILEY shall have the right to terminate this Agreement immediately upon breach of this Agreement by you.

- You shall indemnify, defend and hold harmless WILEY, its Licensors and their respective directors, officers, agents and employees, from and against any actual or threatened claims, demands, causes of action or proceedings arising from any breach of this Agreement by you.

- IN NO EVENT SHALL WILEY OR ITS LICENSORS BE LIABLE TO YOU OR ANY OTHER PARTY OR ANY OTHER PERSON OR ENTITY FOR ANY SPECIAL, CONSEQUENTIAL, INCIDENTAL, INDIRECT, EXEMPLARY OR PUNITIVE DAMAGES, HOWEVER CAUSED, ARISING OUT OF OR IN CONNECTION WITH THE DOWNLOADING, PROVISIONING, VIEWING OR USE OF THE MATERIALS REGARDLESS OF THE FORM OF ACTION,

WHETHER FOR BREACH OF CONTRACT, BREACH OF WARRANTY, TORT, NEGLIGENCE, INFRINGEMENT OR OTHERWISE (INCLUDING, WITHOUT LIMITATION, DAMAGES BASED ON LOSS OF PROFITS, DATA, FILES, USE, BUSINESS OPPORTUNITY OR CLAIMS OF THIRD PARTIES), AND WHETHER OR NOT THE PARTY HAS BEEN ADVISED OF THE POSSIBILITY OF SUCH DAMAGES. THIS LIMITATION SHALL APPLY NOTWITHSTANDING ANY FAILURE OF ESSENTIAL PURPOSE OF ANY LIMITED REMEDY PROVIDED HEREIN.

- Should any provision of this Agreement be held by a court of competent jurisdiction to be illegal, invalid, or unenforceable, that provision shall be deemed amended to achieve as nearly as possible the same economic effect as the original provision, and the legality, validity and enforceability of the remaining provisions of this Agreement shall not be affected or impaired thereby.

- The failure of either party to enforce any term or condition of this Agreement shall not constitute a waiver of either party's right to enforce each and every term and condition of this Agreement. No breach under this agreement shall be deemed waived or excused by either party unless such waiver or consent is in writing signed by the party granting such waiver or consent. The waiver by or consent of a party to a breach of any provision of this Agreement shall not operate or be construed as a waiver of or consent to any other or subsequent breach by such other party.

- This Agreement may not be assigned (including by operation of law or otherwise) by you without WILEY's prior written consent.

- Any fee required for this permission shall be non-refundable after thirty (30) days from receipt by the CCC.

- These terms and conditions together with CCC's Billing and Payment terms and conditions (which are incorporated herein) form the entire agreement between you and WILEY concerning this licensing transaction and (in the absence of fraud) supersedes all prior agreements and representations of the parties, oral or written. This Agreement may not be amended except in writing signed by both parties. This Agreement shall be binding upon and inure to the benefit of the parties' successors, legal representatives, and authorized assigns.

- In the event of any conflict between your obligations established by these terms and conditions and those established by CCC's Billing and Payment terms and conditions, these terms and conditions shall prevail.

- WILEY expressly reserves all rights not specifically granted in the combination of (i) the license details provided by you and accepted in the course of this licensing transaction, (ii) these terms and conditions and (iii) CCC's Billing and Payment terms and conditions.

- This Agreement will be void if the Type of Use, Format, Circulation, or Requestor Type was misrepresented during the licensing process.

- This Agreement shall be governed by and construed in accordance with the laws of the State of New York, USA, without regards to such state's conflict of law rules. Any legal action, suit or proceeding arising out of or relating to these Terms and Conditions or the breach thereof shall be instituted in a court of competent jurisdiction in New York County in the State of New York in the United States of America and each party hereby consents and submits to the personal jurisdiction of such court, waives any objection to venue in such court and consents to service of process by registered or certified mail, return receipt requested, at the last known address of such party.

WILEY OPEN ACCESS TERMS AND CONDITIONS

Wiley Publishes Open Access Articles in fully Open Access Journals and in Subscription journals offering Online Open. Although most of the fully Open Access journals publish open access articles under the terms of the Creative Commons Attribution (CC BY) License only, the subscription journals and a few of the Open Access Journals offer a choice of Creative Commons Licenses. The license type is clearly identified on the article.

The Creative Commons Attribution License

The Creative Commons Attribution License (CC-BY) allows users to copy, distribute and transmit an article, adapt the article and make commercial use of the article. The CC-BY license permits commercial and non-

Creative Commons Attribution Non-Commercial License

The Creative Commons Attribution Non-Commercial (CC-BY-NC)License permits use, distribution and reproduction in any medium, provided the original work is properly cited and is not used for commercial purposes.(see below)

Creative Commons Attribution-Non-Commercial-NoDerivs License

The Creative Commons Attribution Non-Commercial-NoDerivs License (CC-BY-NC-ND) permits use, distribution and reproduction in any medium, provided the original work is properly cited, is not used for commercial purposes and no modifications or adaptations are made. (see below)

Use by commercial "for-profit" organizations